Energy Management System in DC Future Home

Wei Zhang

Thesis submitted to the faculty of the
Virginia Polytechnic Institute and State University
in partial fulfillment of the requirements for the degree of

Master of Science
In
Electrical Engineering

Fred C. Lee, Chair
Dushan Boroyevich
Qiang Li

May 12th, 2015
Blacksburg, Virginia

Keywords: DC Nano-grid, Li-Ion Battery, Bidirectional Battery Charger, Net-zero Energy and Energy Management

Energy Management System in DC Future Home

Wei Zhang

(Abstract)

Making electricity grids smarter and facilitating them with integration of renewable energy sources (RES) and energy storage are fairly accepted as the necessary steps to achieve a sustainable and secure power industry. To enable Net-zero energy and optimize power management for future homes or buildings, DC electric distribution systems (DC Nano-grid) find feasibility and simplicity for integrating renewable energy sources and energy storage. However, integrating the sources and loads in a simple, robust and smart way is still challenging.

High voltage lithium-ion battery should be seriously considered concerning the overcharge/over-discharge risk. Dissipative cell equalization and its performance are studied. Non-dissipative equalization methods are reviewed using an energy flow chart. Typical charging schemes and the related over-charge risk are illustrated. A Lithium-ion battery charging profile based on $V_{Cell\_Max/Min}$ monitoring is proposed and validated with experimental results in an 8.4kW bidirectional battery charger for DC future home.

For the DC future home emulator testbed, a grid interface converter, i.e. energy control center (ECC) converter, is reviewed with functions identification. A PV system with different configurations is compared to further expand the common MPPT region, and a DC-DC converter is designed as the interface between PV panels and DC bus, facilitating maximum power point tracking (MPPT) as well as fulfill the system energy management requirement. An 8.4kW multi-

phase bidirectional battery charger with Si IGBT in DCM operation is designed to achieve high efficiency and to be the interface converter between lithium-ion battery and DC bus, enhancing the battery system management as well as increasing the system reliability.

To integrate all the sources and loads in a simple, reliable and smart way, this thesis proposes a distributed droop control method and smart energy management strategy to enhance the Net-zero electric energy cost. All of the control strategies are applied to the DC future home with interactions among the energy control center (ECC), renewable energy sources, energy storage and load within a day/24 hours. System level energy management control strategies for Net-zero electric energy cost are examined and illustrated. A 10kW future home emulator testbed is built and introduced for concepts validation.

Acknowledgement

I would like to express my sincere gratitude and appreciation for my advisor, Professor Fred C. Lee, for his continuous guidance, encouragement and support during my study and research in CPES. Through all the tremendous effort Dr. Lee spent on me, I improved myself greatly in many aspects, and of which the most important part is the research attitude – never stop challenging myself, never take anything for granted and never use alibi . All of the training and improvements will definitely benefit me in the future work.

I also would like to give specific appreciation to Dr. Dushan Boroyevich, Dr. Rolando Burgos, Dr. Paolo Mattavelli and Dr. Qiang Li. As the faculty advisors in the REN group, their wisdom, vision and guidance does help me a lot during my research. And it is an honor for me to have Dr. Dushan Boroyevich and Dr. Qiang Li as my committee members. I am truly thankful to them for all the technical discussions, opinions and suggestions.

A lot of work in this dissertation is team efforts. I would like to appreciate my previous and current colleagues for their contributions and assistances. It includes Mr. Igor Cvetkovic in REN system architecture; Mr. Fang Chen and Dr. Dong Dong in ECC converter; and Mr. Zhongsheng Cao, Mr. Sizhao Lu, Dr. Feng Wang, Mr. Li Jiang and Mr. Pin-yu Huang in PV System.

I would like to thank colleagues in the power management consortium (PMC) and renewable energy nano-grid consortium (REN) of CPES. It is my honor to work with these talented, creative, helpful and dedicated people: Dr. Wenli Zhang, Dr. Mingkai Mu, Dr. Pei-Hsin Liu, Dr. Dongbin Hou, Dr. Dianbo Fu, Dr. David Reusch, Mr. Shu Ji, Dr. Pengju Kong, Dr.

Daocheng Huang, Mr. Pengjie Lai, Mr. Zijian Wang, Mr. Qian Li, Dr. Yingyi Yan, Mr. Feng Yu, Mr. Haoran Wu, Mr. Chanwit Prasantanakorn, Dr. Weiyi Feng, Dr. Yipeng Su, Mr. Shuilin Tian, Mr. Li Jiang, Dr. Pei-Hsin Liu, Mr. Xiucheng Huang, Mr. Zhengyang Liu, Mr. Yuchen Yang. Mr. Chao Fei, Mr. Xuebin Chen, Mr. Syed Bari, Mr. Zhongsheng Cao, Mr. Bin Li, Mr. Tao Liu, Mr. Junjie Feng, Mr. Zhengrong Huang, Ms. Yincan Mao, Ms. Virginia Li. Mr. Mohamed Ahmed, Dr. Zhiyu Shen, Mr. Jun Wang, Mr. Alinaghi Marzoughi, Dr. Marko Jaksic, Dr. Bo Wen, Mr. Yang Jiao, Mr. Chi Li, Mr. Ruiyang Qin, Mr. Shishuo Zhao. Mr. Yadong Lyu, Mr. Chen Li and Mr. Eric Hsieh.

I also appreciate all other colleagues and students at CPES: Dr. Fang Luo, Dr. Di Zhang, Dr. Puqi Ning, Dr. Ruxi Wang, Dr. Dong Jiang, Dr. Zheng Chen, Dr. Sara Ahmed, Dr. Xuning Zhang, Dr. Zhuxian Xu, Dr. Jing Xue, Dr. Zheng Zhao, Mr. Bo Wen, Mr. Milisav Danilovic, Mr. Lingxiao Xue, Mr. Bo Zhou, Dr. Hemant Bishnoi, Ms. Christina DiMarino, Mr. Qiong Wang, Mr. Yin Wang, Ms. Han Cui, Dr. Woochan Kim, Mr. Tao Tao, Mr. Di Xu, Mr. Kumar Gandharva, Mr. Zhemin Zhang, Mr. Hanguang Zheng, Dr. Yiying Yao, Mr. Ming Lu, Mr. Ting Ge, Ms. Haryani Nidhi, Mr. Najmi Vahid, Ms. Rashidi Mehrabadi Niloofar, Ms. Bingyao Sun. It is precious memory to live and work with you in CPES.

Many visiting scholars have brought their expertise and helpful discussion during my research. They are Dr. Kuang-Yao Cheng, Dr. Xiaoyong Ren, Dr. Yue Chang, Dr. Feng Zheng, Dr. Xinke Wu, Dr. Weijun Lei, Mr. Zeng Li, Dr. Jin Li, Dr. Monti ê Vitorino, Dr. Feng Wang, Dr. Xiwei Zhou, Dr. Hao Zhang, Dr. Weijing Du, Mr. Peiqing Hu, Dr. Guiping Du, Dr. Alian Chen, Mr. Pin-Yu Huang. Thank you for the help and friendship.

I would also like to thank the wonderful members of the CPES staffs who were always willing to help me: Ms. Teresa Shaw, Mr. David Gilham, Ms. Linda Gallagher, Ms. Teresa Rose, Ms. Marianne Hawthorne, Ms. Linda Long, Mr. Douglas Sterk.

My deepest appreciations go towards my parents Xiaogang Zhang and Chunying Xie, my lovely wife Yunmiao (Kathy) Wang, who have always been there with their love, support, understanding and encouragement for all of my endeavors.

This work was supported by the Renewable Energy Nano-grid Consortium (REN) at CPES (Delta Electronics, ABB, SIEMENS, GE, Huawei, Keysight, Boeing, ONR and College of Engineering of Virginia Tech).

Table of Contents

List of Figures

List of Tables

Chapter 1 Introduction

1.1 Background and Motivation

1.1.1 Electric Energy and Distributed Power Generation

Making electricity grids smarter while facilitating them with the integration of renewable energy sources (RES) is fairly accepted as part of the necessary steps to achieve a sustainable and secure power industry [1][2]. Based on the 2014 annual energy outlook report by The U.S. Energy Information Agency (EIA) [3], renewable energy is projected to grow substantially from 2013 to 2040 in all cases, like wind, solar, geothermal, etc., however the largest growth is expected in the wind and solar generation area. In 2013, as a result of increases in wind and solar generation area, total non-hydropower renewable generation was almost equal to hydroelectric generation for the first time, see Figure 1.1. In 2040, non-hydropower renewable energy sources will account for more than two-thirds of the total renewable generation, and the total renewable share of all electricity generation will increase from 13% in 2013 to 18% in 2040.

Taking the usable electric energy into consideration, in 2011, the total energy consumed to generate electricity was 40.04 quadrillion Btu (British thermal unit) [4], shown in Figure 1.2, however, the gross usable electric energy is only 14.82 quadrillion Btu, around 37% of the total energy needed. The total conversion loss is massive, and must be kept in mind of the importance of improvement in the energy conversion efficiency, and thus resources conserved and pollution avoided are far greater than the energy we have been used.

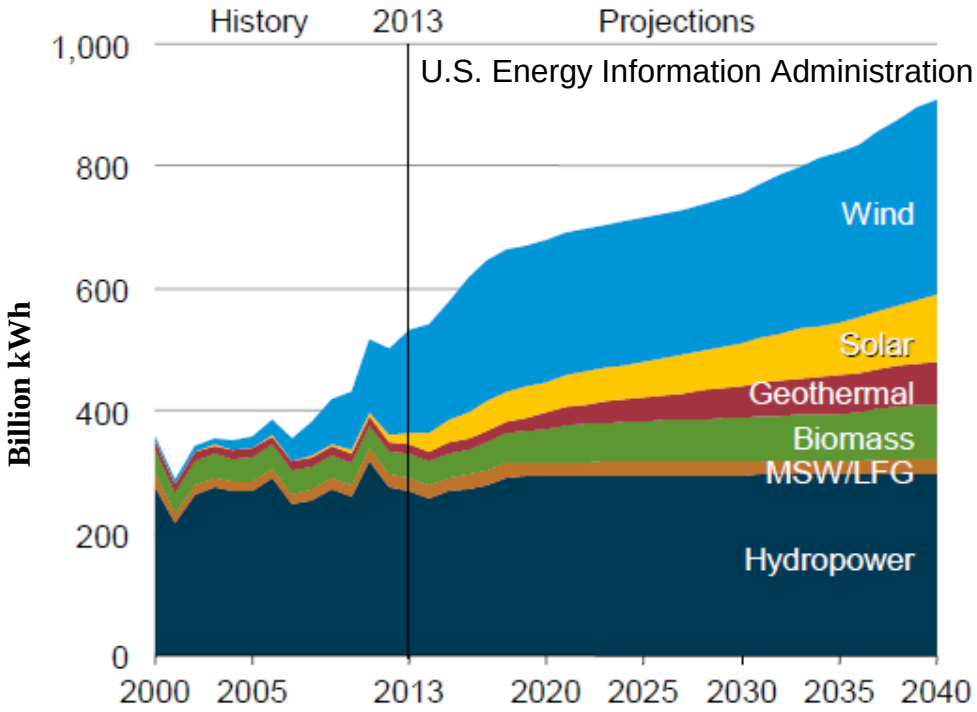

Figure 1.1 Renewable electricity generation by fuel type (billion kWh) [3] - Dept. of Energy. Public domain

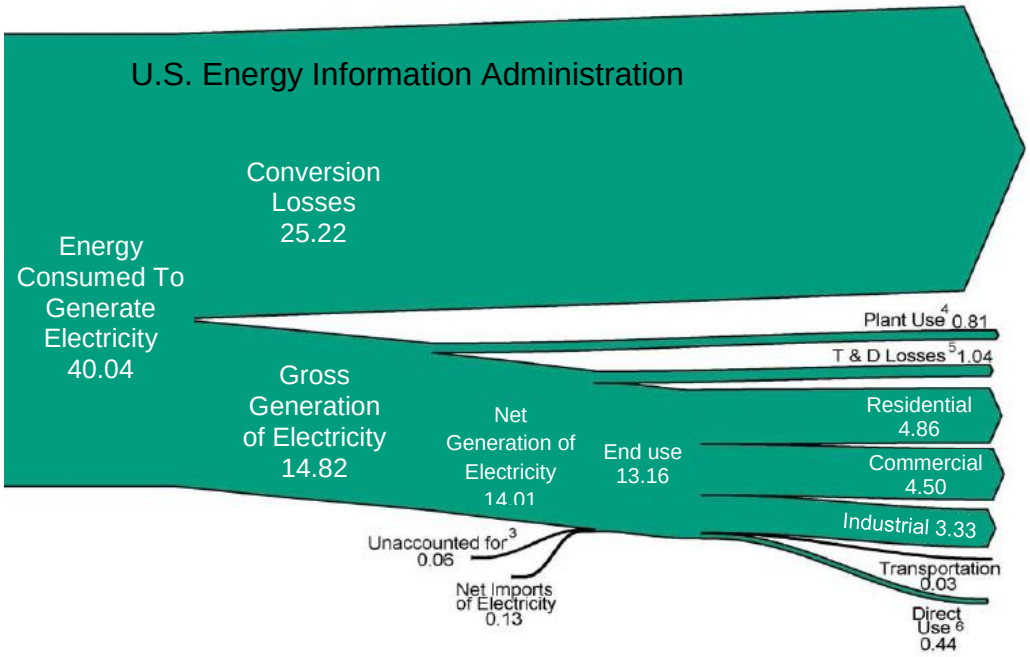

Figure 1.2 U.S. electricity energy flow in 2011 (Quadrillion Btu) [4] - Dept. of Energy. Public domain

Considering the end use distribution, as shown in Figure 1.2, there are three major parts: 1) Residential; 2) Commercial; 3) Industrial. Residential applications include single- and multi-family residences. Commercial buildings include offices, stores, restaurants, warehouses, others for commercial purposes, and government buildings. Figure 1.3 shows the proportion of the three major categories for electricity end use consumption. The buildings account for over 70% of the total electric energy consumption, among which the residential buildings takes the largest portion, 37% of the total. Importantly, the energy used by the building sector continues to increase, primarily because new buildings are constructed faster than old ones are retired. In the study done by U.S. EIA [3], electricity consumption in the residential and commercial sectors increases by 0.5%/year and 0.8%/year from 2013 through 2040, respectively. What is more, considering the ever-increasing electricity price through the years, shown in Figure 1.4, the investment in the electric system and the cost for the end users will be a significant issue, thus, it also serves for the motivation of this study. To greatly reduce the energy consumption and address the concerns over environment protection and energy security, renewable energy, such as solar, wind, fuel cell, etc. [5][6], has been studied by counties intensively and extensively.

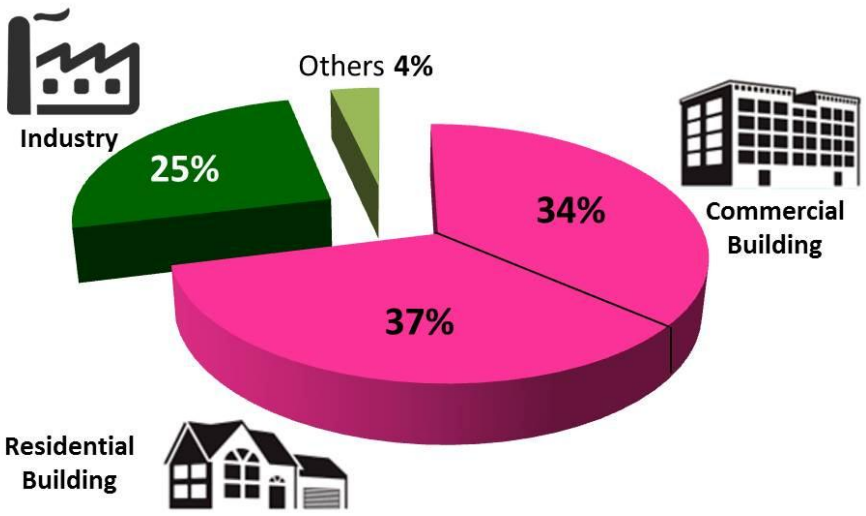

Figure 1.3 Distribution of End use electricity energy consumption

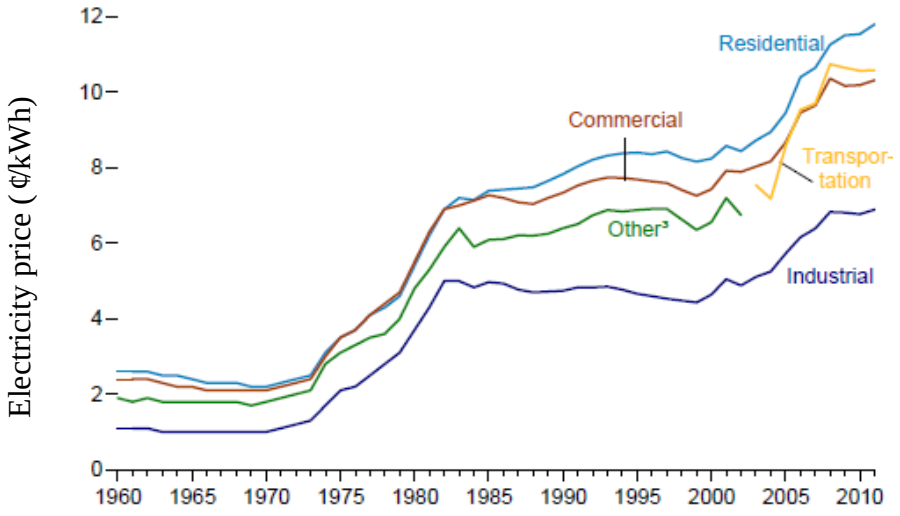

Figure 1.4 Average retail nominal prices of Electricity [4] - Dept. of Energy. Public domain

1.1.2 Net-zero Energy Buildings

A net-zero energy building is a residential or commercial building with greatly reduced energy needs through efficiency gains such that the balance of the energy needs can be supplied with renewable technologies [7].

The concept of net-zero energy buildings is the idea that buildings can meet all their energy requirements from low-cost, locally available, nonpolluting, renewable sources. Strictly speaking, a net-zero building generates enough renewable energy on site to equal or exceed its annual energy use. To meet this energy balance annually, connection with a grid in the buildings can facilitate excess electricity exported to the utility grid, and supply the building's load with utility when renewable energy is not available. Concerning intermittent solar and wind power output, however, in high market penetration scenarios, the grid may not always need the excess energy. Therefore, on-site energy storage would become necessary.

The National Renewable Energy Laboratory (NREL) defines net-zero energy buildings in four ways depending on the installation of different applicable renewable energy sources, project

goals and the values of the design team and building owner. These four definitions are: Net-zero site energy, Net-zero source energy, Net-zero energy costs and Net-zero energy emissions [7].

- Net-zero Site Energy: A site net-zero building produces at least as much energy as it uses in a year, when accounted for at the site.
- Net-zero Source Energy: A source net-zero building produces at least as much energy as it uses in a year, when accounted for at the source. Source energy refers to the primary energy used to generate and deliver the energy to the site. To calculate a building's total source energy, imported and exported energy is multiplied by the appropriate site-to-source conversion multipliers.
- Net-zero Energy Costs: In a Net-zero cost building, the amount of money the utility pays the building owner for the energy the building exports to the grid is at least equal to the amount the owner pays the utility for the energy services and energy used over the year.
- Net-zero Energy Emissions: A net-zero emissions building produces at least as much emissions-free renewable energy as it uses from emissions-producing energy sources.

This study focuses on the third definition on the subject of electric energy, i.e. Net-zero electric energy cost. A Net-zero electric energy cost building, that is interconnected with the grid with integration of different renewable energy sources and energy storage for the purpose of energy management optimization and off-grid (islanded operation) robustness, receives as much financial credit for the exported energy as it is charged on the utility bills. Figure 1.5 shows a picture describing a conceptual sustainable future home with installation of 1) renewables: roof-top solar panels as photovoltaic (PV) system and wind turbine; 2) energy storage devices, plug-in hybrid electric vehicles (PHEV) and battery energy storage devices; 3) utility grid connection

through energy control center (ECC); 4) loads: energy saving power electronics based home appliances.

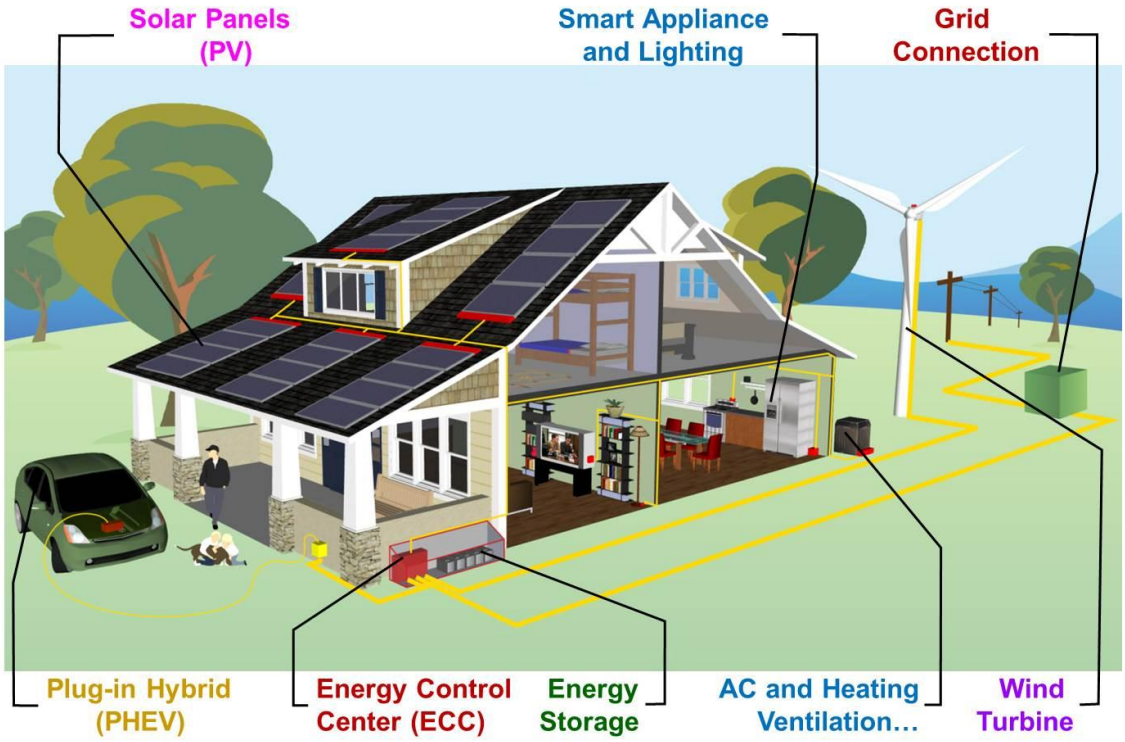

Figure 1.5 A conceptual sustainable future home

1.1.3 "AC vs. DC"

To achieve high reliability, efficiency and controllability for critical or advanced applications, such as hospitals, data centers, more electrified ships and aircrafts [1][2][8][9][10][11][12][13], etc., power electronics converters are widely used due to the rapid development of power convert topologies, advanced power semiconductors, advanced control, system packaging and cost reduction. This migration, thanks to fast growing power technology, recalls the historical debate between Thomas Edison and Nicola Tesla about the "AC vs. DC", which has already been addressed by high-voltage DC transmission (HVDC) [14][15] and demonstrated in many countries with advantages, such as increasing transmission efficiency.

Figure 1.6 shows an example of a residential building using conventional AC integration. Each source and load is interfacing with the utility through a power electronics converter for better power quality, advanced energy management, efficiency increase, system optimization, and dynamics decoupling. The important electric protection device of this system is the centralized circuit breaker or fuse panel for all the loads, and the current rating is normally over 5 times higher than the installed capacity, as well as the electrical wiring. Furthermore, all the sources have the additional stage of DC-AC conversion, and all the electrical appliances have front-end AC-DC conversion for power quality, since most of the sources have a DC bus or a DC link, like solar/wind, batteries, and most of the loads require a DC bus/link with a DC-DC or a DC/AC conversion for more electrified/controllable loads, like LED lighting, computers, as well as motors or compressors.

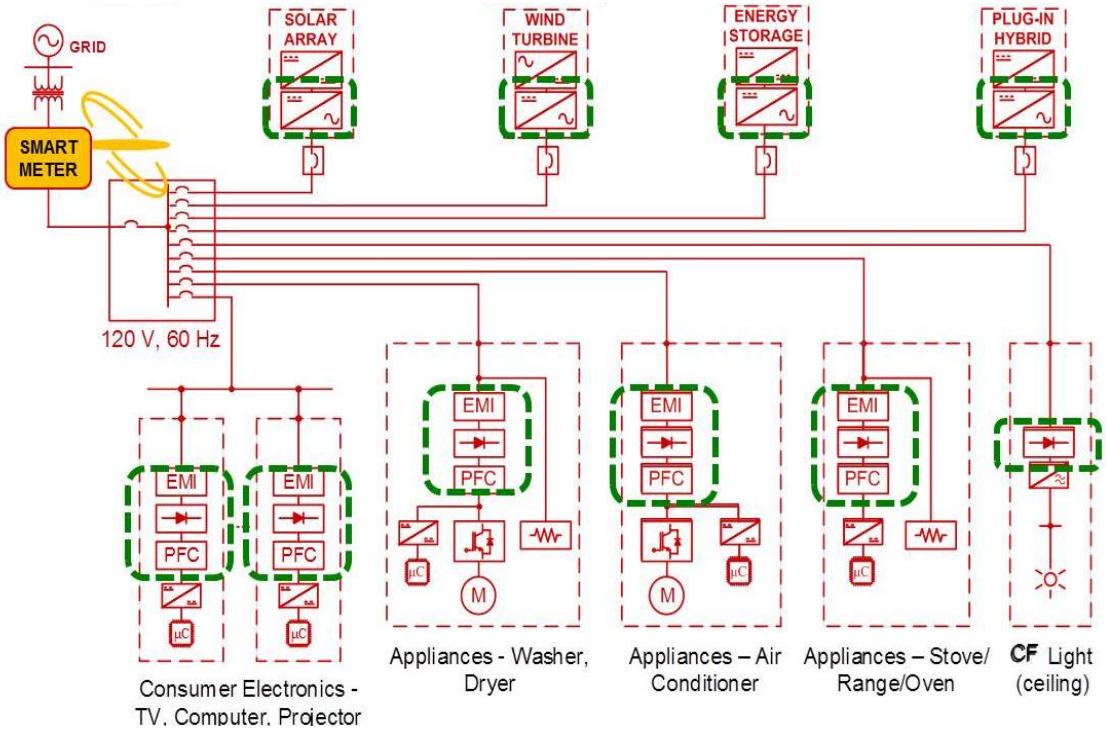

Figure 1.6 AC integration for residential buildings

Figure 1.7 shows an example of DC integration for residential buildings [16][17][18], which has an energy control center (ECC) as the interface between the utility and $380V_{DC}$ bus, and all the sources and loads directly couple to the DC bus through one simple stage DC-DC converter or DC-AC inverter. A secondary 24V or 48V low voltage bus can be introduced to supply consumer appliances, like a TV, computer, cell phone charger, which saves the bulky and expensive adaptors. To summarize, the benefits of the DC over AC system integration include:

- High efficiency – less energy conversion
- Low cost – single stage DC-DC converter or DC-AC inverter
- More reliable – protection is done by power converter with programmable current limiting, i.e. 110% rated load current, far less than rating of circuit breaker or fuses.
- Easier control and better energy management – better understanding of the DC system

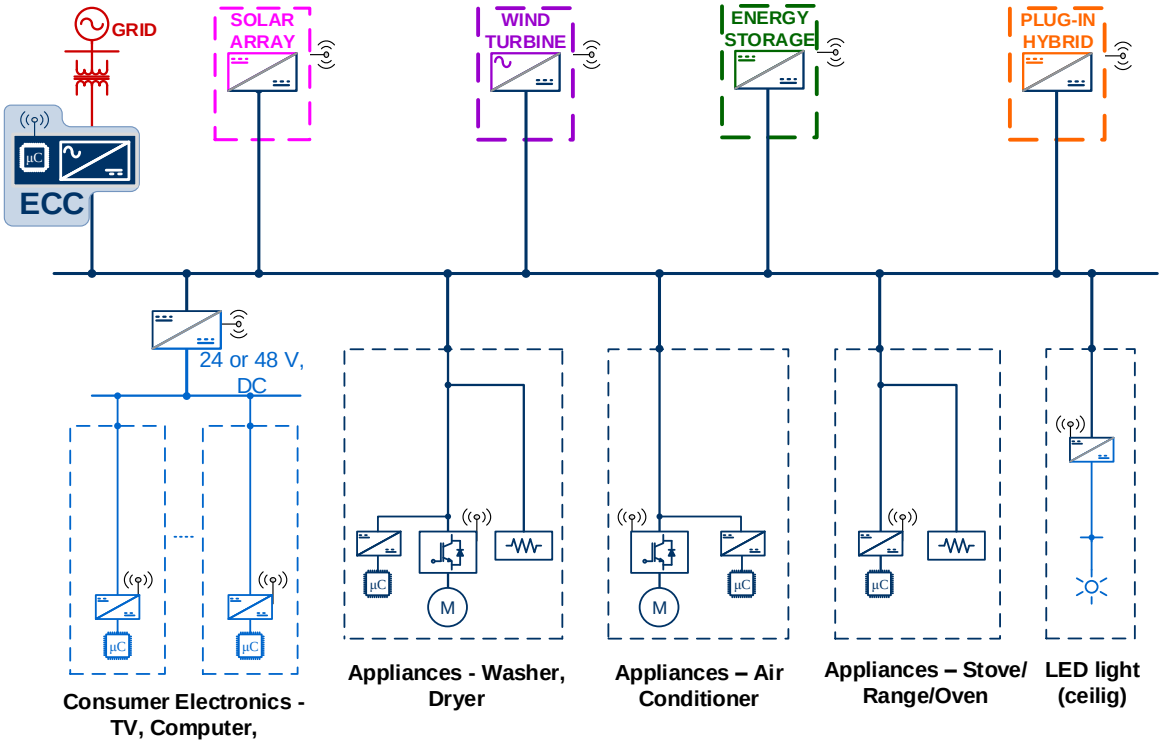

Figure 1.7 DC integration for residential buildings

1.2 High Voltage Lithium-ion Battery Management for DC Future Home

1.2.1 Distributed Energy Storage and Lithium-ion Battery

With the increasing use of distributed energy resources and the emergence of the Smart Grid, distributed energy storage is becoming more and more important and popular [19], and is driven by many factors including: a) managing peak load demand due to peaking generation and transmission constrains; b) expected increased penetration of distributed energy generation with intermittent output; c) increasing emphasis on richer electric energy and services pricing, such as time-of-use energy prices and the increasing exposure of market-based prices for ancillary services; d) Net-zero electric energy as mentioned in section 1.1, e) accelerating battery storage cost reduction and performance improvement.

Energy storage devices, which have been installed in the power system [19][20], majorly includes pumped-storage hydroelectric (PSH), compressed air energy storage (CAES) and different kinds of electrochemical battery technologies including NaS, Zinc-bromine (Zn/Br), Lead-acid, Ni-MH, Lithium-ion batteries and capacitors (EDLC), shown in Figure 1.8. Among all the characteristics of the battery, the rated available energy, corresponding to discharging time, and the rated power, corresponding to the load power requirement, are the two most important factors. As shown in Figure 1.8, PSH and CAES are for high power and energy applications. Distributed storage devices (<20kWh for house or small community) focus on (Plug-in) hybrid electric vehicles ((P) HEV) approved batteries, such as ultra-caps, NiMH and Lithium based batteries. Table 1.1 shows the comparison among the three batteries considering energy and power density, self-discharge rate for standby and storage performance, life-cycle and temperature range [21][22][23][24]. The data shows that Li-ion battery performs best with the highest balanced specific energy and power density, very low self-discharge rate, accepted

life-cycle and wide temperature range, making it not only achieves commercialization in Battery EV or (P)HEV, but also gain interests in utility applications as distributed energy storage, which requires above 15 years life, a small footprint for serving residences or a business park up to 50kW & 4hours of storage capability [19].

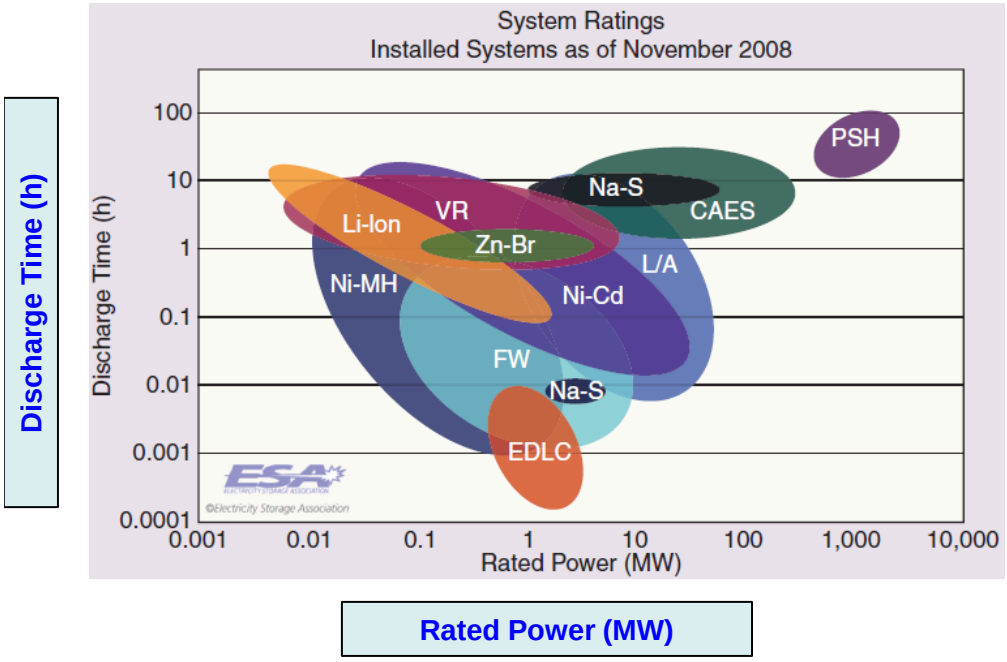

Figure 1.8 Energy storage devices for electric system

Table 1.1 Comparisons of Li-ion, Ni-MH and Super-capacitor

	Li – ion	Ni-MH	Super-cap
Energy density (Wh/kg)	100~250	30~80	3~5
Power density(W/kg)	300~1500	250~1000	1000~2000
Self-discharge (/Month)	2~3%	15~30%	< 100%
Life-cycle(20% Degrade)	> 1000	500~1000	750k
Temp. range(°C)	-20~60	5~25	-30~52

1.2.2 High Voltage Lithium-ion Battery System Management Considerations

As mentioned in 1.2.1, the Li-ion battery belongs to an electrochemical battery which physically has three major parts, positive material, negative material and a separator. Figure 1.9 shows the detailed configuration and reaction mechanism [26]. The positive and negative materials usually have a layered structure to facilitate intercalation of the lithium ions. The net effect of the charge and discharge reaction is the movement of lithium ions back and forth between the electrodes, matched by a corresponding flow of electrons in the external circuit.

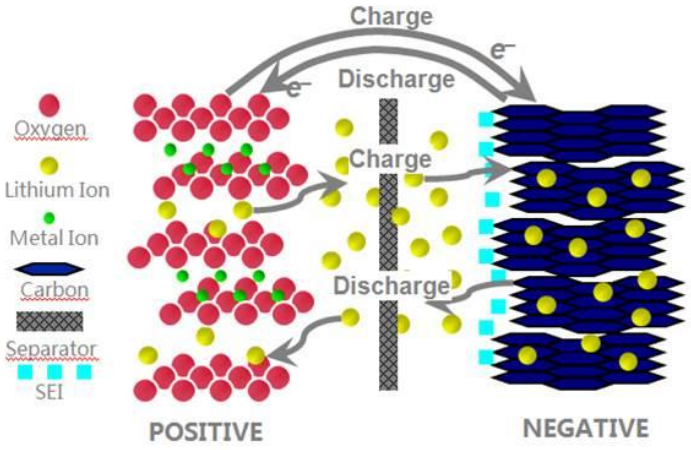

Figure 1.9 Representation of lithium-ion reaction mechanism

Figure 1.10 shows the typical lithium-ion battery cell voltage vs. capacity. Generally speaking, a high state of charge (SoC) will have a higher cell voltage and a low SoC has lower voltage, which builds a slope among the total capacity range. Depending on different lithium-ion battery positive electrode materials constitution [21][22][23][24][25][26][27][28][29][30], such as $Li_4Ti_5O_{12}$ – *LTO*, $LiFePO_4$ – *LFP*, $LiNi_xCo_yAl_zO_2$ – *NCA*, $LiNi_xMn_yCo_zO_2$ – *NMC and* $LiMn_2O_4$ – *LMO*, the maximum cell voltage is 3.0~4.4V and the minimum cell voltage is from 2.0~2.5V. For both conditions, the lithium-ion battery cannot be over-charged and over discharged. Over-charging will lead to over-heating, thermal runaway and even fire, while over-

discharging will cause impedance increase, thermal instability and permanent capacity loss. To charge a low voltage, <3V for LTO or NCA cell, pre-charge with low charging current (≈0.1·C) is required to prevent over-heat of the cell, since cell impedance is very high at low SoC.

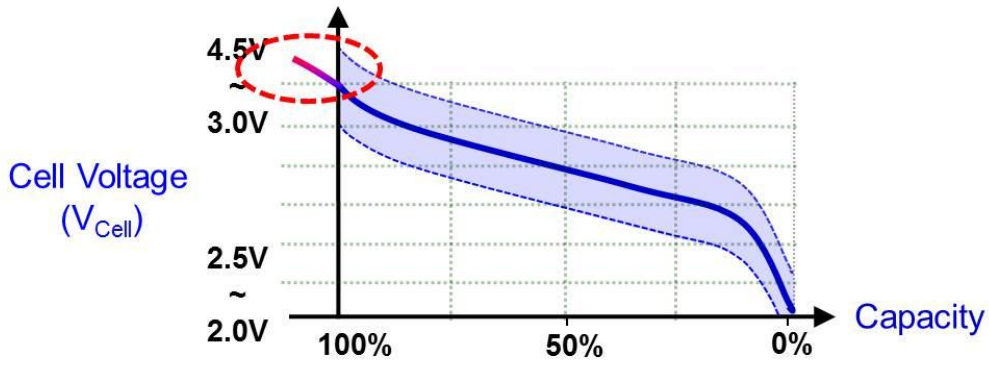

Figure 1.10 Lithium-ion battery cell voltage vs. capacity

For most portable customer appliances, like cellphones, lab top computers and power tools, less than 5 cells in series connected are needed to provide the required voltage. However, a lithium-ion battery used in electric vehicles, distributed energy storage, etc., contains up to one hundred cells in series [17], building a high voltage DC bus, up to 400V, for a high power energy load, such as EV motor drive and data center. On the other hand, many factors [26] including 1) manufacturing deviation; 2) temperature unbalance; 3) impedance difference; 4) self-discharge; 5) charge/discharge efficiency, lead the series-connected cells to deviate from balance, and cause an unbalanced state of charge (SoC). Importantly, the unbalance will continue to get worse and worse if there is no electric circuit assistance.

Therefore, the available battery SoC cannot be fully utilized because charging should be stopped when the maximum cell voltage among the battery pack, V_{Cell_Max}, is fully charged with 100% SoC, and discharging should be stopped when the minimum cell voltage, V_{Cell_Min}, is approaching the allowed minimum voltage limit, shown in Figure 1.11.

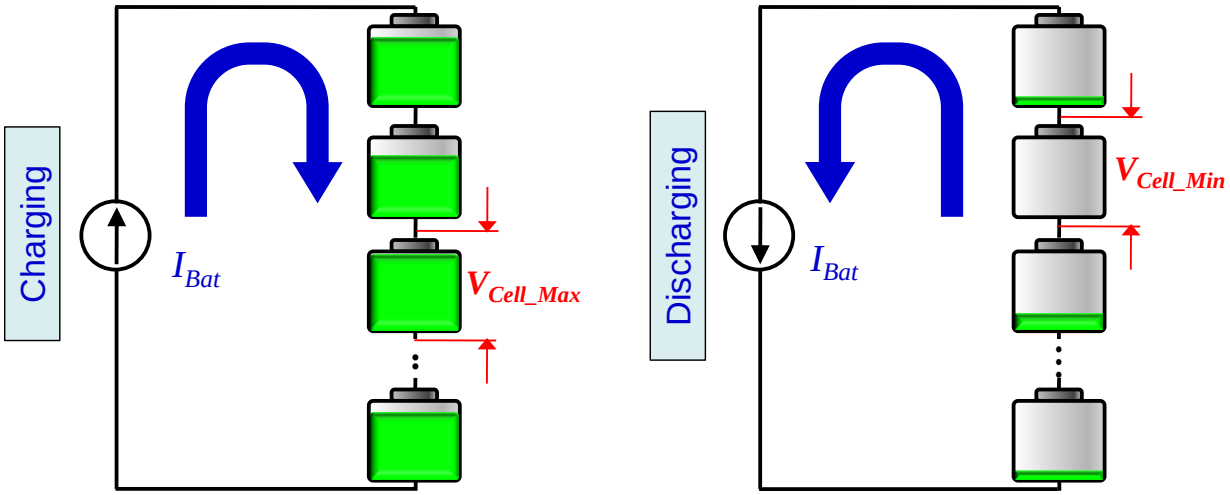

Figure 1.11 Charge and discharge with unbalanced lithium-ion cells

A typical battery charger/discharger assumes that the series connected cells are well balanced. Therefore, in order to protect the battery from over charge/discharge, a cell equalization electric circuit is always provided. There are two major equalization categories, shown in Figure 1.12: 1) Dissipative [31][32]; 2) Non-dissipative [33].

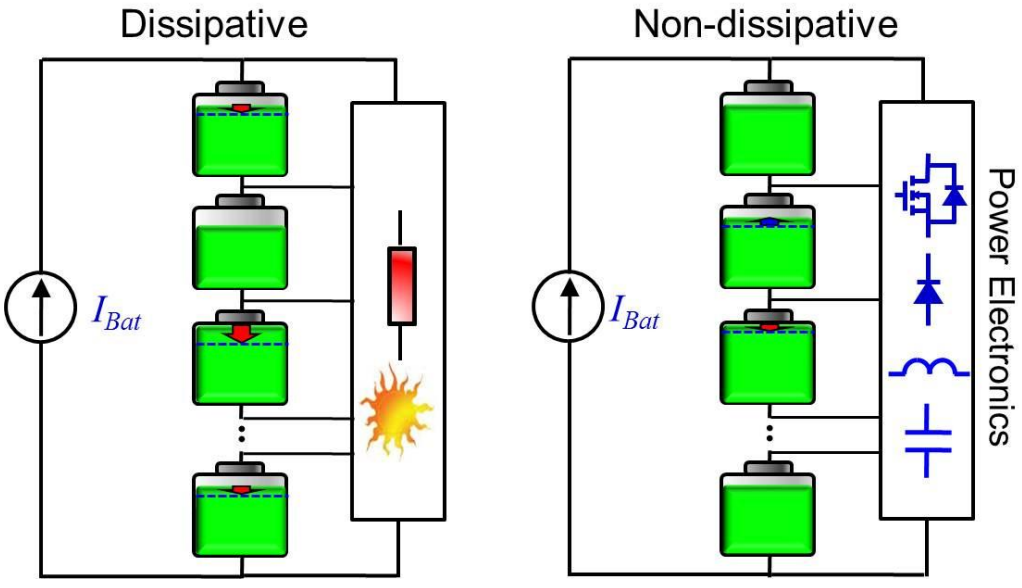

Figure 1.12 Dissipative and non-dissipative equalization methods

Dissipative methods dissipate the higher state of charge (SoC) of cells until they reach the level of the lowest SoC cell. The major benefits of the dissipative ways include control simplicity, easy implementation, low cost and higher reliability. However, it is inefficient to bleed the stored energy. Non-dissipative methods, which are also called active cell equalization methods, apply a power electronics circuit with the utilization of active devices, inductors and capacitor to achieve equalization by transferring the energy among all the series connected lithium-ion cells. The difference between the two is that dissipative methods bleed the energy in a higher SoC cell into heat, and non-dissipative methods recycle it, therefore, causing the equalization speed to be faster and more efficient.

1.3 Energy Management System Control for DC Future Home

1.3.1 Centralized Control Based on Supervisor Computer

To integrate multiple renewable energy sources and energy storage to the DC Nano-grid, there are two major types of control methods. The first one is centralized control, shown in Figure 1.13, and applied in [39]. The benefit of centralized control is that energy management strategies can be implemented easily in the central controller since this controller is aware of each source and load component in the entire system. Centralized control requires real-time feedback from each terminal to produce operational orders and commands. The major drawback of centralized control is that a high-speed communication path is required for real-time controlling of the fast switched converters. Considering the fast and non-coincidental load demand in the residential application, even the high speed communication cannot satisfy the transient requirement. What is more, the system loses the centralized control or smartness, or even shuts down when the communication system fails. To summarize, centralized control

method relies on supervisor computer for smart energy management and control, but suffers system reliability and robustness.

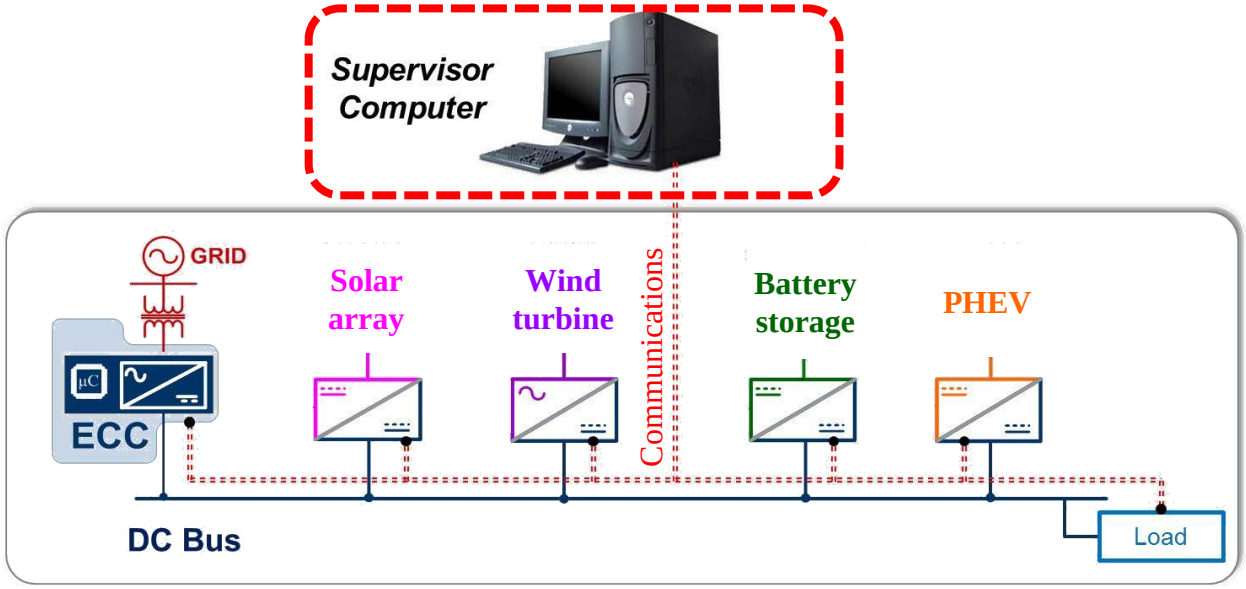

Figure 1.13 Centralized control based on supervisor computer

1.3.2 Decentralized Control with Different Droop Impedance

Another type of control is decentralized control, or autonomous control, which majorly applies the droop control method, show in Figure 1.14, to integrate different sources for current sharing depending on the corresponding droop impedance. This control doesn't need communication, which inherently increases the robustness of the system. Moreover, bus voltage under droop control also carries information with load level, for example, a higher load will lead to a lower bus voltage, which can be easily applied to shed loads at some critical conditions. However, fixed droop control cannot facilitate smart energy flow or dispatching, like energy storage, which not only can provide energy backup, but also can buffer renewable energy and share load when the utility electricity price is high on the peak load-demanding hours. The decentralized control method is discussed and applied in [40][41][42][43][44][45]. [40][41][42] initiate and propose a low voltage DC distribution system ($650V_{DC}$) with droop control for easy

integration of DC sources, such as SMES coil, energy storage and renewables. [43] improves the droop argument and discussed the power flow by adjusting the droop impedance, which serves an important role in DC system. [44][45] discuss a DC system with the utilization of the droop control method and consider the droop bus voltage as key information, i.e. DC bus signaling. However, all of these discussions don't clearly specify the objective and control for energy storage system, and lithium-ion battery system management/protection is not accurately addressed and illustrated for system level integration. What is more, none of the discussions mention load profile or source profile for the residential application, which plays an important role on energy management. Finally, system-level hardware implementation in these literatures isn't paid much attention, either scaled down too much, or test examples are not meaningful and hard to understand.

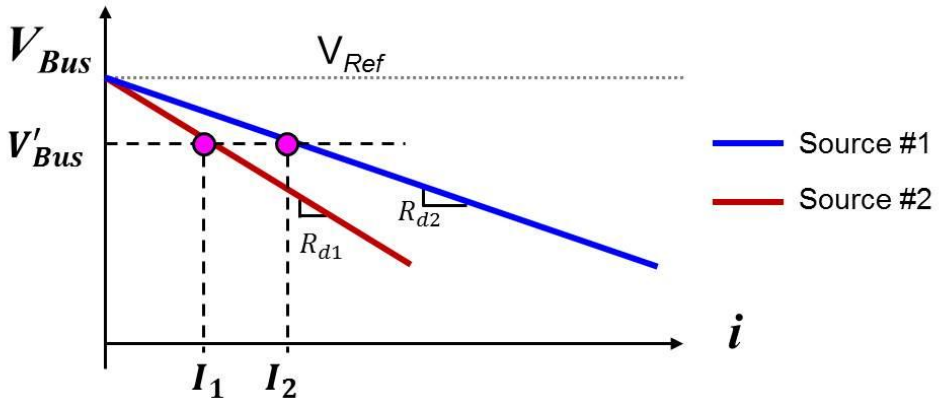

Figure 1.14 Decentralized control with different droop impedance

[46] introduces a testbed for low-voltage DC Nano-grid of residential building based on the concept proposed by [2], shown in Figure 1.7. In [46], comparisons of "smart" AC Nano-grid and DC-based Nano-grid in the future home are given and each component converter and the corresponding static operations are illustrated with preliminary experimental results. However, the static operation and control laws for energy storage are not clear. Moreover, system level

control objectives and operation consideration are not discussed, and system level experiments are not included. Additionally, the discussion is not based on system level with coordination of grid interface converter and renewable energy sources.

1.4 Thesis Outline

Taking into account the challenges raised during the literature survey on the energy management system for the DC future home, several issues have been addressed in this thesis:

Chapter 1:

Research background, motivation and literature review.

To enable Net-zero electric energy cost and optimize power management for future homes or buildings, the DC electric distribution systems (DC Nano-grid) find feasibility and simplicity for integrating multi-type renewable energy sources. However, integrating all the sources and loads in a simple, reliable and smart way is still challenging. High voltage lithium-ion battery management should be seriously taken into consideration before connecting it to the system, which includes over-charge/over-discharge protection and cell equalization. Si-IGBT operating in continuous current mode (CCM) suffers high reverse recovery loss and has low efficiency. Finally, to integrate all the source components in the DC bus in a robust and smart way, and to achieve net-zero electric energy cost with minimum investment are still challenging and need to be carefully addressed.

Chapter 2:

Battery system management: cell equalization, over-charge/over-discharge protection.

High voltage Li-ion battery system in DC Nano-grid and its management considerations are introduced. The lithium-ion battery cell spice model with internal equivalent charging/discharging resistance is provided based on experiment results. The Dissipative cell

equalization and its performance are studied for high voltage lithium-ion battery energy storage in future home applications. Non-dissipative equalization methods are reviewed using energy flow charts. Battery management controller and system-level configurations of the lithium-ion battery are introduced. Typical charging schemes considering total battery bank voltage to control the constant voltage charging and the related over-charge risk are illustrated. A lithium-ion battery charging profile based on $V_{Cell\_Max/Min}$ monitoring is proposed and the design consideration with CAN bus communication is addressed and validated with experimental results in an 8.4kW bidirectional battery charger for DC future home. Finally, the concept of a smart battery module based on an integrated charger and equalizer is introduced.

Chapter 3:

Design consideration for DC Nano-grid: ECC, PV system, Battery converter,

The ECC converter is reviewed with identification of the system functions, including AC-DC bidirectional interface, bus regulation and system level communication among sources and loads. And simulation models of the ECC converter, including switching, average and DC behavior models, are built for system level simulation purposes.

PV configurations with consideration of mismatches are reviewed with the utilization of smart DC-DC converter to increase the maximum power. Different configurations are compared with severe mismatch cases studied to further expand the common MPPT region, thus increasing the maximum power. A centralized converter will interface the PV panels with the DC bus by achieving MPPT for PV system, and facilitating the requirement of DC system energy management. And simulation models of the PV converter, including switching, average and DC behavior models, are built for system level simulation purposes.

An 8.4kW multi-phase bidirectional battery charger with Si IGBT in DCM operation is designed to achieve high efficiency and to be the interface converter between lithium-ion battery and DC bus. Power device candidates considering smaller switching loss and conduction loss are compared and discrete Infineon Si-IGBT with TO-220 package is selected for the phase-leg design. Switching performance, including turn-on and turn-off loss of the target device, is characterized with double pulse tester for accurate loss model and loss breakdown. CCM and DCM operation is compared considering the switching loss and inductor volume. Finally, 8.4kW bidirectional converter prototype is implemented and tested for the purpose of system integration and energy management study. And simulation models of the Battery converter, including switching, average and DC behavior models, are built for system level simulation purposes.

Chapter 4:

Energy management system control strategy and experiment validation for Net-zero electric energy cost.

This chapter discusses the proposed distributed droop control method and smart energy management with a comparison of centralized and decentralized control, and then investigates the proposed control strategies for every source converter, including ECC, PV and energy storage, to enhance the Net-zero electric energy cost. Finally, all of the control functions, in system and component level, are applied to the DC future home with interactions among the energy control center (ECC), renewable energy sources and load variation during a 24 hours day. Importantly, a similar concept can be extended to do analysis for a week, season and year. What is more, system level energy management control strategies for Net-zero electric energy cost are examined and illustrated. A 10kW future home emulator testbed is built and introduced. Finally, all the concepts are experimentally verified with considerations of 24 hours residential load

demand profile, local renewable energy source profile and schedules of electricity rates from a local utility company.

Chapter 5:

Conclusions and future work.

Chapter 2 High Voltage Lithium-ion Battery System Management and Protection

The overall performances of the Lithium-ion battery make it not only find applications in portable appliances, but also gain popularities in electric vehicles. However, fault conditions, such as overcharge/over-discharge, will hurt the lithium-ion by increasing cell impedance, shortening cycle life, or even catch fire. Therefore, serious considerations over battery protection and battery management system should be taken for reliable and robust system operations.

2.1 Introduction of High Voltage Li-Ion Battery System in DC Nano-grid

2.1.1 Lithium-ion Battery Cell and Battery Pack Introduction

The Li-Ion battery used in DC Nano-grid is from SAFT batteries [47], and the cell is manufactured based on the electrochemistry of $LiNi_xCo_yAl_zO_2$ (NCA) for the positive electrode material. The maximum allowed cell voltage is 4.0V, and the minimum allowed cell voltage is 3.0V. Average cell capacity is 45Ah (C/3 charge to 4.0V/Cell – Model # VL45E). The energy and power density are 149Wh/L (4.0V) and 1400W/L (30s peak with 50% SoC) respectively. Table 2.1 shows the detailed specifications of VL45E. Importantly, the charging current limit is depending on battery temperature. Over 20℃, the maximum charging current is 25A, while this limit decreases as temperature decrease. The datasheet of VL45E cell shows the maximum

charging current limit is 12A, 8A and 2A for 0℃, -10℃ and -20℃, respectively. And the corresponding characteristics at 20℃ of the cell voltage vs. Capacity with different current are shown in Figure 2.1.

Table 2.1 Specification of 45Ah Li-Ion Battery Cell (VL45E)

Maximum Cell Voltage (V_{Cell_Max})	**4.0V**
Minimum Cell Voltage (V_{Cell_Min})	**3.0V**
Maximum Charge Current (>20°C)	**25A**
Maximum Discharge Current	**100A**
Cycle Life (80% DoD, 20°C)	**3000**

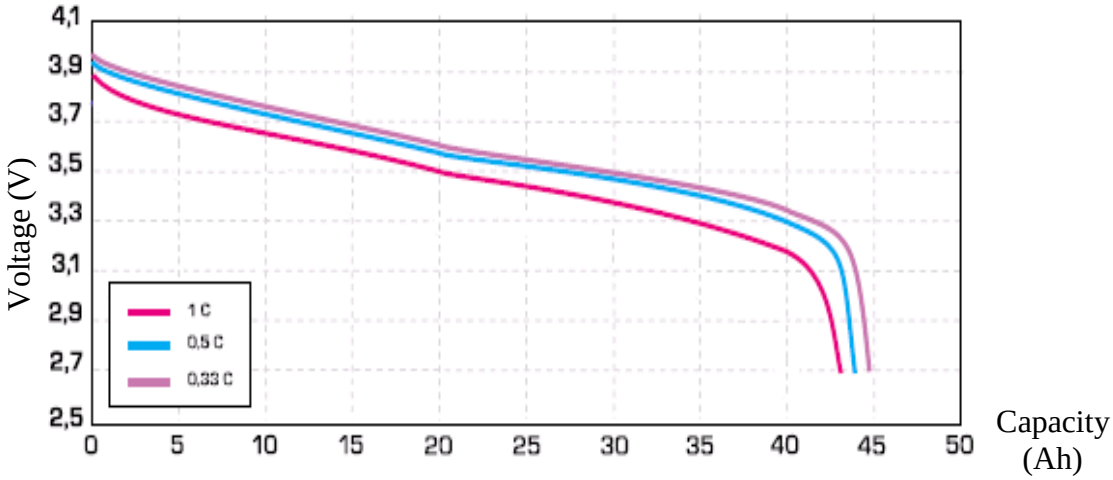

Figure 2.1 Cell voltage vs. capacity (Discharge), 20℃

To obtain a high voltage/power with the utilization of 4.0V single cell, there would be a certain number of individual cells in series connected. Figure 2.2 shows the detailed battery pack configuration, which is divided into 6 modules in series connected and each module has 14 series-connected cells. Therefore, 84 cells, in total, are series connected with the maximum allowed battery pack voltage to be 336V and the minimum battery voltage to be 252V.

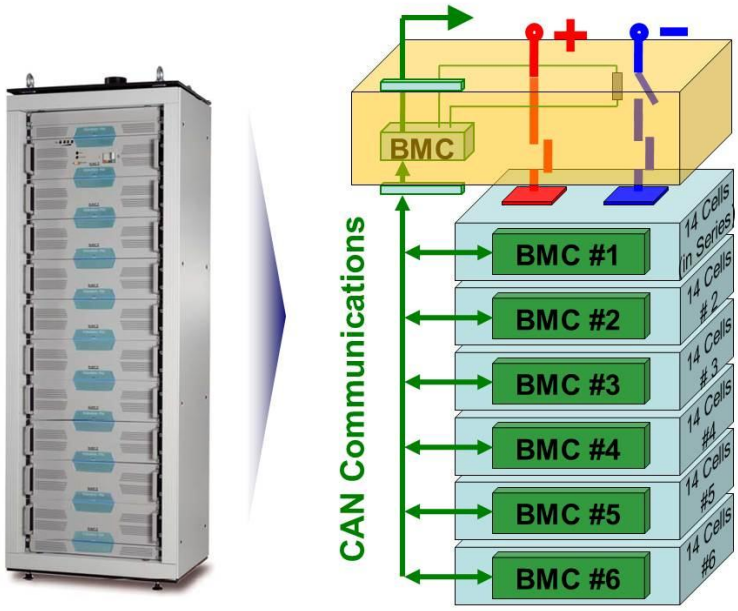

Figure 2.2 Lithium-ion battery pack configurations

Battery picture is from http://www.saftbatteries.cn/sites/default/files/ess_market-brochure_en.pdf, Used under fair use, 2015

As shown in Figure 2.2, there is a local battery management controller for each battery module, which is used to monitor the miscellaneous battery module information, including each cell voltage, temperature, total battery pack voltage and current, fuel gauging – SoC, fault, cell equalization and so on. All the information is communicated with CAN bus for interfacing with an upper system-level controller. Moreover, there will be an over current circuit breaker with manual command and redundant safety contactor used for over voltage, over current and other fault protection, shown in Figure 2.2.

2.1.2 Lithium-ion Battery Aging Factors

The lithium-ion battery has limitations over discharge, charge, state of charge (SoC), temperature, life cycle etc.; therefore, factors that affect the aging of the lithium ion battery cell should be investigated before the integration of Lithium-ion battery pack. [48][49] thoroughly discuss the potential factors which affect the aging effects of the lithium-ion cell by recording cell internal resistance, cell power level, cell cycle number under different test conditions, such

as SoC, temperature, and charge/discharge rate. Among all the degrading factors, cell internal impedance increases is the most critical one, which reflects the permanent loss of Li material and degradation of the available power. Figure 2.3 shows the Lithium-ion cell (NCA Cell) internal impedance variation as a function of depth of discharge (DoD), after storage periods. Figure 2.3 (a) shows that the cell internal resistance is around 2.2mΩ at the initial state, and increases to above 6mΩ after 404 days when storage is at 100% SoC and 60 ℃. However, Figure 2.3 (b) is stored in 50% SoC at the same temperature, and cell internal resistance in still less than 3.5mΩ after 416 days and less than 5mΩ even after 712 days. Comparing Figure 2.3 (a) and (b), it can be concluded: 1) the cell internal resistance increases faster when the battery is stored under higher SoC, and the potential factor affecting the resistance is the higher pressure under higher SoC conditions. The specific reason can be found in [48]; 2) deep depth of discharge (DoD) increases cell impedance. As shown in Figure 2.3 (b), after 712 days, cell impedance is 4.75mΩ at 80% DoD, around 50% higher than that in 20% DoD.

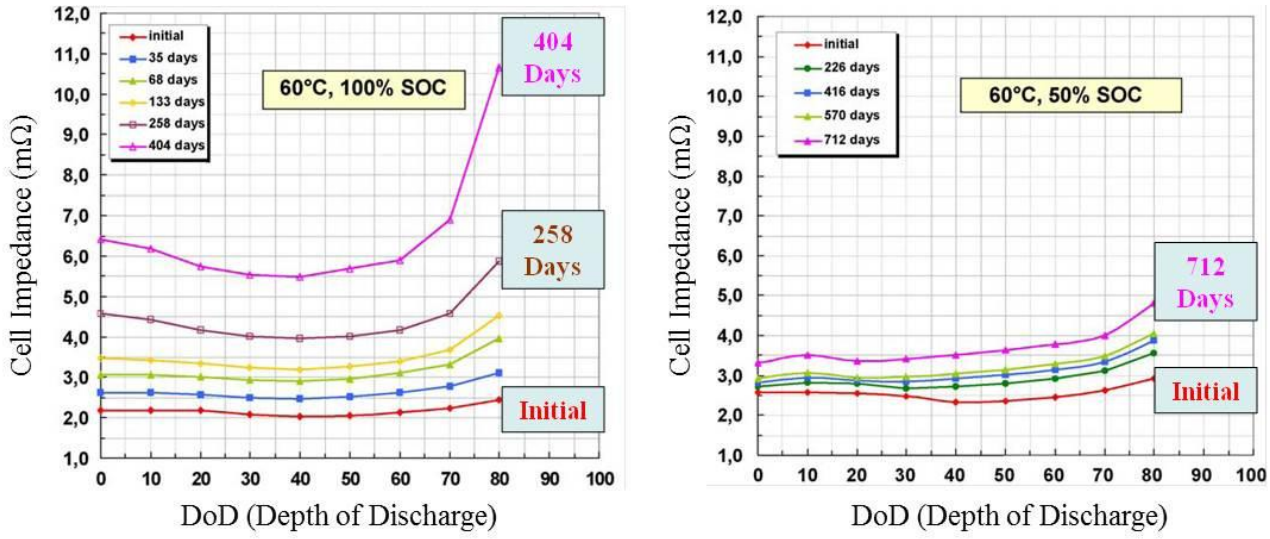

(a) Cell impedance with 100% SoC Storage (b) Cell impedance with 50% SoC Storage

Figure 2.3 Comparison of cell resistance with DoD [48], and Used under Fair use, 2015.

[48] M. Brousselya, Ph. Biensanb, etc., "Main aging mechanisms in Li ion batteries"; Journal of Power Sources Volume 146, Issues 1-2, 26 August 2005, Pages 90-96.

Figure 2.4 shows temperature and its effects on the output power of the Lithium-ion cell. Comparing the blue lines and red lines, it can be found that the higher temperature, 60 ℃, will have a dramatic decrease on cell power output, while the power condition at 20 ℃ does not change much. What is more, the solid and dash blue line comparison also reflects the conclusion drawn from Figure 2.3. Additionally, Figure 2.4 also shows that a solid blue line, storage under higher temperature and higher SoC, is the worst case for storing the Lithium-ion battery cell. Therefore, to extend the lithium-ion battery cycle life, higher temperature (>60 ℃) and higher SoC (100%) storage should be avoided to decrease the degradation speed of the cell internal impedance.

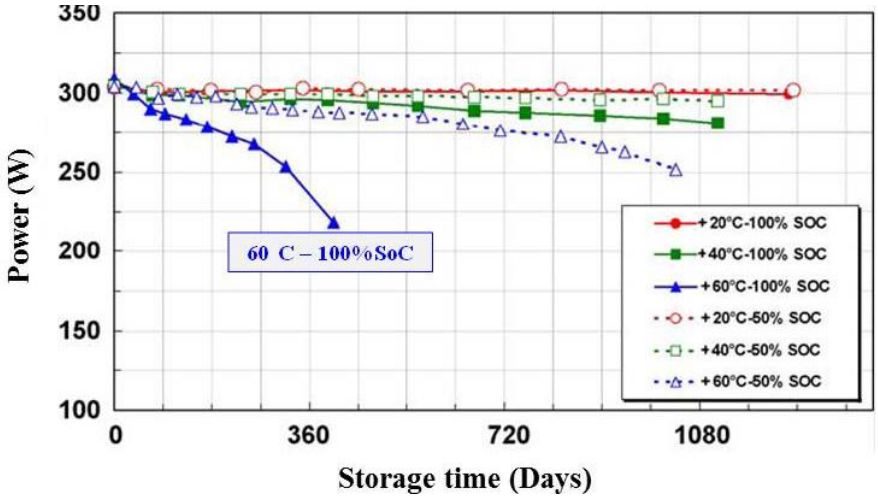

Figure 2.4 Power degradation vs. temperature and SoC [48], and Used under Fair use, 2015.

[48] M. Brousselya, Ph. Biensanb, etc., "Main aging mechanisms in Li ion batteries"; Journal of Power Sources Volume 146, Issues 1-2, 26 August 2005, Pages 90-96.

Figure 2.5 shows the charge and discharge current rate versus cell capacity counting the cycle number of the $LiCoO_2$-based cell [49]. At 1C charging (1C means that the discharge current will fully discharge the battery cell in 1 hour), shown in Figure 2.5 (a), the battery capacity is still over 80% of the rated capacity after 500 cycles (1C rate discharge battery from 4.2V to 2.75V, and charge with various rate), however, the capacity is only less than 30% with a 1.4C charging rate. Therefore, it can be seen that the higher the charging current rate, the faster

the cell capacity degrades. As for the discharging rate and capacity degradation, in Figure 2.5 (b), the trend is still the same, higher discharge rate will lead to faster degradation. However, it is not as sensitive as the charging rate. At 1.5C of discharging rate, the capacity is still over 70% of rated capacity after 500 cycles (1C rate charge battery from 2.75V to 4.2V, and discharge with various rate), which means the lithium-ion battery cell is more resilient for a high discharge current rate.

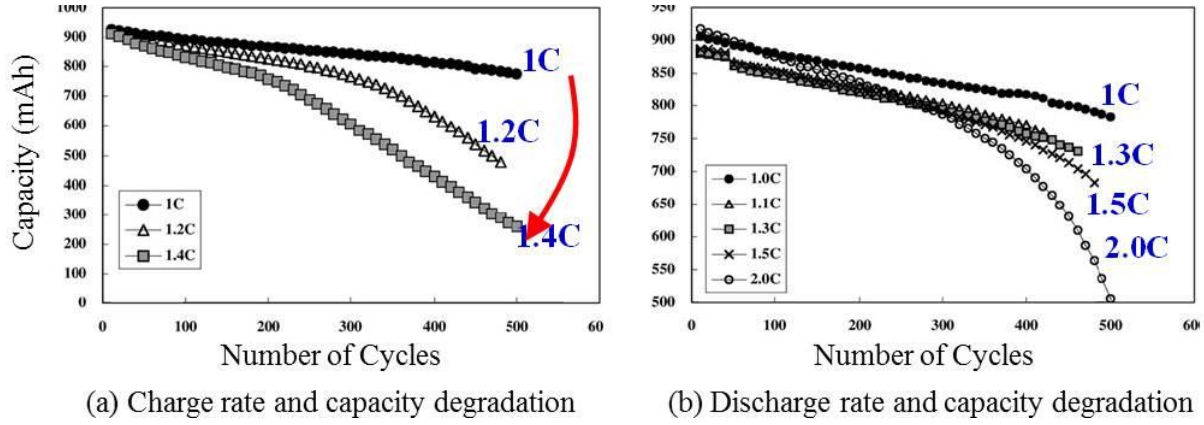

Figure 2.5 Charge/discharge rate and its effects on capacity degradation [49], and Used under Fair use, 2015.

[49] Soo S. Choi, Hong S. Lim, "Factors that affect cycle-life and possible degradation mechanisms of a Li-ion Cell Based on LiCoO2", Journal of Power Source, Volume 111, Issue 1, 18 Sep. 2002, Pages 130-136.

2.1.3 Lithium-ion Battery Cell Spice Model

For system level simulation of energy management, it is necessary to predict the SoC and the voltage of the lithium-ion battery pack (VL45E Cell used in our system) besides the allowed current specifications introduced in 2.1.1 and 2.1.2, because SoC decides the available energy stored in the battery pack, and the instantaneous voltage under different load decides the available maximum charge/discharge power.

[50] proposes an electric battery model, shown in Figure 2.6, for lithium-ion batteries. This model proves 0.4% runtime error and 30mV maximum error voltage, and the parameters

used in this model are easy to be extracted by a group of experimental results. Therefore, this model is used as the reference SPICE model for VL45E cell.

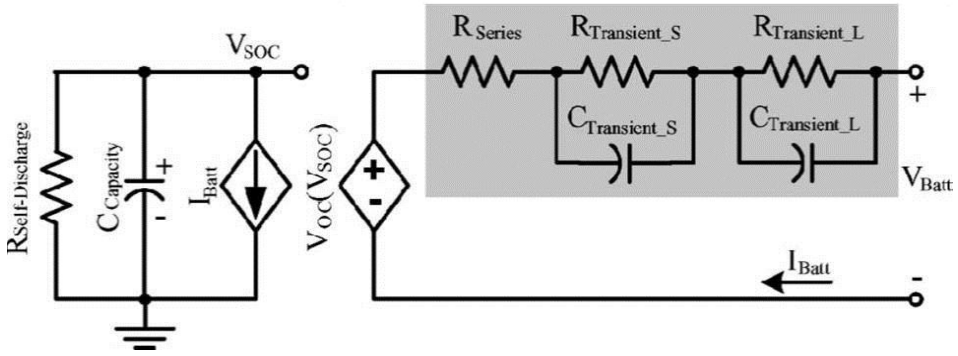

Figure 2.6 Lithium-ion battery cell spice model [50], and Used under Fair use, 2015.

[50] M. Chen; Rincon-Mora, G.A., "Accurate electrical battery model capable of predicting runtime and I-V performance," Energy Conversion, IEEE Transactions on, vol.21, pp.504,511, Jun. 2006.

In Figure 2.6, Capacitor $C_{Capacity}$ represents the available battery energy capacity with voltage, V_{SOC}, ranging from 0V~1V, where 0V means the battery is fully discharged and 1V means the battery is fully charged. And value of V_{SOC} can be used to represent SoC, where 0V for 0% of SoC and 1V represents 100% SoC. $R_{Self\text{-}Discharge}$ represents the self-discharge rate of the lithium-ion battery cell which is a quite large value and has a certain influence within months/years operation. Since the lithium-ion battery have very low self-discharge rate, $R_{Self\text{-}Discharge}$ can be ignored for operations within a few days or less. Controlled current source, $I_{Bat,}$ is decided by the load representing charging and discharging current. Finally, the controlled voltage source, $V_{OC}(V_{SOC})$, is normally provided by the battery manufacture representing the relationship between open circuit voltage V_{OC} and SoC. R_{Series}, $R_{Transient\_S}$ and $R_{Transient\_L}$ are the internal resistance of the lithium-ion battery and causes voltage drop under different load current and load step responses. Moreover, the SPICE model presented in [50] also considers all the dynamic characteristics for transient analysis, such as $C_{Transient\_S}$ and $C_{Transient\_L}$ in Figure 2.6.

Considering static operation for energy management in a 24 hours day in this study, $R_{Self\text{-}Discharge}$, $C_{Transient\_S}$ and $C_{Transient\_L}$ can be ignored. And all the series connected resistance in

Figure 2.6 could be combined to be one total resistance, R_{INT}, shown in Figure 2.7. Therefore, there are only two parameters required to complete the simplified lithium-ion SPICE model: 1) relationship between open circuit voltage V_{OC} and SoC; 2) internal resistance value for charging and discharging operation.

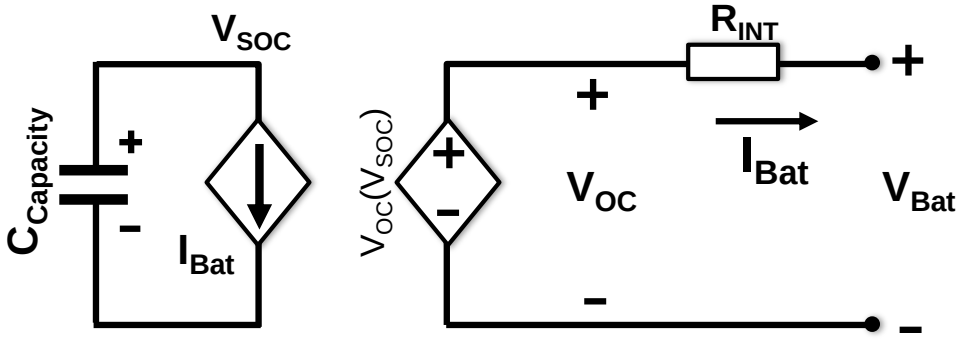

Figure 2.7 Simplified lithium-ion SPICE model for static operation

Figure 2.8 shows the relationship between open circuit voltage V_{OC} and SoC. The red dots are the original manufacture provided data, and the blue line is 6 orders of polynomial regression curve fitting graph from MathCAD, and the exact expression is found in (2.1)

$$\boldsymbol{V_{OC}(SoC) = A_0 + A_1 \cdot SoC + A_2 \cdot SoC^2 + A_3 \cdot SoC^3 + A_4 \cdot SoC^4 + A_5 \cdot SoC^5 + A_6 \cdot SoC^6} \qquad (2.1)$$

Where A_0=3.301, A_1=0.301, A_2=6.845, A_3= -31.929, A_4=61.21, A_5= -52.595, A_6=16.868;

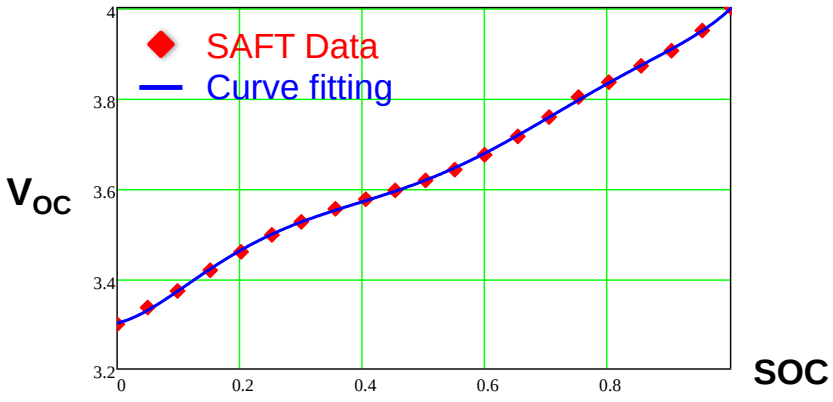

Figure 2.8 Curve fitting for the relationship between V_{OC} vs. SoC

It can be seen that the curve fitting data matching the original manufacture provided data very well, shown in Figure 2.8. Moreover, it is important to mention that the open circuit voltage doesn't represent the battery terminal voltage. The real battery terminal voltage should also consider the battery internal resistance.

In order to get the internal resistance of the VL45E cell, groups of charging current are applied to charge and discharge the battery. Figure 2.9 shows the measured cell voltage with charging currents of -15A and -25A. Negative sign corresponds to Figure 2.7 and designates the charging current direction. ΔV, shown in Figure 2.9 (a), highlights the voltage droop caused by internal resistance. With reference to open circuit voltage V_{OC}, also shown in solid blue line in Figure 2.9 (a), the internal resistance for charging is calculated and shown in Figure 2.9 (b), with the red and green lines designating the resistance for -25A and -15A respectively. A linear approximation of the charging resistance is found in (2.2) to represent the relationship between charging resistance, R_{INT_Chg}, and SoC.

$$\boldsymbol{R_{INT\_Chg}(SoC) = -0.003034024 \cdot SoC + 0.00635680482} \tag{2.2}$$

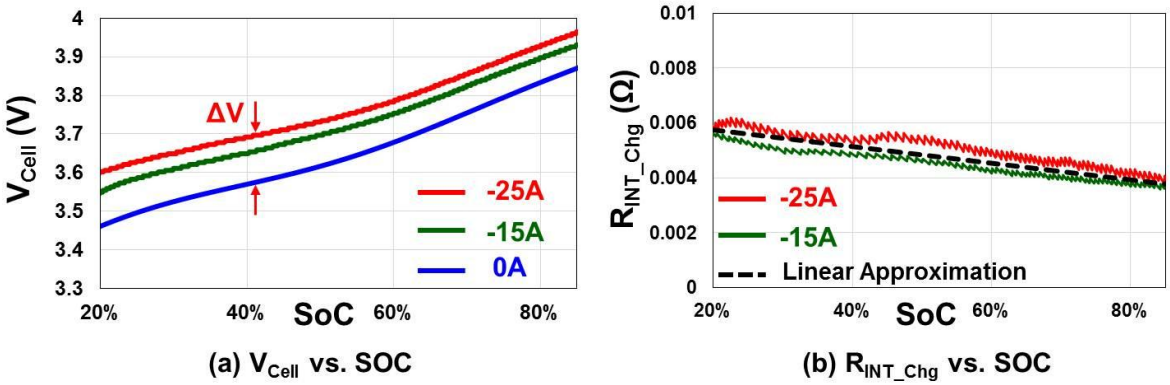

Figure 2.9 Battery cell internal charge resistance – R_{INT_Chg} vs. SoC

Similar to the charging resistance characterization, two groups of discharging currents are applied to battery to measure the discharge internal resistance. Figure 2.10 (a) shows the

measured battery cell voltages at 25A and 15A discharging current. Due to the internal resistance, the battery cell terminal voltage is lower than the cell open circuit voltage V_{OC}. Figure 2.10 (b) shows the extracted discharge internal resistance for 25A and 15A in red and blue line respectively. And the solid black line in Figure 2.10 (b) is 6 orders of polynomial regression curve fitting graph from MathCAD, and the exact expression is found in (2.3).

$$\boldsymbol{R_{INT\_Dchg}(SoC) = B_0 + B_1 \cdot SoC + B_2 \cdot SoC^2 + B_3 \cdot SoC^3 + B_4 \cdot SoC^4 + B_5 \cdot SoC^5 + B_6 \cdot SoC^6} \quad (2.3)$$

Where B_0=3.23m, B_1= -0.7723m, B_2=27.5789m, B_3= -169.817m, B_4=391.39, B_5= -380.56m, B_6=132.52m. And Figure 2.10 (b) shows that the curve fitting resistance matches the experimental data very well.

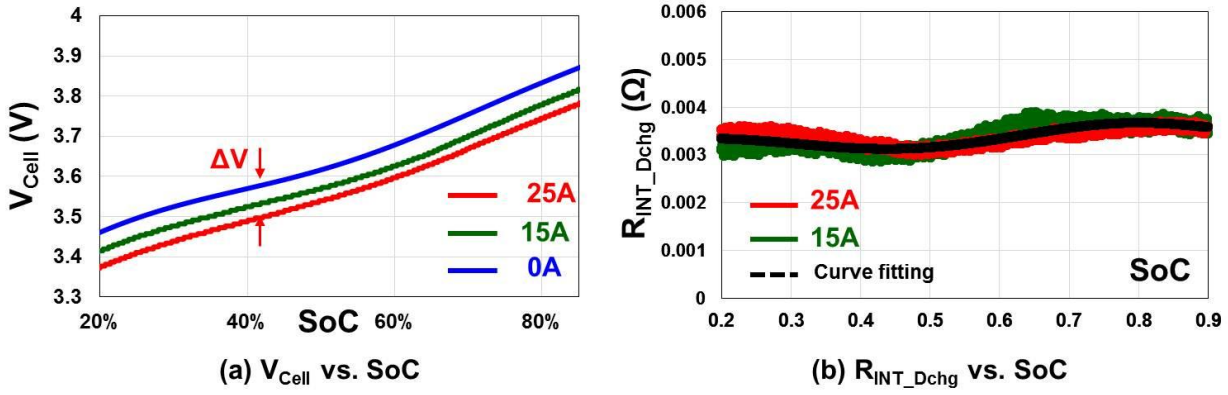

Figure 2.10 Battery cell internal discharge resistance – R_{INT_Dchg} vs. SoC

To integrate the charge/discharge resistance in one SPICE model, two ideal diodes are used in series with the R_{INT_Chg} and R_{INT_Dchg} respectively, shown in Figure 2.11, with the corresponding current directions. Simulating the complete SPICE model with charge/discharge currents of ±15A and ±25A, Figure 2.12 shows that the battery cell terminal voltages match the experiment very well.

For a battery bank with 84 identical cells in series connected, the complete SPICE model in Figure 2.11 can be easily modified by modifying the $C_{Capacity}$ and R_{INT} with $C'_{Capacity}$ =

$C_{Capacity} \cdot M/N$, $R'_{INT} = R_{INT} \cdot N/M$, where N is the number of series connected battery cells, and M is number of the parallel connected battery cells.

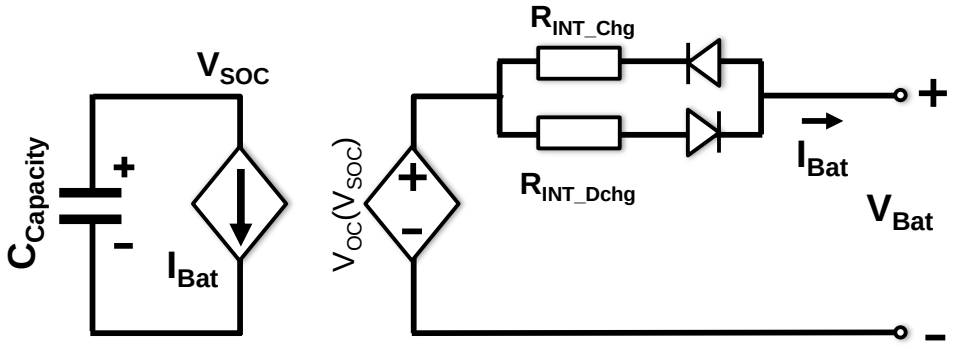

Figure 2.11 Simplified Li-ion model with separate charge/discharge internal resistance

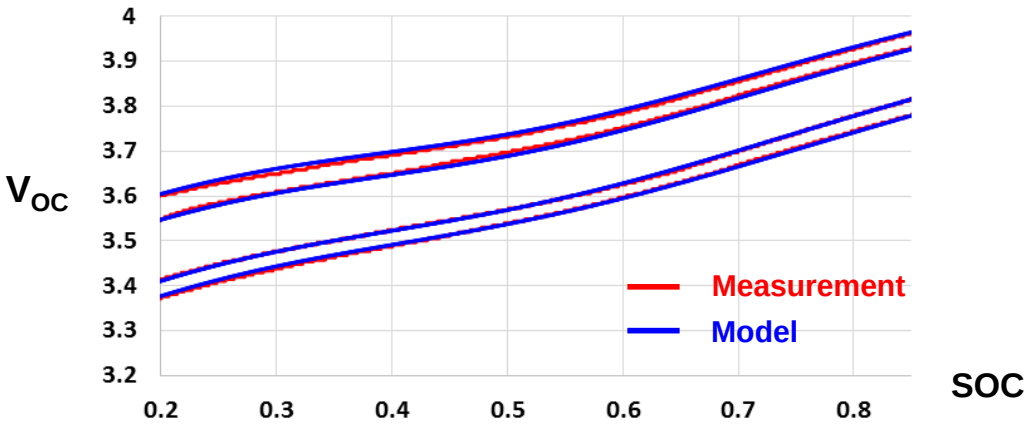

Figure 2.12 Extracted VL45E SPICE model and measurement results

2.2 Dissipative Cell Equalization and its Performance

Even though the dissipative cell equalizer suffers efficiency by bleeding the extra energy to be equal to the lowest cell SoC, it is still widely used in nearly all the commercial products because of control simplicity, easy implementation, low cost and high reliability, all of which are quite important in high reliability applications, such as PHEV and EV. Many commercial controller supports this method, such as *AD7280* [51], *BQ77PL900* [52]. For a high efficiency and reliability battery management system, it is essential to understand how the dissipative cell

equalizer works and to identify the issue of commercial design before addressing the non-dissipative cell equalization methods.

Figure 2.13 shows resistive cell equalization for a high voltage Li-Ion battery pack used for REN Nano-grid. CAN bus communication is applied for accessing battery management system information, including cell voltage, temperature, SoC, fault and so on, within which the most critical information is V_{Cell_Max} and V_{Cell_Min}, since they decide whether the battery back can accept or deliver energy. ΔV_{Cell}, show in (2.4), is defined to characterize how unbalance all the cells voltage are, where V_{Cell_Max} and V_{Cell_Min} are the maximum and minimum cell voltage among the whole lithium-ion battery pack.

$$\Delta \boldsymbol{V_{Cell}} = \boldsymbol{V_{Cell\_Max}} - \boldsymbol{V_{Cell\_Min}} \tag{2.4}$$

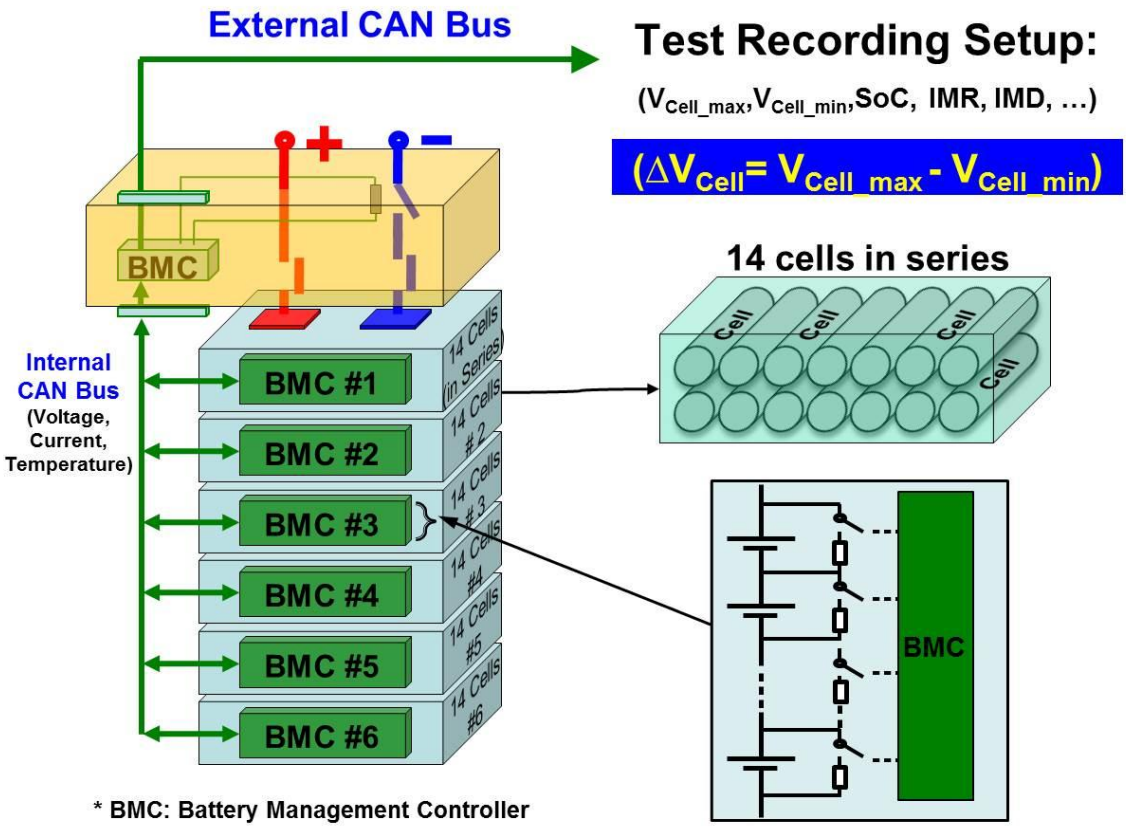

Figure 2.13 Resistive cell equalization for high voltage lithium-ion battery pack with CAN bus

The dissipation equalization methods, shown in Figure 2.13, control the switch on/off to dissipate energy from the corresponding paralleled battery cell. The final target would be dissipating the higher energy cell to be very close or equal to the minimum cell among the battery bank. Considering the natural characteristics of the cell imbalance described in 1.2.2, the cell which has a high self-discharge rate will continue to increase the imbalance level and ΔV_{Cell} will keep increasing. As a result of the equalization principle, all the higher cells will keep bleeding until the battery dies. Therefore, to prevent this condition from happening, the cell equalizer is only enabled with certain conditions. In this setup, the conditions include:

1) $V_{Cell\_Max} \geq 3.73V$;

2) $\Delta V_{Cell} \geq 30mV$;

The first condition is set to disable the cell equalizer when maximum cell voltage is less than 3.73V, which means that the cell SoC is around 50% and far from fully charge, therefore, the risk of overcharge is considered to be low. The second condition is the target of the cell equalization, which means that the battery pack is considered to be balanced when $\Delta V_{Cell} < 30mV$. 30mV is based on the conditions of tolerance of the cell voltage monitoring and battery over-charge risk. The cell equalization circuit will be enabled when the two conditions are both satisfied. For example, when the $V_{Cell\_Max} < 3.73V$, the cell equalizer is disabled and the imbalance will be continually worse during storage. Figure 2.14 shows the 800 hours of recorded data for ΔV_{Cell} for the dissipative cell equalization method. The horizontal axis is the time in hours and the vertical axis is ΔV_{Cell} in unit of Volts. This figure can be divided into three stages:

(1) Equalization circuit is disabled with $V_{Cell\_Max} < 3.73V$ during storage

As shown in Figure 2.14, ΔV_{Cell} continually increases all the way due to the mismatched cell self-discharge rate. When ΔV_{Cell} is approaching 0.3V, one battery regular charge is conducted for maintenance, and this charge increases the ΔV_{Cell} to 0.35V drastically. The major reason for this sharp increase is the deviation of the electric-chemical charging efficiency and cell impedance. This charge stops when V_{Cell_Max} touches 4.0V, the highest cell voltage limit. Considering V_{Cell_Max}>3.73V and ΔV_{Cell}>30mV, both the two cell equalization conditions are met and cell equalizer circuit is enabled.

(2) Equalization circuit is enabled

ΔV_{Cell} is decreasing linearly all the way down to 30mV at which the battery pack is considered to be balanced. Taking an average during this stage, it can be seen that the equalization speed is averaged at 25mV/day, quite slow compared to the battery's normal charge and discharge duties. For example, one fully charge 0%~100% SoC is roughly 2~4 hours, and the discharge duty to maintain non-coincidental load will be even shorter and unpredictable. Therefore, additional measures should be taken to protect the lithium-ion battery bank from overcharge/over-discharge considering the very low speed of the dissipative cell equalizer.

(3) ΔV_{Cell} maintenance stage.

Under ideal conditions, the ΔV_{Cell} will be maintained within a 30mV tolerance range and keep this condition until one condition fails. However, due to the regular charge and discharge, it is very likely that ΔV_{Cell} will increase over 30mV, which takes the cell equalizer tens of hours, or even days, for the battery to get back into balanced state again.

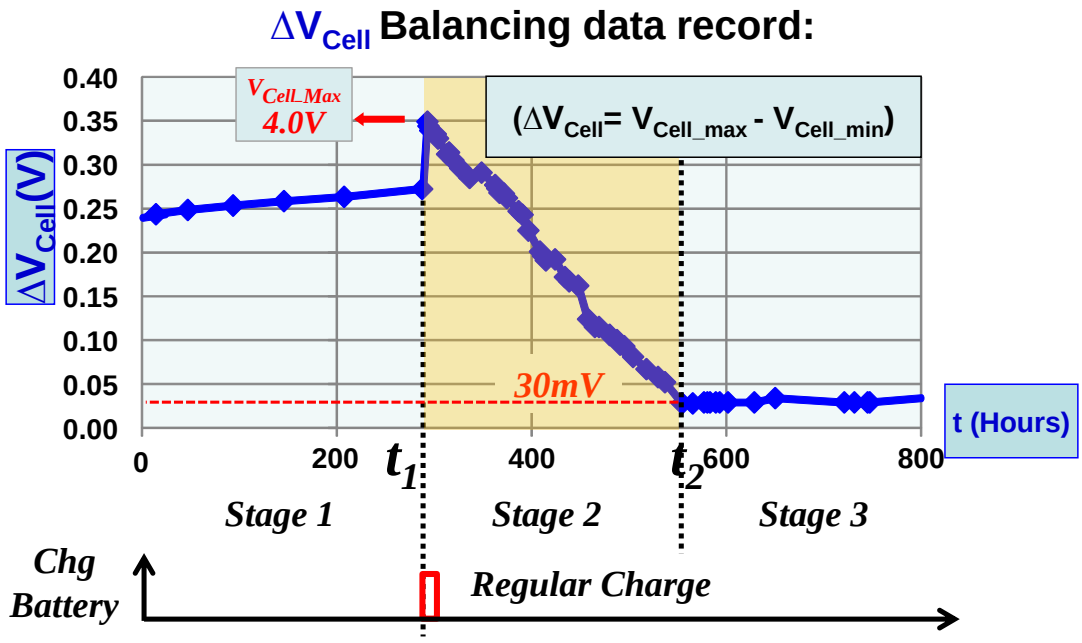

Figure 2.14 Performance of dissipating cell equalization method

One possible solution for this issue is to decrease the resistance value and speed up the bleeding speed. The corresponding sacrifice would be thermal management of the bleeding resistor, large size, heavy weight and related cooling system, which will further increases the system level cost and depreciate the benefit of the lithium-ion technology.

2.3 Non-dissipative Cell Equalization Techniques and Classifications

Non-dissipative methods, which are also called active cell equalization methods, apply power electronics circuit with the utilization of active devices to achieve equalization by transferring the energy among all the series connected lithium-ion cells. Different with the dissipative methods which bleed the energy in higher SoC cell into heat, non-dissipative methods recycle it. Non-dissipative methods have already been investigated extensively and discussed in [53]-[70], shown in Figure 2.15, and there are many topologies and solutions covering this issue.

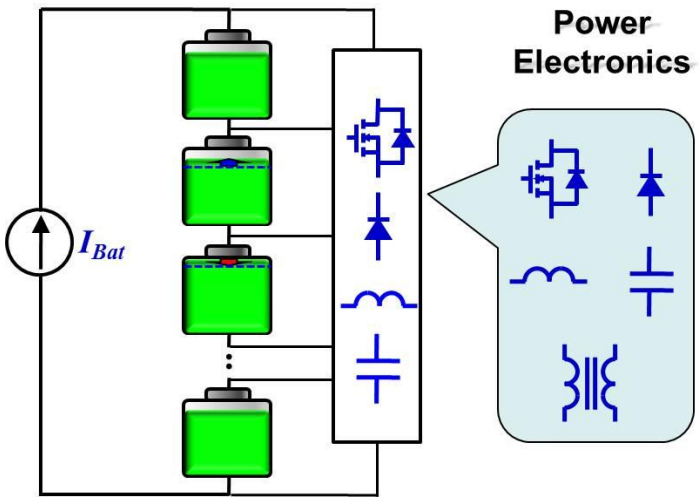

Figure 2.15 Non-dissipative Cell equalization with Power Electronics

However, there is no system-level study and classification of all the cell equalization methods with a comparison of pros and cons. To understand the equalization methods systematically for high voltage lithium-ion battery applications, an "Energy Flow Chart" categorization methodology is proposed to help understand the system-level design considerations. Figure 2.16 shows the basic concept of the energy flow chart, and it can be explained with the following perspectives:

1) Series connected cells are considered as one battery bank, providing a relative stable DC Link/Bus;
2) All the single cells are numbered from *#1* to *#n* for all the cells;
3) Energy storage components, like capacitors and inductors in power electronics equalization circuit, are represented as '***S***' for simplification. Besides, any common DC link/bus or battery pack can be used as energy storage and represented as '***S***';
4) Directed lines represent the energy flow with the arrow indicating the energy flow direction; a single arrow line for unidirection and a double arrow line for bidirectional energy flow.

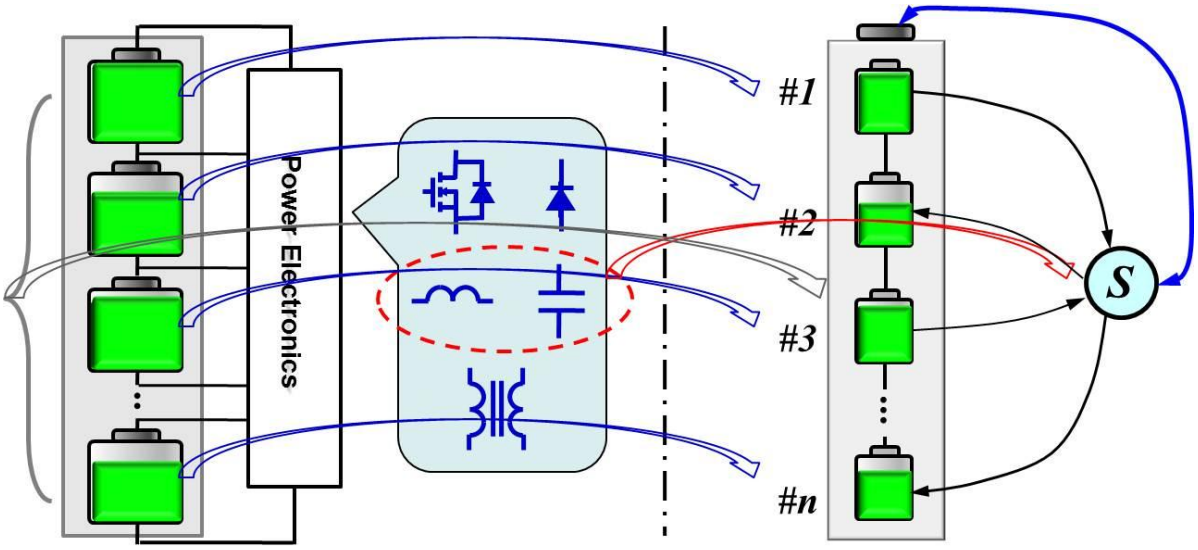

Figure 2.16 "Energy Flow Chart" for categorizing battery equalization

Based on this concept and study of the literature [53]-[70], four basic categories are generalized, shown in Figure 2.17. Importantly, the expressions of "higher SoC cells" and "lower SoC cells" during the discussion are all mentioned with comparison with average SoC.

I) Charging lower SoC Cells;

Energy discharged from a common DC link/bus or battery bank is first stored in '***S***', and then delivered to the lower SoC cells. (I) in Figure 2.17 shows the energy is from a common battery pack source.

II) Discharging higher SoC cells;

Energy discharged from higher SoC cells is firstly stored in ***S***, and then delivered to a common DC link/bus or battery bank. (II) in Figure 2.17 shows the energy is discharged to common battery pack source.

III) Selective cell charging/discharging;

Energy discharged from higher SoC cells is firstly stored in '***S***', and then delivered to lower SoC cells.

IV) Shuttling;

The energy storage components equalize two adjacent battery cells by bidirectional energy flow and every two adjacent cells share one circuit with one energy-storage component. Therefore, N series connected cells needs N-1 equalization circuit.

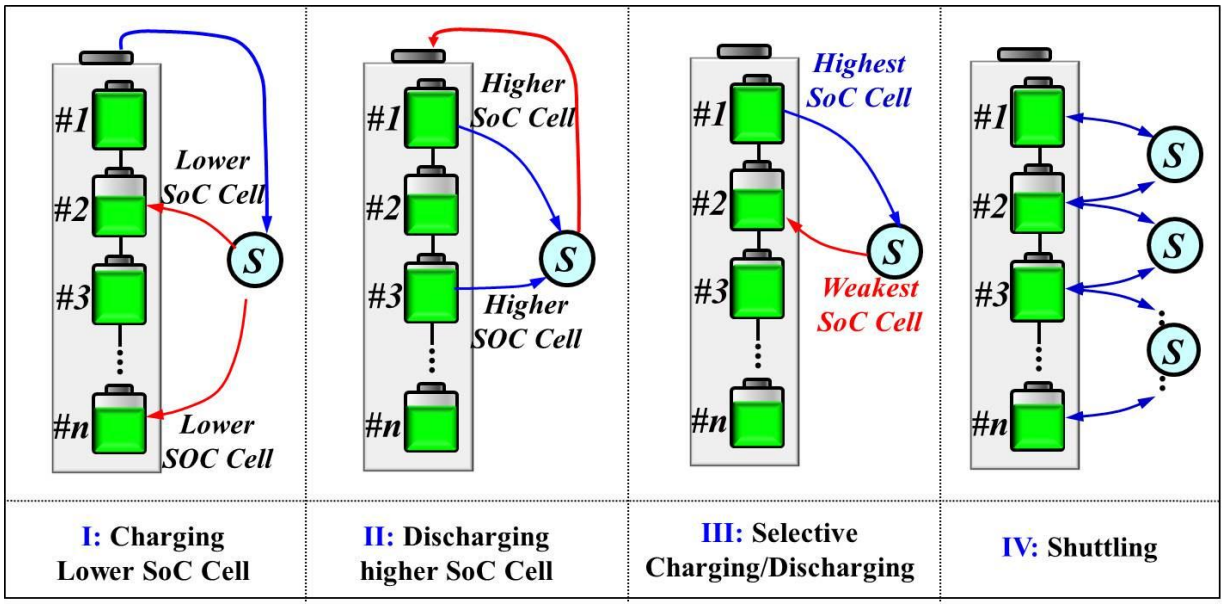

Figure 2.17 Four basic non-dissipating equalization methods

To further illustrate the concepts in the perspective of power electronics circuits, popular equalization circuit examples are studied and evaluated with the proposed energy flow chart concepts. Figure 2.18 shows one example with multi-winding Flyback circuit for category I [55][56]. The primary winding is connected with the high voltage battery back as an energy source, which is used to charge the primary coupled inductor of the Flyback converter, and a multi-secondary winding is connected to individual cells. Assuming symmetrical leakage inductances for all the secondary windings, the lowest SoC will clamp the coupled inductor winding voltage during off state of the primary switch, thus, the least SoC cell will get most of the energy transfer during normal operation. The benefits include simple control of the primary side and many cells share one converter for equalization. However, for a long string battery bank

of up to 100 cells, the fabrication for the transformer with up to 100 secondary windings will be very difficult and can lead to a mismatched leakage inductance, further degrading the circuit performance. However, this method can be used to balance among modules of the battery bank.

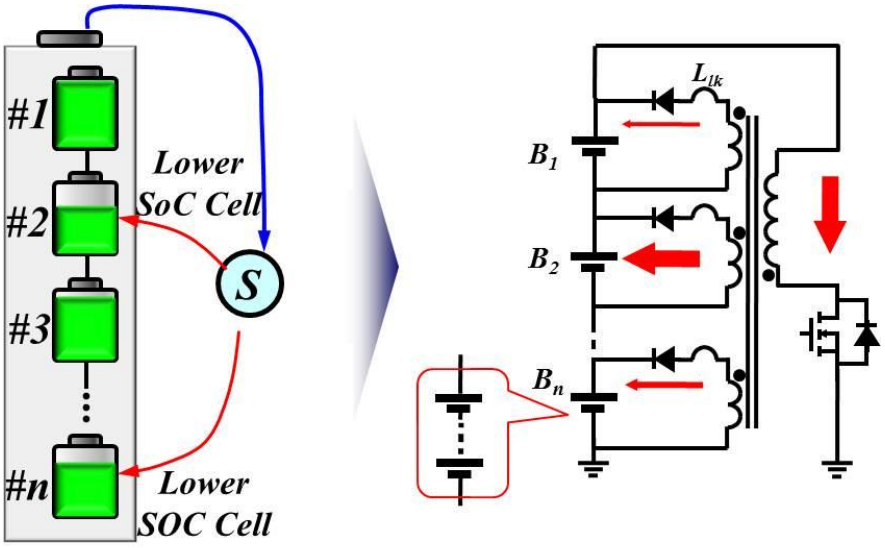

Figure 2.18 Circuits example of category I – Charging lower SoC Cell

Figure 2.19 (a) shows one example with a multi-winding Flyback circuit for category II [55]. Different with Figure 2.18, the Flyback converter has a multi-winding in the primary side and shares one secondary winding. There will be only one primary side working at a time to discharge the higher SoC cell, and then deliver the stored energy to the total battery bank. Beside the pros and cons illustrated in category I, the control is more complicated in this circuit, since the active switch number is as the same as battery cell number. Circuit show in Figure 2.19 (b) [57] [58] [59] [60] has a different configuration with a modularized concept – each battery cell applies one switch and one inductor, extremely simple buck-boost converter. The operation principle is still a buck-boost concept with one or multi-cell converter at a time as a buck-boost operation. However, this topology has a very high voltage stress on the active switches, as high

as the battery bank voltage up to N×V_{Cell}. Moreover, it is difficult to design an inductor for multi-cell charging/discharging operation.

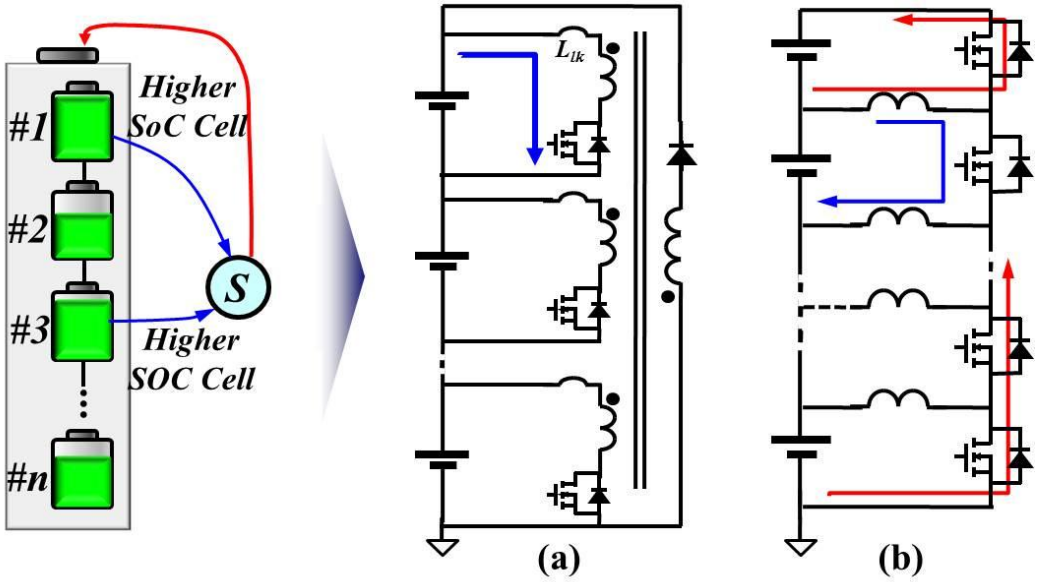

Figure 2.19 Circuits example of category II – Discharging higher SoC cell

Figure 2.20 shows one example of category III [62] – selective charging/discharging. One implementation with multiple diodes and active switches is addressed in [61] which uses active switches or solid state relay to control which cell(s) is (are) connected for operation. [62] divides the battery bank into two groups, and the control implementation will connect the maximum SoC in group 1 and minimum cell in group 2 with the isolated bidirectional DC-DC converter to achieve equalization. Similarly, maximum SoC cell in group 2 also can be connected to minimum SoC cell in group 1 for equalization. The benefit of this control is using a single converter concept; however, the bidirectional blocking switch has high voltage stress, up to N×V_{Cell}, and the control is extremely complicated. What is more, only two cells are involved in the equalization operation.

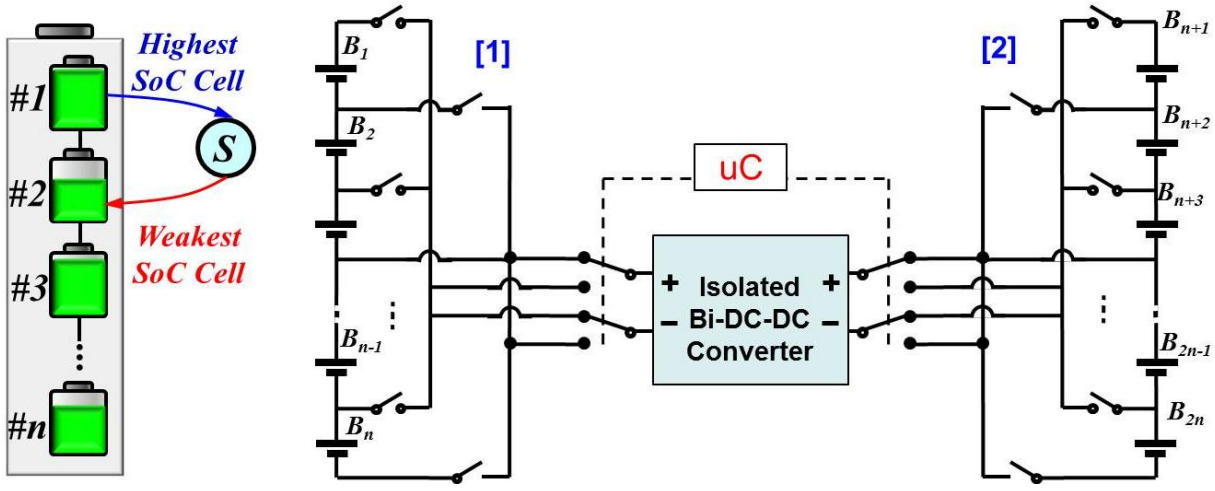

Figure 2.20 Circuits example of category III – Selective charging and discharging

Figure 2.21 shows the shuttling method for category IV. Every two adjacent cells share on individual cell equalizer (I.C.E) which is a bidirectional converter equalizing these two cells. For a battery bank with N cells needs N-1 of I.C.E for full implementation. Considering the circuit for I.C.E, Figure 2.22 shows that the I.C.E converter with inverse output will work for this application, such as buck-boost converter as the simplest one with two active switches and one discrete inductor [63][64][65]. Figure 2.23 shows another configuration with switched capacitor (SC) as the I.C.E. converter [66][67][68] with 4 active switches and one storage capacitor. Adding one small inductor in series with the capacitor will turn this circuit to soft-switching [68].

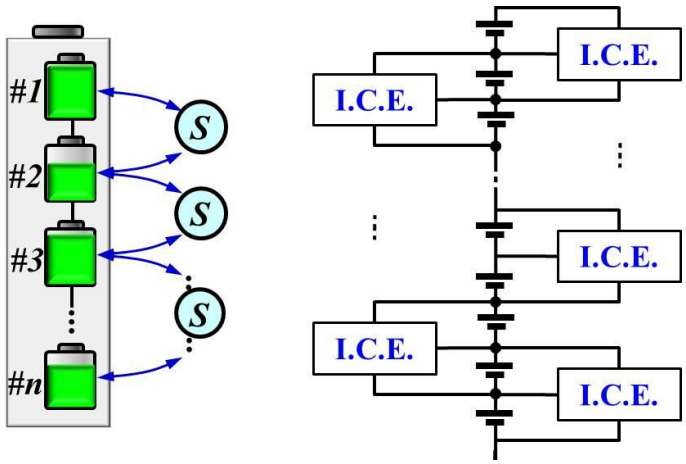

Figure 2.21 Circuits example of category IV - Shuttling

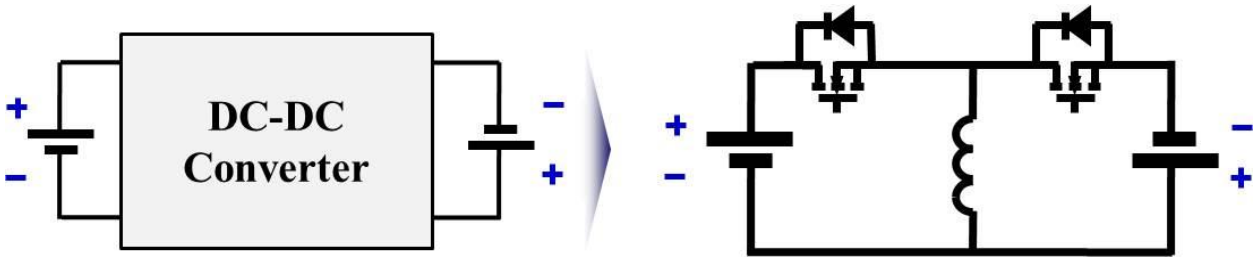

Figure 2.22 Buck-boost circuit as individual cell equalizer

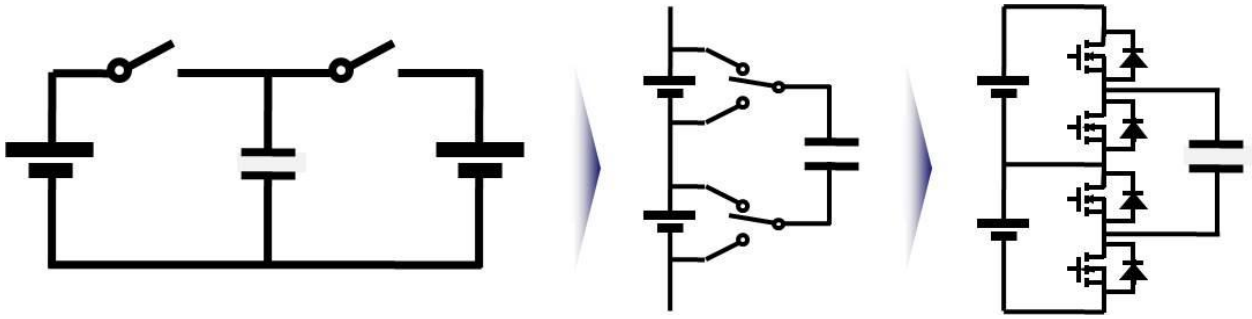

Figure 2.23 Switching capacitor as individual cell equalizer

The benefits of shuttling method include: 1) low voltage stress, $2\times V_{Cell}$ for buck-boost shuttling and $1\times V_{Cell}$ for switched capacitor; 2) no magnetics in switched capacitor – high power density; 3) modular design; 4) very simple in control for switched capacitor [68], as shown in Figure 2.24, with 50% duty cycle and soft-switching. However, the efficiency is quite low when the string number is increased up to 100 cells. For example, in the worst scenario, the top cell is the highest SoC and the lowest is at the bottom, then the total efficiency is $\eta_{Tot} = \eta_{I.C.E}^{99} < 15\%$ (Assumption: 100 cells and 98% efficiency for I.C.E).

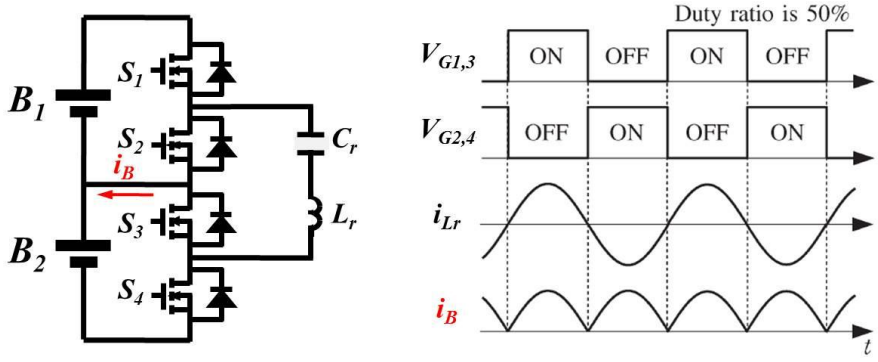

Figure 2.24 Control of soft-switching switched capacitor

To summarize all four types of the non-dissipative cell equalization circuits, Figure 2.25 list all the potential benefits and drawbacks for each non-dissipating cell equalization category, and it can be found that the shuttling methods are considered to be better than the other three categories because of the simple control, no magnetic, modular design and low voltage stress.

	Pros	Cons
Charging Lower SOC Cells ☺☺	1) Simple control; 2) One Converter;	1) Fabrication difficulty; 2) Not suitable for long string
Discharging Higher SOC Cells ☺	1) One extremely simple buck/boos per cell;	1) Complicated control; 2) High voltage stress; 3) Difficult inductor design;
Selective Charging/Discharging ☺	1) One converter;	1) Complicated control; 2) High voltage stress; 3) High cost; 4) Prolonged Equal. time;
Shuttling ☺☺☺☺	1) Simplest control (SC); 2) No Magnetic Pat(SC); 3) Modular design; 4) Low voltage stress;	1) Lower efficiency for long battery string; $\eta_{TOT} = \eta_{I.C.E.}^{N-1}$

Figure 2.25 Summary of four categories of non-dissipating cell equalization methods

2.4 Proposed Li-ion Battery Charging Profile base on $V_{Cell\_Max/Min}$ Monitoring

2.4.1 Overcharge of lithium-ion battery with conventional charging profile

Comparing the performance of dissipative and non-dissipative cell equalization methods, discussed in section 2.2 and 2.3, the non-dissipative cell equalization definitely increases the equalization speed, and the corresponding equalization period is decreased significantly, from days to hours for a high energy lithium-ion battery cell around 50Ah [17][66][70], which is good in terms of efficiency and speed. However, considering the level-2 charger can fully charge battery within 1~4 hours and level-3 charging within less 0.5h, the equalization speed is still not

fast enough which can guarantees the balance of the battery bank, and the condition will be even worse at non-coincidental load transition which happens in less than microseconds.

Therefore, under a typical lithium-ion battery constant current (CC)→constant voltage (CV) charging profile, shown in Figure 2.26, the battery charger, which treats the whole battery as one unit, may put the battery into danger—overcharge or over-discharge under unbalanced conditions. Figure 2.27 shows the typical battery charger implemented with the typical CC-CV charge profile, and the outer voltage loop kicks into control as soon as the battery pack voltage touching 336V (84×4Volts). Considering cell imbalance, this charge profile will have some cells' voltage exceeding 4.0V while other cells' voltage is still below 4.0V when the battery pack is fully charged to 336V. The cells with voltage over 4.0V will lead to overcharge. As discussed in [48][49], lithium-ion battery cannot withstand overcharge, for the charging efficiency lithium-ion battery is nearly 100%, and overcharge will definitely hurt the battery cycle life and even damage the lithium-ion battery cell, or even catch fire. This over-charge risk under cell imbalance can also be applied to over-discharge as long as the battery pack voltage is considered as the protection reference. Therefore, careful measures should be taken to prevent the overcharge and over discharge risk, since the charger must stop charging when the highest SoC cell is fully charged, and should stop discharging when lowest SoC is fully discharged.

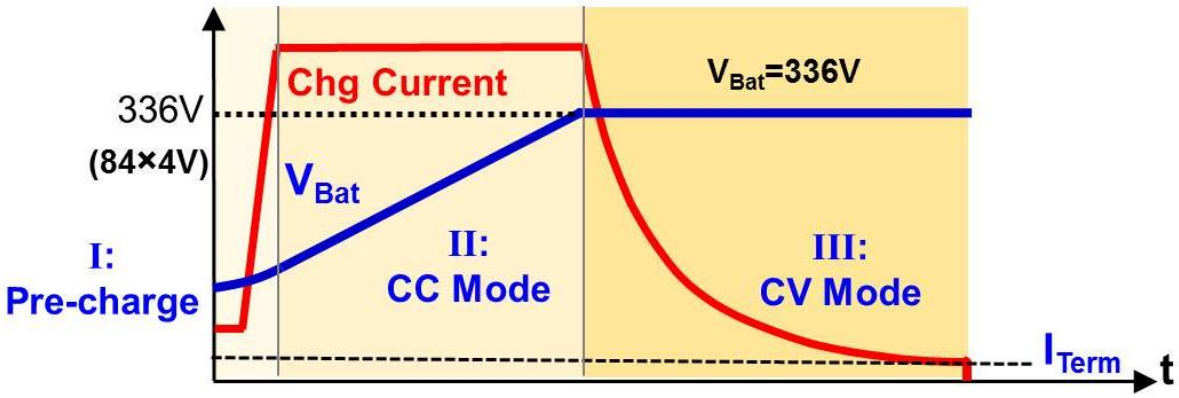

Figure 2.26 Typical CC→CV charging profile

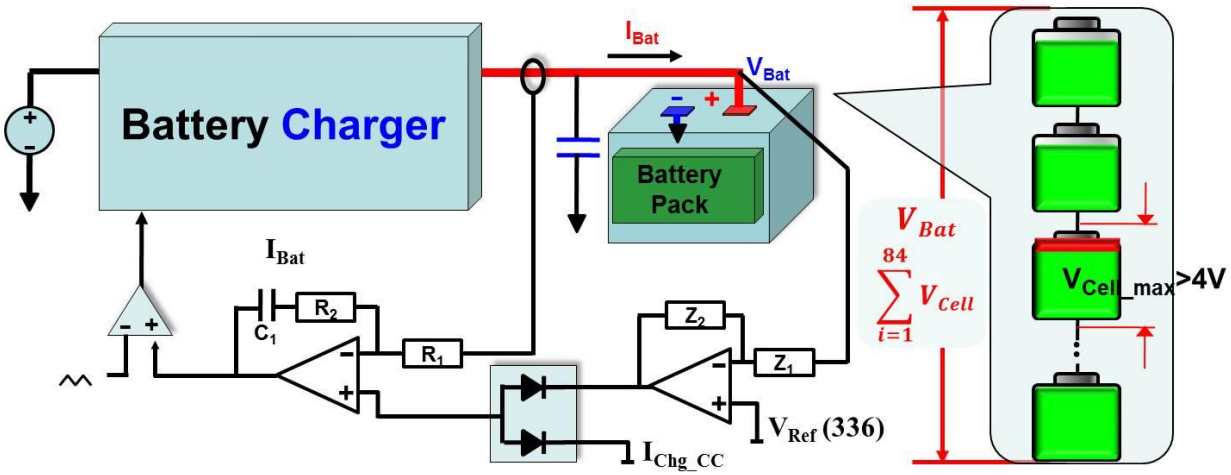

Figure 2.27 Overcharge at typical CC→CV charging profile considering battery bank voltage

Traditionally, in order to protect lithium-ion battery from being overcharged, the maximum cell voltage, V_{Cell_Max}, is monitored and the charger will be shut down as soon as V_{Cell_Max} is reaching certain protection level [71], shown in Figure 2.28. Normally the protection level is set a little bit higher than the allowed maximum limit to speed up the charging process. In Figure 2.28, the charger is shut down and charging current is zero when V_{Cell_Max} hits 4.2V (4.0V is the fully charged voltage for the NCA Li-ion cell). This method can save the Li-ion cell from being severely overcharged; however, it is 0.2V higher than the rated maximum limit, and it needs a multi-start-stop charge to fully charge battery pack. Multi-start/stop means multiple charge/discharge, which also leads to increased cell degradation.

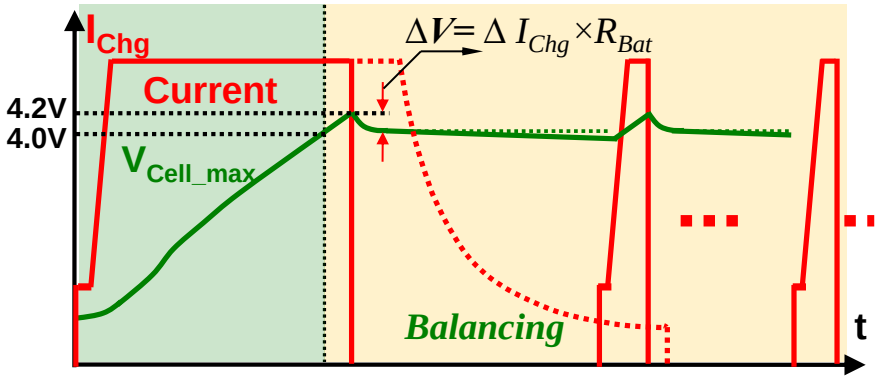

Figure 2.28 Multi-stop charging for lithium-ion battery protection

Another method is to decrease the charging current when V_{Cell_Max} hits the top limit, shown in Figure 2.29. The charge current decreases by ΔI_{Chg} when V_{Cell_Max} hits the top limit, 4.0V. The advantage of this method over the start-stop in Figure 2.28 is that it does not stop the charger; however, it is hard to find the optimal ΔI_{Chg}. Larger ΔI_{Chg} will increase the charging period and smaller ΔI_{Chg} will lead to cell overcharge.

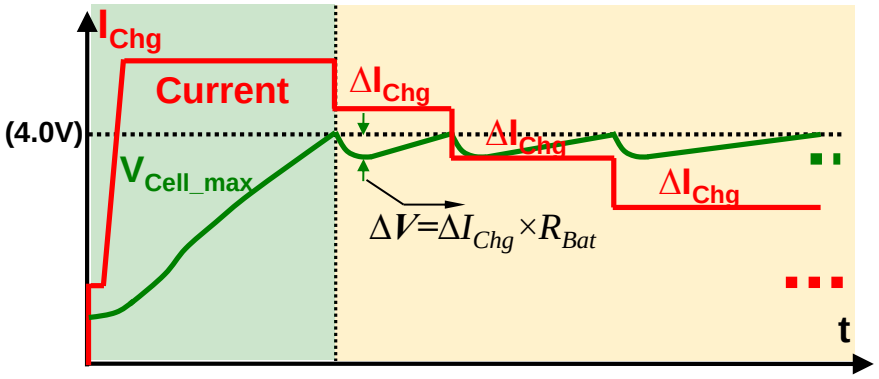

Figure 2.29 Decreasing charging current for lithium-ion battery protection

2.4.2 Proposed Li-ion Battery Charging Profile base on $V_{Cell\_Max/Min}$ Monitoring

A battery management system, shown in Figure 2.30, is normally configured with four major functional parts, 1) high voltage series/parallel connected lithium-ion battery pack with the related integrated thermal dissipating system; 2) bidirectional battery charger or discharger; 3) battery management controller (BMC), which includes cell equalization, sensing and monitoring, like temperature, fault, the battery pack voltage and current, every cell voltage, SoC, state of health (SoH), state of function (SoF). For example, the available charging and discharging current rating is a function of temperature, mentioned in 2.1.1; 4) protection, which normally consists of redundant high voltage DC circuit breaker, contactor or fuse to protect the battery from overcharge/over-discharge, short circuit, over-rated current charge/discharge, over temperature and so on.

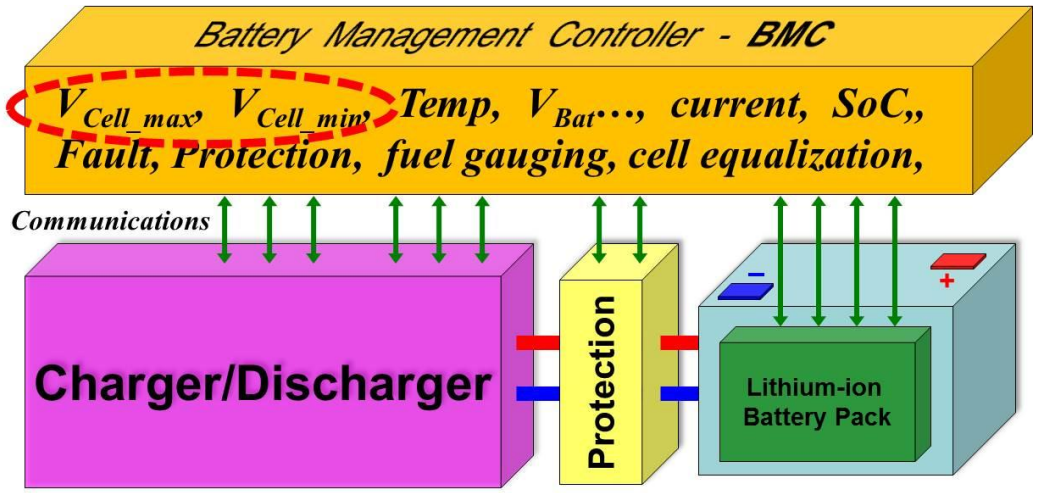

Figure 2.30 Lithium-ion battery system configuration

Among all the monitored information, V_{Cell_Max} and V_{Cell_Min} are very critical, since $V_{Cell\_Max/Min}$ decides when the charger should stop charging/discharging. With the utilization of this critical message, a modified charging profile based on $V_{Cell\_Max/Min}$ monitoring is proposed to protect the Li-ion battery and fully charge battery in one cycle, making full utilization of the Li-ion battery capacity.

Taking the V_{Cell_Max} for illustration, Figure 2.31 shows V_{Cell_Max} controlled charging control configuration. As is different with Figure 2.27, the outer voltage loop does not applied the battery pack voltage, however, it applies the V_{Cell_Max} information obtained from the CAN bus of the battery management controller (BMC). After the constant current (CC) charging period controlled by the current loop with I_{Chg_CC} as the reference, the V_{Cell_Max} controlled outer voltage loop kicks into control as soon as the maximum cell voltage V_{Cell_Max} touches the allowed cell voltage limit (V_{LMT_High}), 4.0V in the example. Figure 2.32 shows the corresponding waveforms under the V_{Cell_Max} controlled constant voltage (CV) charging profile for a battery bank with the dissipative cell equalization method in 2.2, including charging current (I_{Chg}), two cell voltage (V_{Cell_Max} and V_{Cell_Min}), and battery bank voltage (V_{Bat}). Generally speaking, this charging profile

is initiated with pre-charge (≈1/10C) and is followed by the constant current (CC) charge. The final stage is constant V_{Cell_Max} controlled charging profile. Operation waveforms can be divided into 4 sections:

I: [t_0~t_1]: Pre-charge stage;

Charge battery with around C/10 current rating to bring the battery voltage into a safe range, typically ≥ 2.7~3.0V; The major concern of a high current charge at a low SoC is overheating, since the impedance of Li-Ion cell is high at low SoC conditions;

II: [t_1~t_2]: Constant current charge with cell equalization disabled;

This stage with high current charging will linearly increase the SoC, as well as the cell voltage. Before the maximum cell voltage is less than 3.73V, the cell equalizer is disabled (refer to section 2.2), therefore, all the cells are charged with the same current.

III: [t_2~t_3]: Constant current charge with cell equalization enabled;

When both the cell equalization conditions are met (V_{Cell_Max}≥3.73V & ΔV_{Cell}≥30mV), the cell equalizer circuit is enabled and the higher SoC cells are bypassed with a certain amount of current through the switch controlled resistor. Therefore, the charging speed of the higher SoC cells, V_{Cell_Max} for example, in Figure 2.32, is slightly slower than the low SoC cells, V_{Cell_Min} for example. This stage ends when the maximum cell voltage, V_{Cell_Max}, touches high cell voltage limit, V_{LMT_High}, which is 4.0V.

IV: [t_3~t_4]: Constant V_{Cell_Max} controlled charging;

This stage starts as soon as V_{Cell_Max} reaches 4.0V, and V_{Cell_max} controlled loop will regulate V_{Cell_Max} to be a constant value (4.0V). When V_{Cell_Max} reaches

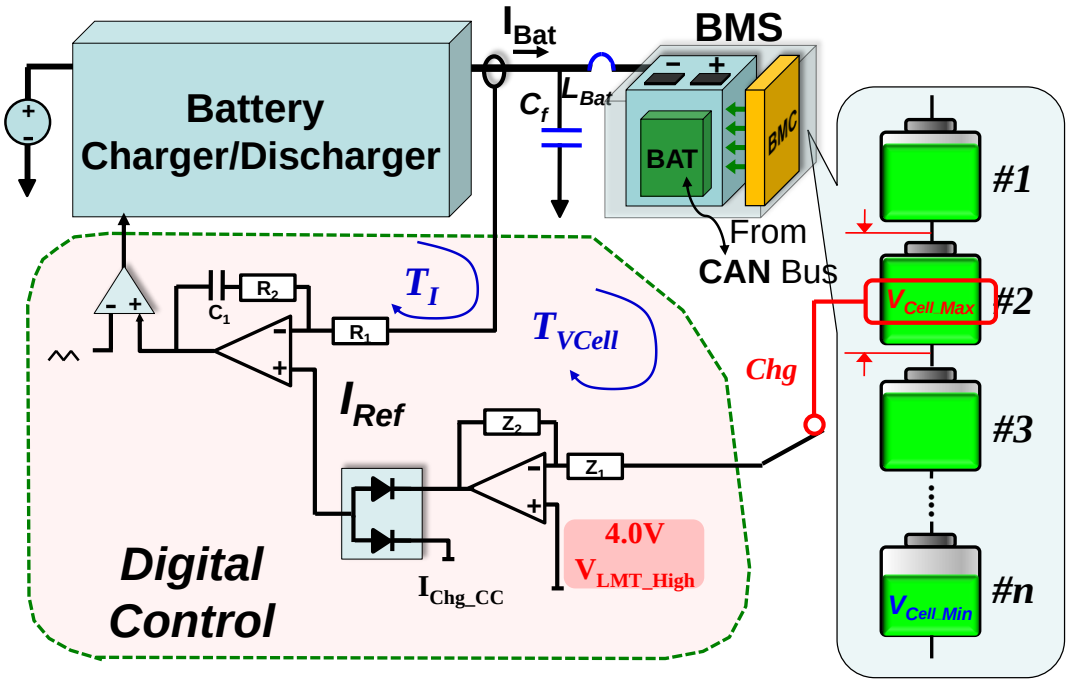

Figure 2.31 Control block for proposed charge profile based on V_{Cell_Max} monitoring

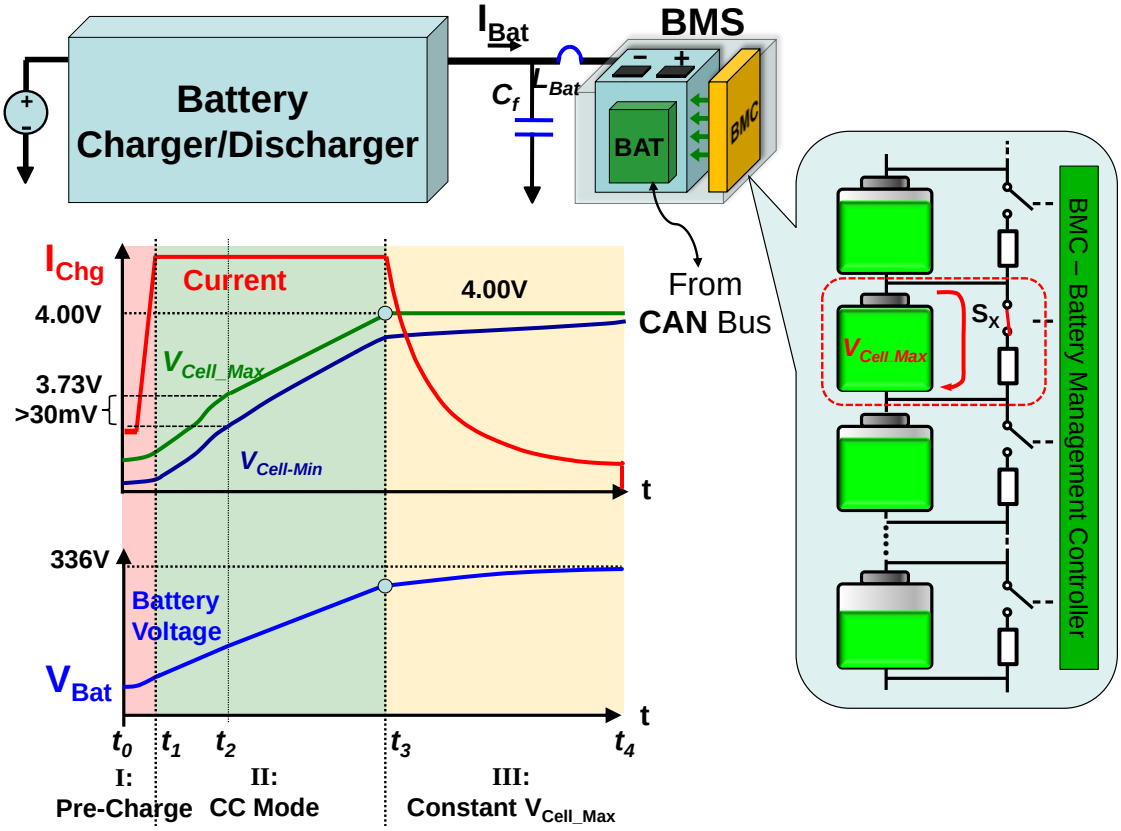

Figure 2.32 Operation illustration for proposed charge profile based on V_{Cell_Max} monitoring

4.0V, the whole battery pack is still under the equalization process and other cells' voltage is under 4.0V; therefore, the battery pack voltage, V_{Bat}, is less than 336V at the moment of t_3. As V_{Cell_Max} controlled charge continues, V_{Bat} increases slowly because the higher SoC cells are bleeding energy (Switch, S_X in Figure 2.32, is closed and bypassing certain amount of current) and have lower equivalent charging current compared to the lower SoC cell. Finally, V_{Bat} reaches 336V when all the cells are well balanced. The above mentioned process will definitely prevent the lithium-ion battery cell from being overcharged and can fully charge the battery bank within one charge cycle.

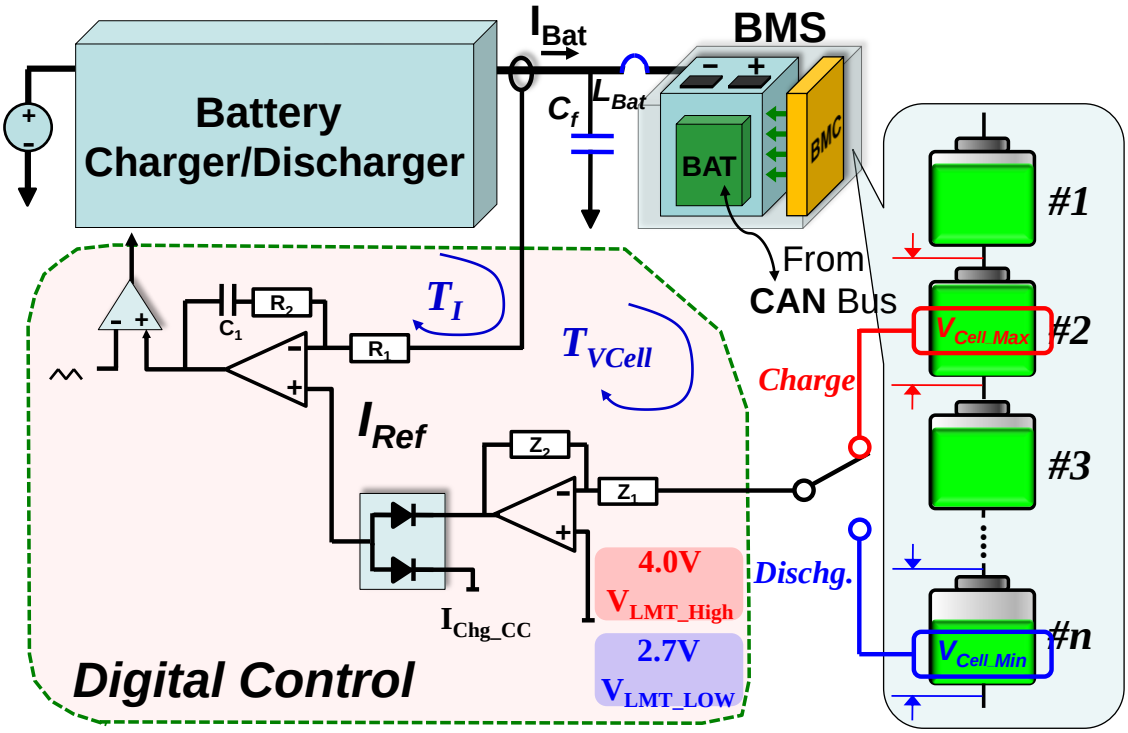

Figure 2.33 Control of proposed charge profile based on $V_{Cell\_Max/Min}$ monitoring

Comparing V_{Cell_Max} and its influences, V_{Cell_Min} is of great importance during discharging. During discharge operation, the battery charger is regulating the load side voltage, and the battery side voltage is normally not considered when total battery voltage is within the safe

operation range. The principle of risk for over discharge considering the mismatching is similar to the overcharge issue described in 2.4.1. Similar to the V_{Cell_Max} controlled charging profile, V_{Cell_Min} controlled discharging will set the limit maximum discharging current. The detailed control principle for V_{Cell_Max} and V_{Cell_Min} is summarized in Figure 2.33. Detailed illustration is not repeated here.

2.4.3 Design Considerations and Experiment of $V_{Cell\_Max/Min}$ Controlled Charging Profile

To implement this control in a DSP controller with the CAN bus communication, the sample rate of the V_{Cell_Max} is an important factor to be considered. The CAN Bus implemented in this system is operating at 250kbps, and the V_{Cell_Max} information updated at DSP controller is only 10Hz, since there are hundreds of information sharing the bandwidth, which means the V_{Cell_Max} controlled outer voltage loop T_{VCell} cannot be designed to have high bandwidth. Importantly, the switching frequency of the bi-directional charger is 30kHz, and it is practical to design the inner current loop T_I bandwidth to be around kilohertz range, which is very much higher than the V_{Cell_Max} controlled outer voltage loop T_{VCell}, shown in Figure 2.34. Therefore, comparing the outer voltage loop bandwidth, which is lower than 5Hz, the inner current loop output $\hat{I}_{Bat}$ follows the current reference $\hat{I}_{Ref}$ very well and does not affect outer voltage loop T_{VCell} design. Then, the closed inner current loop transfer function from $\hat{I}_{Ref}$ to $\hat{I}_{Bat}$ — G_I can be considered to be 1 for T_{VCell} loop design, listed in (2.5),

$$\boldsymbol{G_I = \frac{\hat{I}_{Bat}}{\hat{I}_{Ref}} = 1} \tag{2.5}$$

Then, the outer V_{Cell_Max} controlled voltage loop gain T_{VCell} can be simplified to (2.6),

$$\boldsymbol{T_{VCell} = G_{CV} \cdot Z_{Filter}(s) \cdot Z_{Bat}(s) \cdot R_{DIV}(s) \cdot e^{-s \cdot 0.1}} \tag{2.6}$$

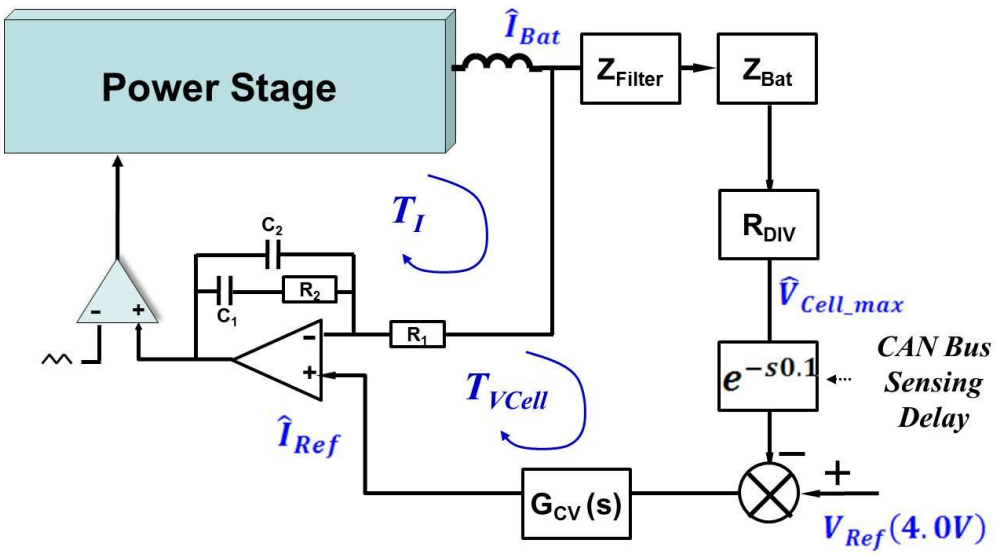

Figure 2.34 V_{Cell_max} Loop Design Considerations

Where G_{CV} represents the V_{Cell_max} controlled voltage loop compensator (2.7), refer to Figure 2.33; and the load $Z_L(s)$ represents the combined impedance of battery and filter, L_{Bat}, as the filter and parasitic inductance, is shown in (2.8); $R_{DIV}(s)$, the voltage divider, is shown in (2.9),

$$\boldsymbol{G_{CV} = \frac{Z_2}{Z_1}} \tag{2.7}$$

$$\boldsymbol{Z_L(s) = (1/sC_f)//(sL_{Bat} + Z_{Bat})} \tag{2.8}$$

$$\boldsymbol{R_{DiV}(s) = \frac{Z_{Bat}}{s \cdot L_{Bat} + Z_{Bat}}} \tag{2.9}$$

Moreover, $e^{-s \cdot 0.1}$ represents the V_{Cell_max} information updating delay, 10Hz, 0.1seconds, and Z_{Bat} is the impedance of the battery pack. Based on the battery manufacturing manual and equivalent circuit model [73], the battery model applied for the designed system is following Figure 2.35, the resistive model. Figure 2.35 (a) shows the high frequency resistive model, and Figure 2.35 (b) shows the low frequency resistive model considering voltage source to be a super capacitor to

represent the low frequency dynamic performance. Considering the T_{VCell} loop bandwidth is as low as a few hertz, Figure 2.35 (b) is applied for $Z_{Bat}(s)$ expression. The simplified battery SPICE model addressed in 2.1.3 could be used for the small signal model with the parameter C_{bat} and R_{Int} in Figure 2.35 referring from the value from 2.1.3. The target bandwidth of the V_{Cell_Max} is set to be 1Hz with a phase margin around 50 °degrees, the compensator G_{CV} can be configured as one simple integrator.

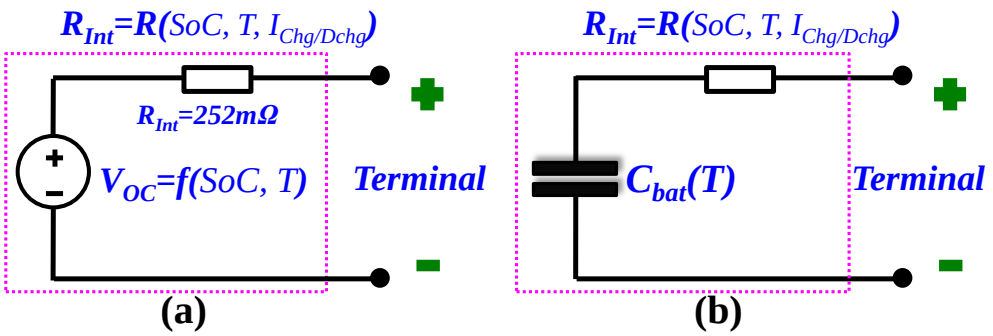

Figure 2.35 Low frequency lithium-ion battery model

Figure 2.36 shows the 8.4kW experimental results of V_{Cell_Max} control. In Figure 2.36, the green line in the top is the battery charging current; the pink and purple line in the middle are showing the inductor current of phase 1&2 (Three-phase interleaved bi-directional buck/boost converter is implemented); the blue line are V_{Cell_max} signal, manually drawn according to the data read from CAN bus. Importantly, there are several points addressed below to understand Figure 2.36:

1) Figure 2.36 is capturing around 26mins waveform with 125 sampling per second;

2) V_{Cell_max} information, blue line, is manually drawn in scale to help understand the step-chang battery charging current.

3) V_{Cell_max} is read from CAN bus, and the updating frequency is 10Hz with minimum change of 0.001V, the 1mV resolution causes charge current step change;

4) V_{LMT_High} is set to be 3.950V for this experiment.

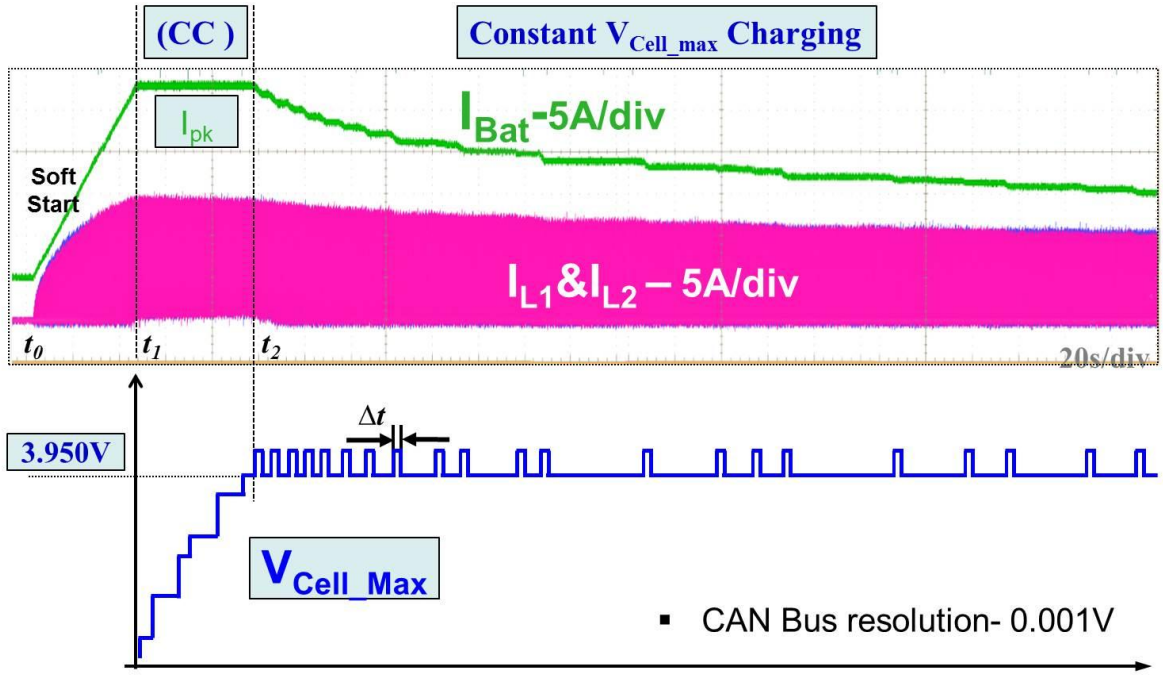

Figure 2.36 Experiment results of the proposed battery charge profile with $V_{Cell\_Max/Min}$ monitoring

Figure 2.36 can be divided into 3 stages:

[t_0~t_1]: After the Pre-charge stage, battery charging current I_{Bat} is ramping to the constant charging stage, 20A for this experiment;

[t_1~t_2]: Constant current charging stage; charging current keeps constant, and the V_{Cell_max}, in blue line, is increasing linearly;

[t_2~t_3]: V_{Cell_max} controlled charging stage; the V_{Cell_max} in this stage remains constant around 3.950V, and the 0.001V step change only lasts for less than tens of mini-seconds in the real experiment and the 0.001V step change period in Figure 2.36 is intentionally enlarged for easy understanding. The reason for the step change condition is that the CAN bus resolution is 1mV which is fairly accepted by the lithium-ion battery requirement.

2.5 Smart Battery Module based Integrated Charger and Cell Equalizer

An active cell equalization method survey in [74], summarized in 2.3, shows all the state-of-the-art solutions with detailed pros and cons. Based on all the reviewed solutions, three better candidates are selected for discussion. Figure 2.37 shows the three candidates.

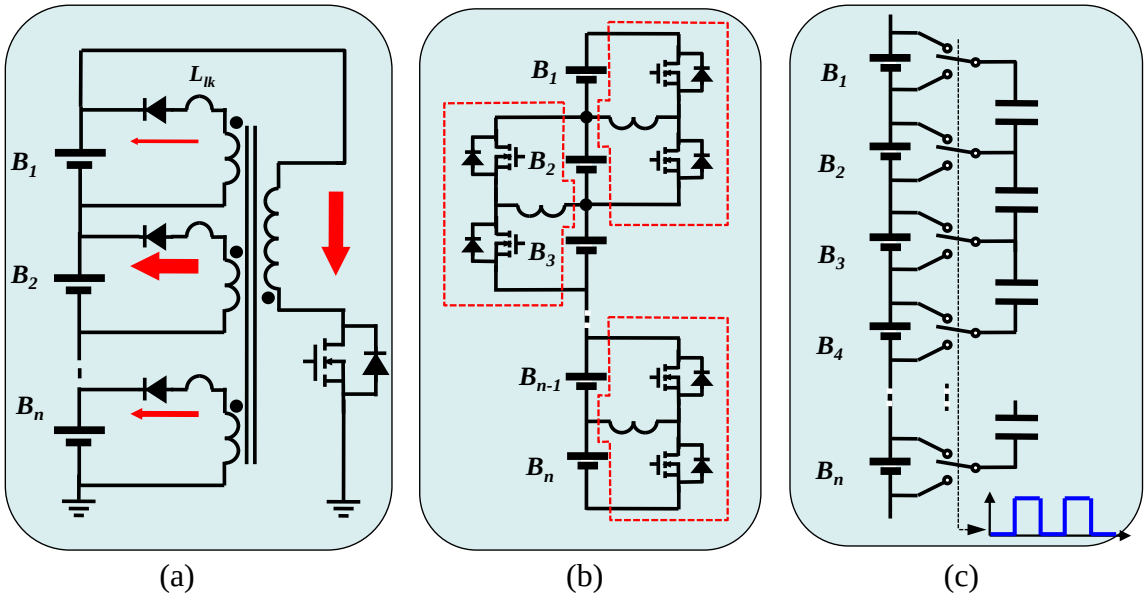

Figure 2.37 Active cell equalization candidates

The 1st one, shown in Figure 2.37 (a), is a multi-winding output Flyback converter (isolated switch inductor) based cell equalizer. This method discharges the energy from the battery pack when the primary switch is on, and charges all the cells when the switch is off. Importantly, the cell which has the lowest SoC receives the most energy, as shown with the red arrow thickness in Figure 2.37 (a). The pros and cons of this converter includes: 1) many cells share one converter; 2) simple control; 3) not suitable for large strings for the leakage inductance deviation when the number of the secondary winding is increasing. The 2nd one, shown in Figure 2.37 (b) is buck-boost converter-switched inductor converter-based cell equalizer. This method contains multi-buck-boost converter unit between each adjacent battery cell to achieve battery

equalization. The pros and cons of this method include: 1) low voltage stress for the active switch; 2) modular design; 3) low efficiency in long strings. The worst case happens when the energy transfer from the top cell to the bottom cell during which the energy shall pass all the stages of the buck-boost unit. Even though the efficiency of each stage is high, however, a multi-stages converter in series would decrease the efficiency to η^{N-1}, while N is the number of the cells. The 3rd method is a switched capacitor circuit, which is very simple in control, low voltage stress and modular design. However, it still bears the low efficiency characteristic as the switched inductor solution. Comparing these three circuits, each solution has its pros and cons when the cell number of the strings is increasing.

For the battery system packaging in (P)HEV, the individual cells are firstly modularized, then, the battery bank is then arranged with battery modules [75][76][77][78], which provides better mechanical strength, better room filling factor and higher reliability. This idea can be borrowed and extend to battery equalization architecture. [69][70] mentioned modularized concept for cell equalization design. Figure 2.38 shows the modularized concept with intro-module and inter-module equalizer. Firstly, the battery pack is grouped into different modules, from module 1 to M. Then, every module has an intro-module equalizer to balance the cells in each module, and the inter-module equalizer balances the energy among different modules. The intro-module has a large cell number; therefore, solutions with low cost and simple control are preferable, such as switched inductor and switched capacitor. On the other hand, the inter-module equalizer has smaller module numbers; therefore, solutions with high efficiency solutions are preferable, such as switched inductor， switched capacitor and isolated switched inductor. Combining the intro- and inter- module solutions together, Figure 2.39 give one example of the concept with the switched capacitor as the intro-module equalizer and Flyback as

the inter-module equalizer. All these modularized hybrid active cell equalizers take the advantage of the benefits of all the candidates, as shown in Figure 2.37. What is more, the modularized hybrid active cell equalizer can apply the proposed charging profile based on the $V_{Cell\_Max/Min}$ monitoring, shown in Figure 2.40, which can be considered as a system solution for high voltage lithium-ion battery system, i.e. Integrated charger and modularized cell equalizer. The proposed solution can protect the lithium-ion cell from being overcharged/over-discharged with full utilization of the battery capacity. However, it introduces one more stage, the inter-module equalizer, and will consequently increase system design cost and complexity.

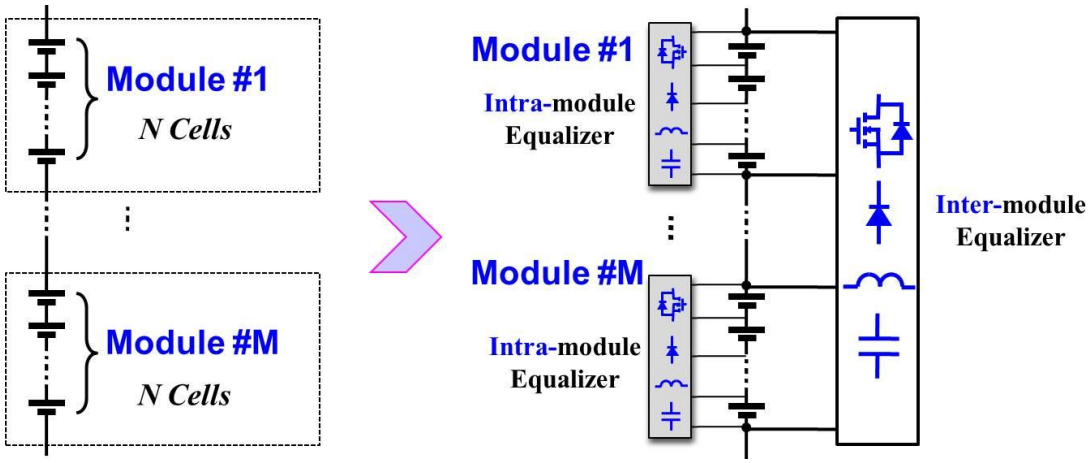

Figure 2.38 Modularized cell equalization architecture

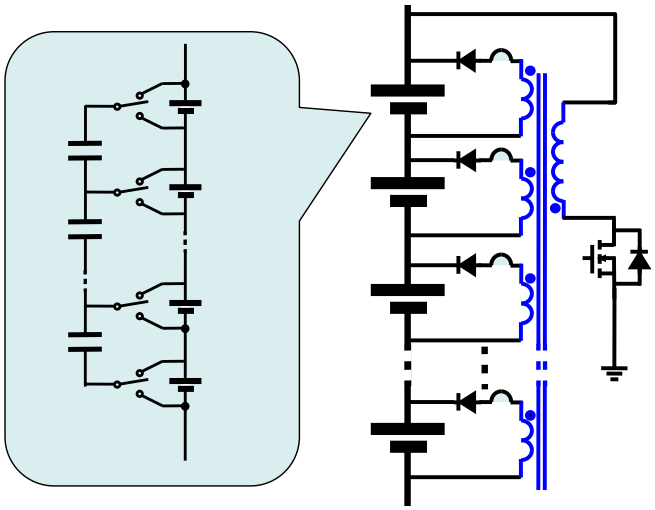

Figure 2.39 Equalization with switched capacitor (Intro-module) and Flyback (Inter-module)

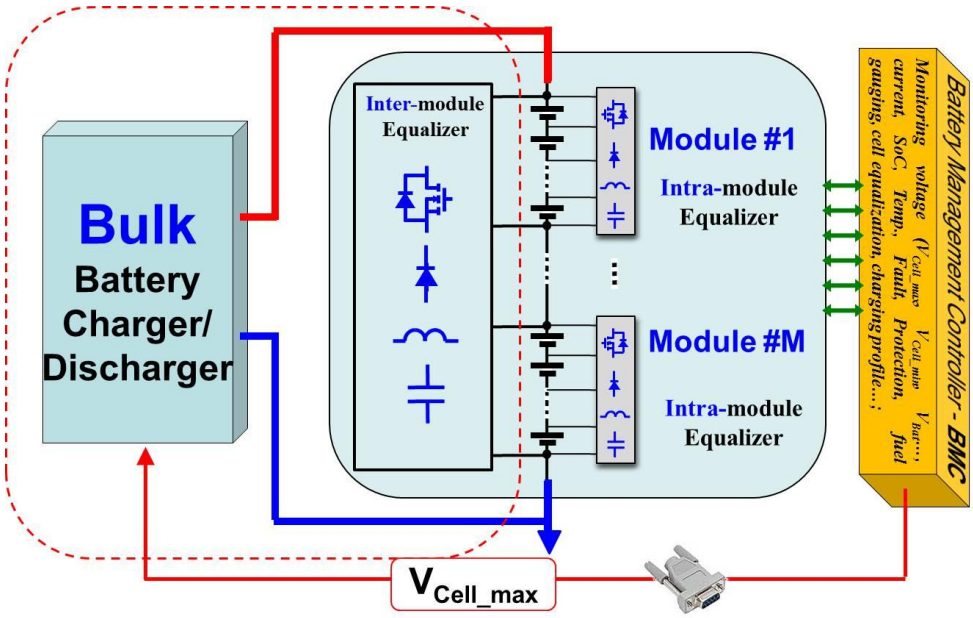

Figure 2.40 Integrated charger and modularized cell equalizer

Figure 2.41 shows the proposed system configuration of the distributed charger/equalizer system, i.e., smart battery module. Comparing the system shown in Figure 2.40, the bulk charger/discharger is split into every module, i.e., distributed charger/discharger. All of these distributed converters are parallel-connected with a high voltage DC or AC link voltage, depending on the charger's topology, such as the DC charging station from Eaton [79], ABB [80][81]. When there is unbalancing with modules, the distributed charger can be controlled to charge the low SoC module more and perform as an inter-module equalizer. The intro-module equalizer, shown in Figure 2.40, will always try to balance the cells in each module. When the charger is disconnected with the DC-Link voltage, the diode will conduct and provide energy from the battery pack for the corresponding charger to charge the low SoC modules (assuming a DC link is provided for the distributed charger/equalizer). The distributed charger/discharger and the intro-module equalizer are combined to perform as a smart battery module and each smart battery module can be standardized, modular and scalable. There will be no need to design

different power level of charger/discharger to fit different battery capacity. By using parallel and series connection, the future battery charger/discharger and equalizer can be scalable, lower cost, higher reliability. Figure 2.41 (right) shows the demonstration of the distributed charger/equalizer system with smart battery module.

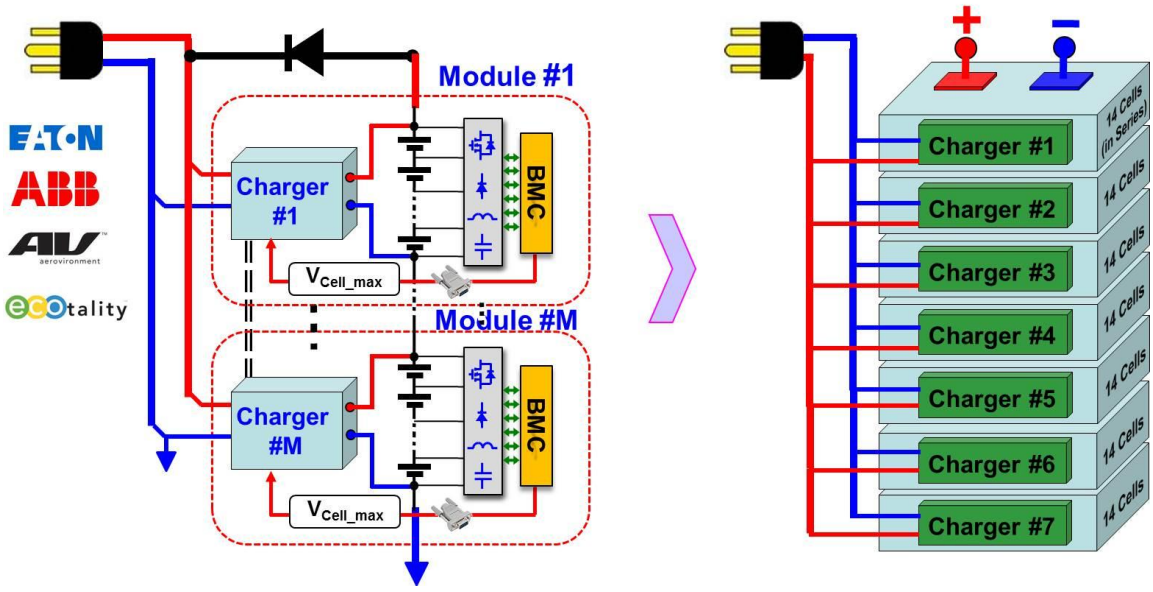

Figure 2.41 Distributed charger/equalizer system – Smart battery module

2.6 Summary

Dissipative cell equalization is studied. Non-dissipative equalization methods are reviewed and categorized using an energy flow chart. The battery management controller and system-level configurations of the lithium-ion battery are introduced. The lithium-ion battery charging profile based on V_{Cell_Max} monitoring and its design consideration is proposed, addressed and validated with experimental results in an 8.4kW bidirectional battery charger, and this method can protect lithium-ion battery from over charge/discharge. Finally, the concept of the smart battery module based on an integrated charger and equalizer is introduced.

Chapter 3 Design Considerations for DC Future Home Emulator Testbed

As shown in Figure 1.7, all the components in the DC Nano-grid can be classified into four types. The first one is the grid interface converter, which is also referred as the energy control center (ECC) in this paper. The second type is generation, which could be in the forms of solar (Photovoltaic–PV), wind, fuel cell, gas engine generator and so on, among which only PV system and its optimization are discussed in this paper. The third type is energy storage, which could be in the form of batteries, compressed air, flywheel, Pump-hydro and so on, among which only lithium-ion batteries, higher power and energy density chemical energy storage, is discussed in this paper. The fourth type is load demand.

To efficiently implement the DC Nano-grid testbed with the integration of renewables and energy storage, the first challenge will be the complexity of the different sources since it not only includes multiple sources, but also all the sources characteristics are different, such as grid interface converter, PV, wind energy and energy storage. Importantly, the issues will become more difficult when the PV system optimization considers the mismatched irradiance of different panels and the battery management system considers the unbalance of energy storage battery cells. Moreover, achieving high power density as well as a high efficiency of all converters will also be important for the adoption of the smart grid. This chapter presents the design considerations of different source converters for the purpose of system optimization and protection, and it includes the grid-connected interface converter, i.e., energy control center

(ECC), PV system configuration optimization, high efficiency bidirectional battery converter design and the smart home appliance. The simulation model (Switch mode and average model) for each interface converter will be provided for system level simulation. Finally, experiments for the corresponding concepts are validated with 10kW future home emulator testbed.

3.1 Energy Control Center (ECC) Introduction and Function Identification

The energy control center, i.e. ECC, serves as the single interface between the utility grid and the DC Nano-grid, show in Figure 3.1, which facilitates the DC system to be fully dynamically decoupled from the grid. By using bidirectional energy flow, the DC Nano-grid can either receive energy from utility grid, or send energy back to utility for electric bill financial credit. Taking advantage of the different utility electricity rates for on-peak and off-peak hours, bidirectional energy flow function makes it possible to achieve net-zero electricity cost, mentioned in 1.1.2, with minimum investment in renewables and energy storage.

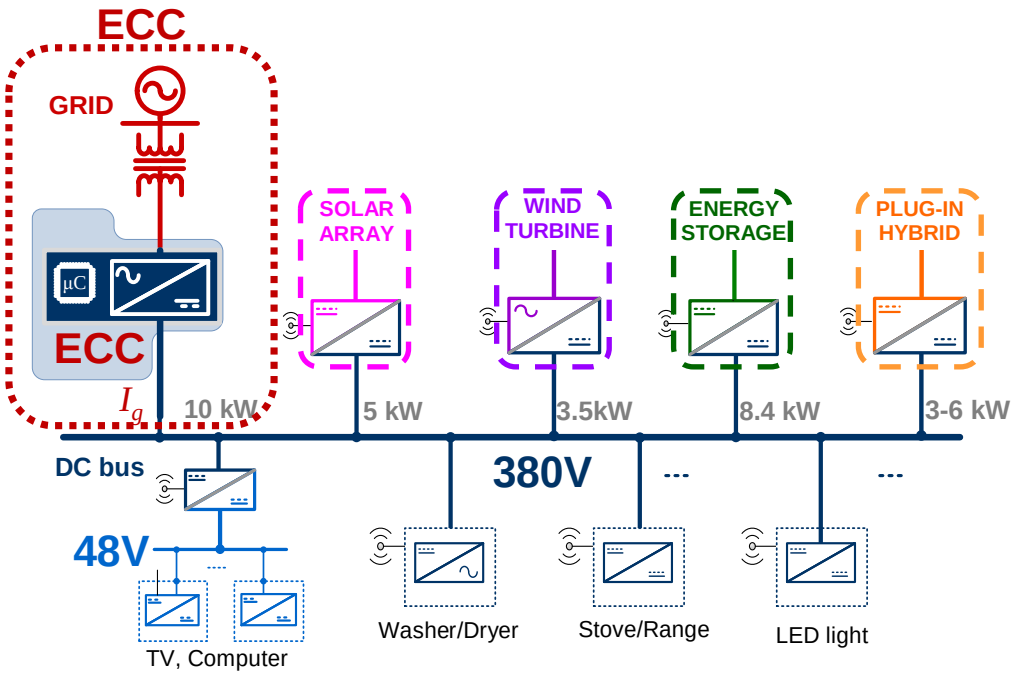

Figure 3.1 Energy Control Center (ECC) in DC Nano-grid

The utility grid mentioned in the DC Nano-grid is a split-phase 120/240Vrms single-phase system shown in Figure 3.2, which is widely used for every single family house in North America. The grounding of the system is at the mid-point of the single-phase grid.

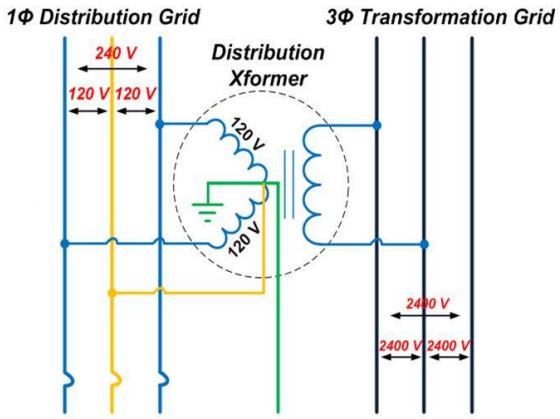

Figure 3.2 Split-phase AC grid system

A bidirectional energy flow that requires the system should not only regulate the DC bus voltage (380Vdc nominal voltage), but also have other necessary functions, including utility grid synchronization, anti-islanding detection, and power quality requirement. Figure 3.3 shows the functions list required for the ECC converter. A system level power stage will include an active power semiconductor integrated with a cooling system, the AC and DC side EMI filter.

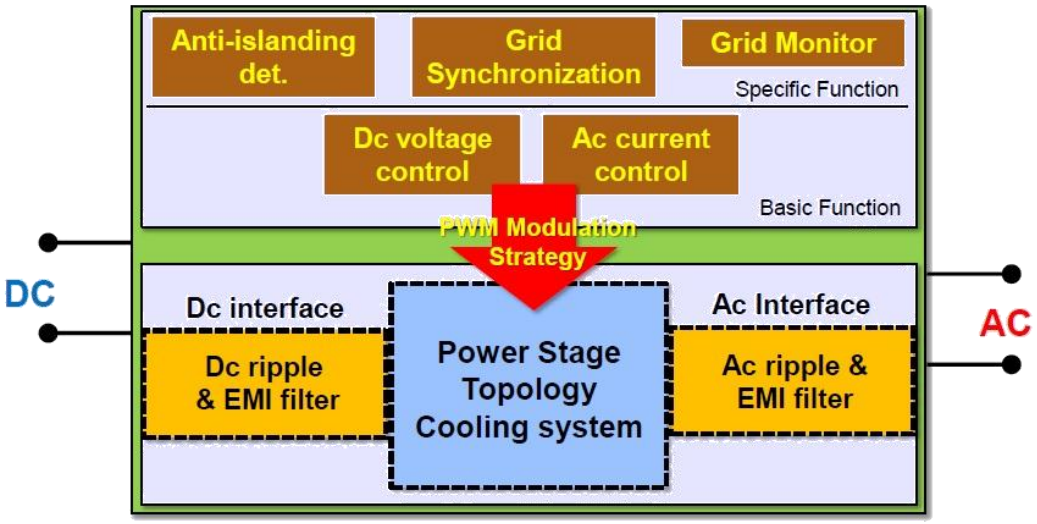

Figure 3.3 ECC system level functions list

By PWM modulation strategy, all the requirements, including seamless bidirectional power transition, DC side voltage control, AC side current control, anti-islanding detection, grid monitor synchronization, as well as grid monitoring and system energy management control, should be implemented before launching a system level experiment test.

[82][83][84] propose a two-stage, single-phase PWM AC/DC converter for ECC, shown in Figure 3.4. This topology comprises three phase-legs: two are used in the H-bridge to interface with the grid, and the third one is used as a bi-directional synchronous rectifier DC-DC converter to regulate the DC-bus voltage. PWM control is comprised of two independent parts: one is used to control the DC bus voltage V_{Bus} by operating the DC-DC converter in the synchronous rectifier buck or boost mode, depending on the power flow direction, and the other one, double-loop controller, controls the H-bridge. The outer-loop controls the DC-link average voltage V_{dc_link} while the inner-loop regulates the power from the grid. Both DC and AC side current and voltage regulation algorithms are developed, in addition to the active islanding detection and seamless transition between the rectification and regeneration mode of operation.

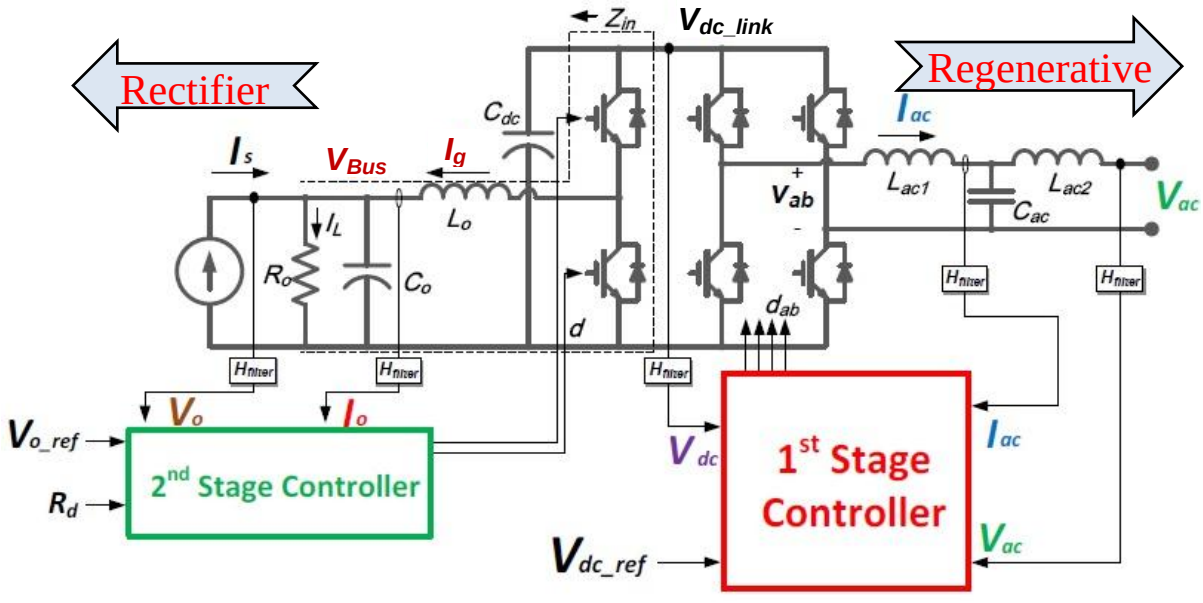

Figure 3.4 ECC topology – Two stage bidirectional AC-DC converter

The topology, by the control of the second stage, can greatly reduce the DC-link capacitor value, almost 3X reduction of size. The major contribution is the DC link capacitor reduction, which is used for absorbing twice-line frequency power ripple. Figure 3.5 (a) shows the volume breakdown comparison between conventional full bridge AC/DC converter and the proposed two-stage topology, and Figure 3.5 (b) shows the volume reduction. Therefore, film capacitors can be employed for high density, long life-time operation. Figure 3.6 shows the waveform between V_{dc_link} and V_{Bus}, where V_{Bus} is tightly controlled with voltage ripple less than 2Vpp at 5kW. What is more, the design of the ECC meets the EMI requirements on both the DC and AC side, and features DC-side high frequency leakage current elimination [83][84].

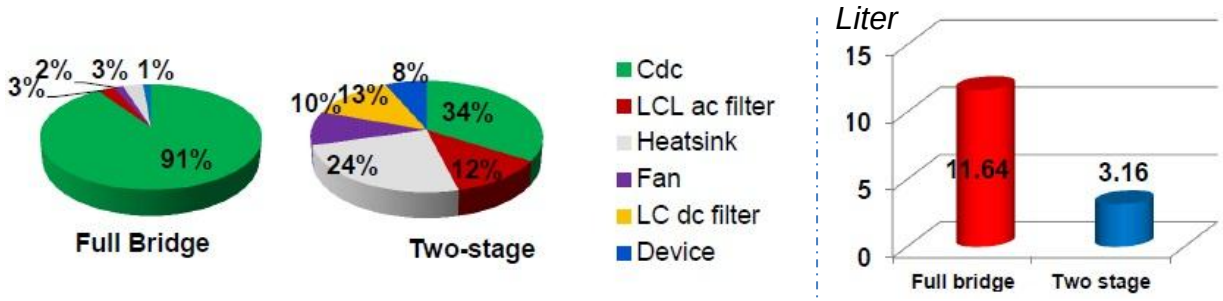

(a) (b)

Figure 3.5 DC-Link capacitor reduction

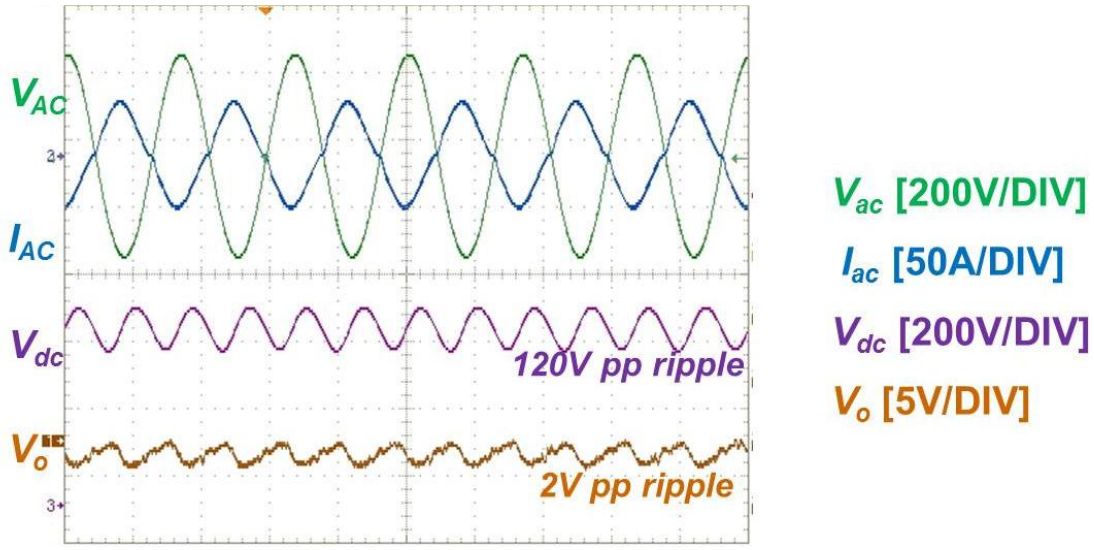

Figure 3.6 Ripple comparison between V_{dc_link} and V_{Bus} at 5kW

The converter's switching frequency is 20 kHz. Figure 3.7 shows the picture of a 10kW hardware prototype with identification of the components location.

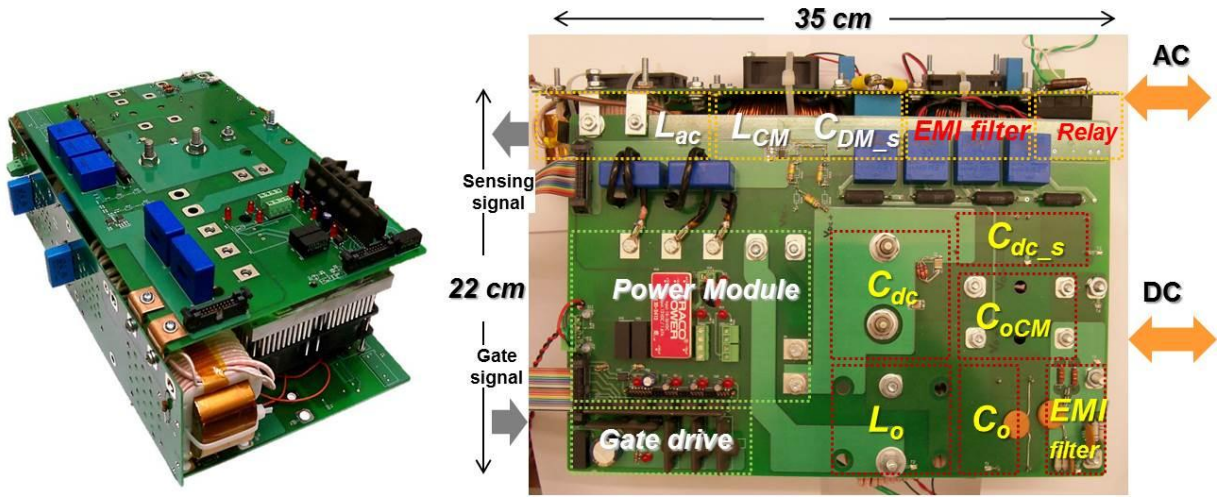

Figure 3.7 ECC hardware prototype – 10kW

For system level simulation, the ECC converter's switch model, shown in Figure 3.4, could be simplified to single DC/DC stage with only 2nd Stage controller, since only the output of the rectifier, V_{Bus}, is related with the 380V system energy management study. Considering the complimentary switching for the rectifier phase leg, the average model of the rectifier stage is shown in Figure 3.8 with the popular three-terminal model in continuous current operation.

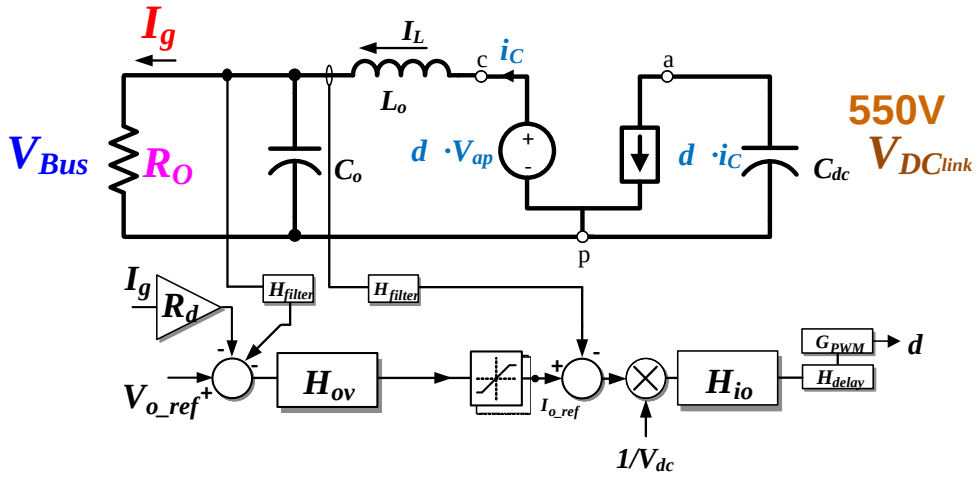

Figure 3.8 ECC average model for DC/DC stage

Figure 3.9 shows the simulation results of 1ms load transient (20Ω→200Ω→20Ω) of ECC rectifier stage switch model (red line) and average model (blue dash line), and it can be see the two models matches each other well.

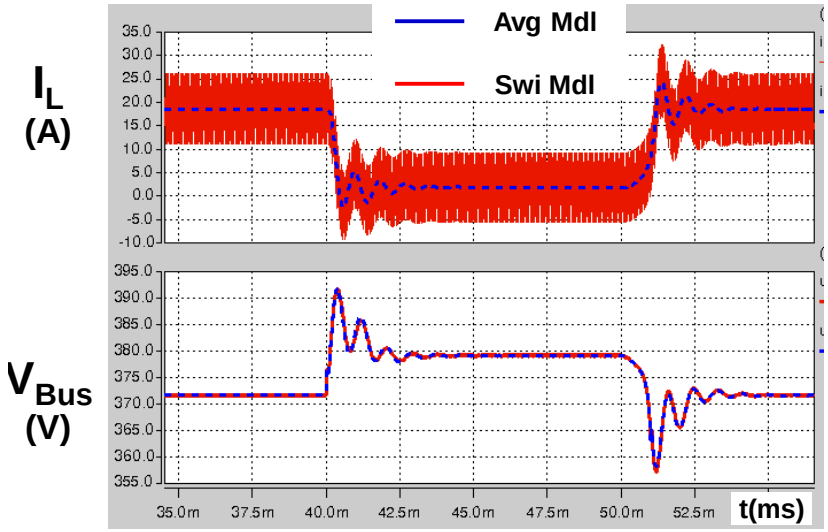

Figure 3.9 Simulation results of switch and average model

3.2 Residential PV System Configuration and Optimization

The PV system is considered as an important renewable energy source in residential applications and is widely adopted in many countries, because of the benefit of stationary installation and friendly acoustics, especially when compared with wind energy. However, the installation of the PV system in a non-ideal roof-top of a single family house will have mismatched maximum power among all the panels. Moreover, partial shading occurs frequently when part of a panel or panels are shaded by the building itself, or by posts, chimneys, trees, and other light-blocking obstacles, since partial shading causes different levels of solar irradiance on the panels. Figure 3.10 gives a real case study considering non-ideal panel orientations on rooftop and chimney-caused partial shading. The solar irradiation data is from NREL [90]. All of these non-ideal factors will leads to loss of available facilitated maximum power. [85][86][87]

have addressed the issue on to maximize the available power considering mismatches with the utilization of a panel level smart converter (SC) and an optimized PV panel configuration.

Figure 3.10 Case study of a severe mismatch for a residential PV system

To maximize the power for the series/parallel connected PV panel system, a PV panel optimizer or smart converter (SC) is connected to each panel to expand the MPPT region and reduce the mismatch impact under multi-panel series/parallel configuration. Figure 3.11 shows the I-V characteristic of the smart converter, and its MPPT functions which extend the original single MPPT point (Red solid dot) to a solid red line as shown in the figure, therefore, the smart converter facilitates the string configuration to have a possible common MPPT region even in mismatched conditions.

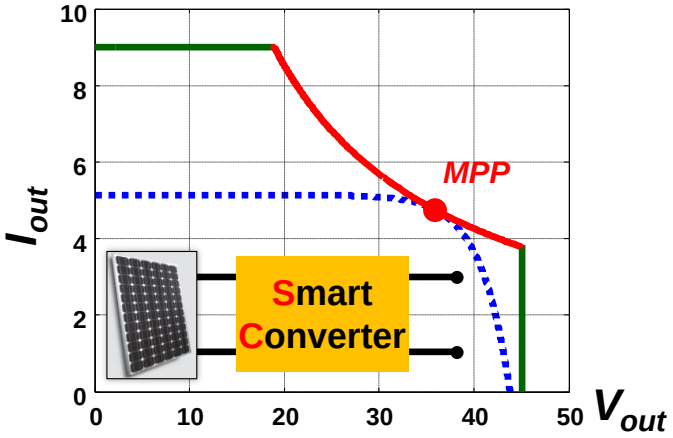

Figure 3.11 Smart converter for PV panel

Figure 3.12 (a) shows the PV system configuration with the utilization of a smart converter considering the mismatching solar irradiance illustrated in Figure 3.10. Figure 3.12 (b) shows the power difference comparing the original structure without the smart converter which has three strings in parallel with each string in series connected. There is a power gain 23% with the utility of smart converter. What is more, the single point MPPT in the original PV array is increased and extended to a region from 170V to 280V, which makes it easily to track the maximum power. To interface with the DC bus, an additional central converter is required to be the interface between PV arrays with the DC bus (360~400V) and also achieve the MPPT operation.

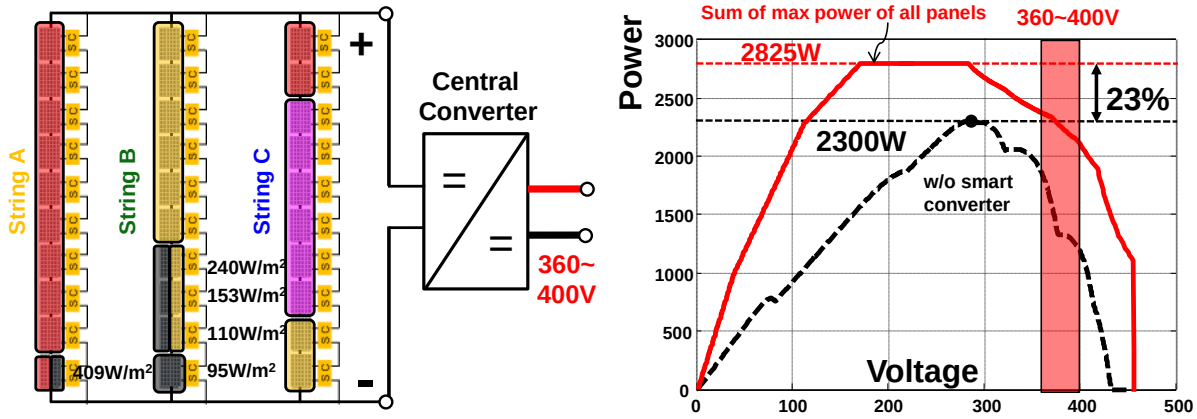

(a) (b)

Figure 3.12 Mismatch considering non-ideal orientation and partial shading

As the mismatches among panels are even severer, show in Figure 3.13, the smart converter can expand and increase the maximum power to 2220W. However, it shows that the severe mismatch in string C can narrow the common MPPT region and shift the MPPT region of string C to the left. And it is clear that the parallel of the three strings has no overlapping MPPT region. Therefore, there is a power gap between 2220W and the available maximum power, 2550W. To further improve the condition, [86] investigated another structure with paralleling

three smart converters first, and then cascaded all the 10 sub-groups together, show in Figure 3.14. Due to panel-parallel increases the common current region of each sub-group, or considering the current limit of each sub-group is increase to 3 times, a common MPPT region is found around 250V. Therefore, the maximum available power, 2550W, is delivered.

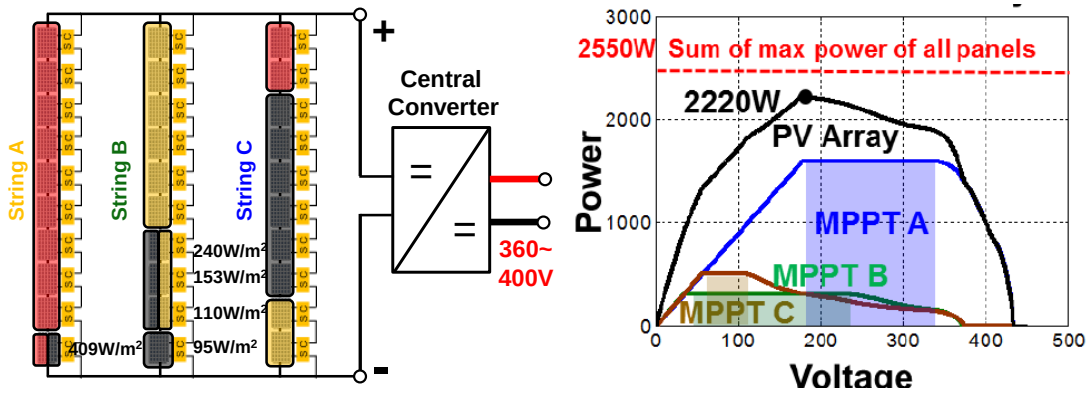

Figure 3.13 Severe mismatch study

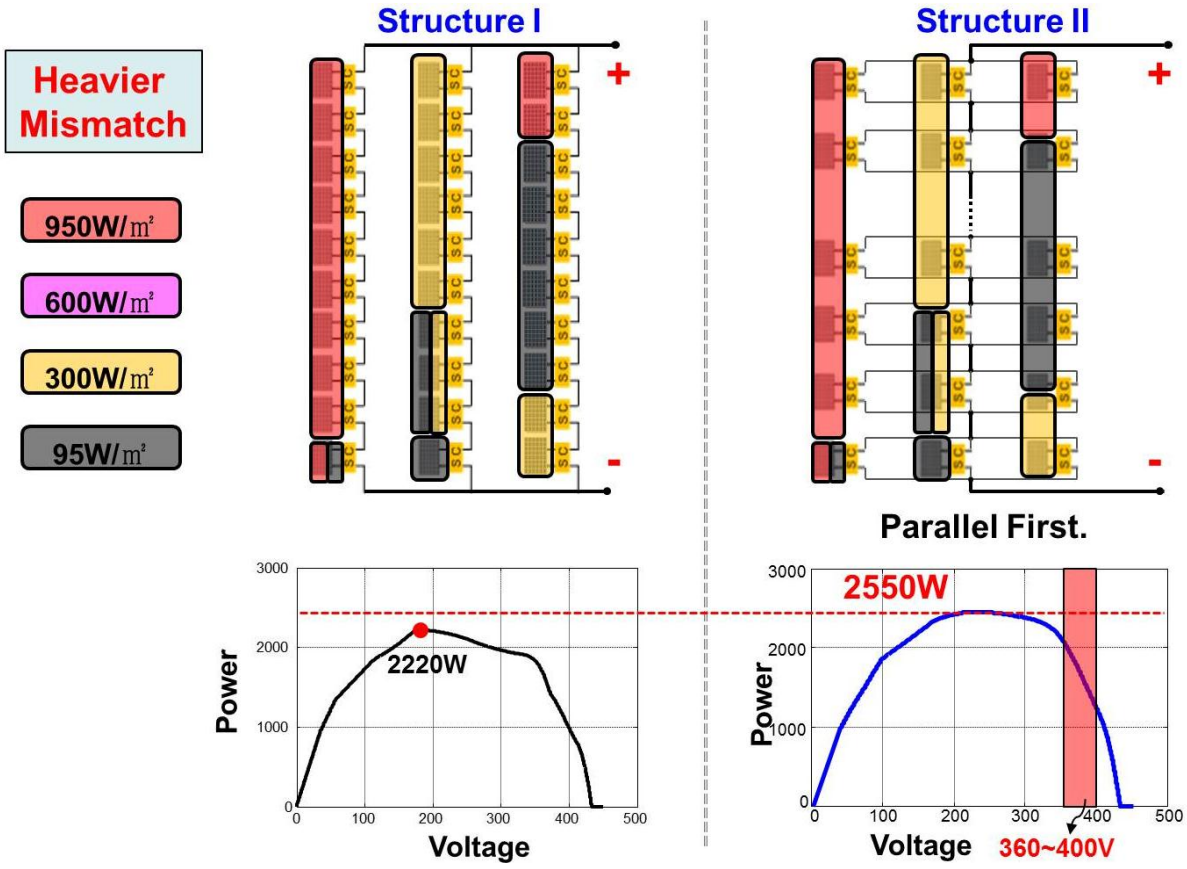

Figure 3.14 Alternate PV System Architecture

To deliver the maximum power of 2550W, an 3-channel interleaved boost converter (central MPPT converter) is needed to interface the PV MPPT region, ≈250V shown in Figure 3.14, to the DC bus, 360~400V. Figure 3.15 shows the system architecture of the PV system for REN test bed integration. For experimental convenience, 15 of E4361A Agilent solar simulators are used to emulate the 30 real panels, shown in Figure 3.15, which can be easily configured for all possible configurations. Considering mismatches of solar irradiance among the panels, a dedicated DC-DC converter with an extra distributed MPPT (Max Power Point Tracking) algorithm, what is called a module integrated MPPT converter (PV panel optimizer) or smart converter (SC) is connected to each panel to reduce the mismatch impact.

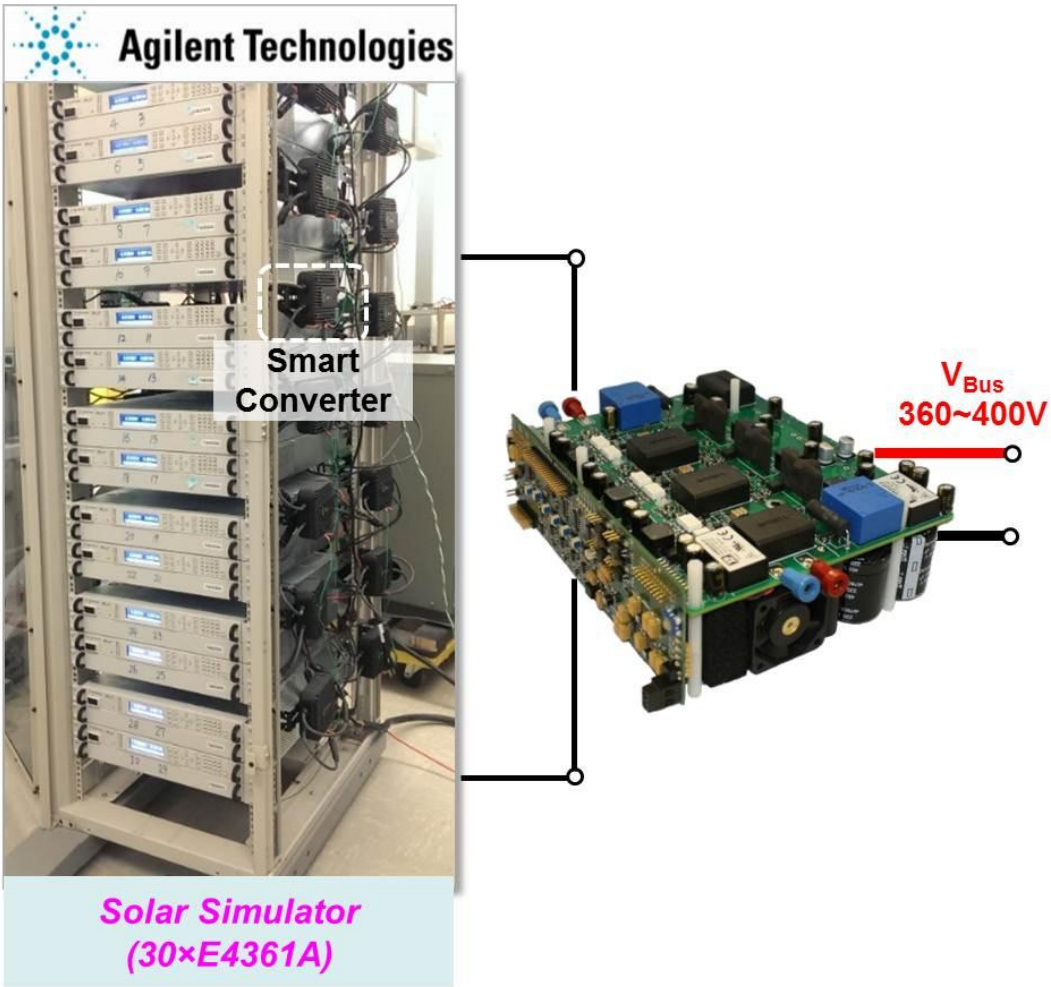

Figure 3.15 Agilent PV Simulator Rack with Central MPPT Interface Converter

Figure 3.16 shows the experiment test setup for PV system validation. A DC circuit breaker and fuses are connected to PV source for redundant protection. Then, a phase leg with active protection switch is applied to actively disconnect the PV source when DC bus is beyond the operating range. 3-channel boost converter power stage is designed for MPPT operation. E-load with constant voltage mode (CV) is set to simulate the 380V DC bus. Figure 3.17 shows the experiment validation with V_{Bus} to be 380V. After soft-start, V_{PV} and I_{PV} keep tracking in the maximum power point with V_{PV} around 320V at 5kW. Design methodology and simulation models of PV converter, which are very similar to battery converter, will be addressed in 3.3.

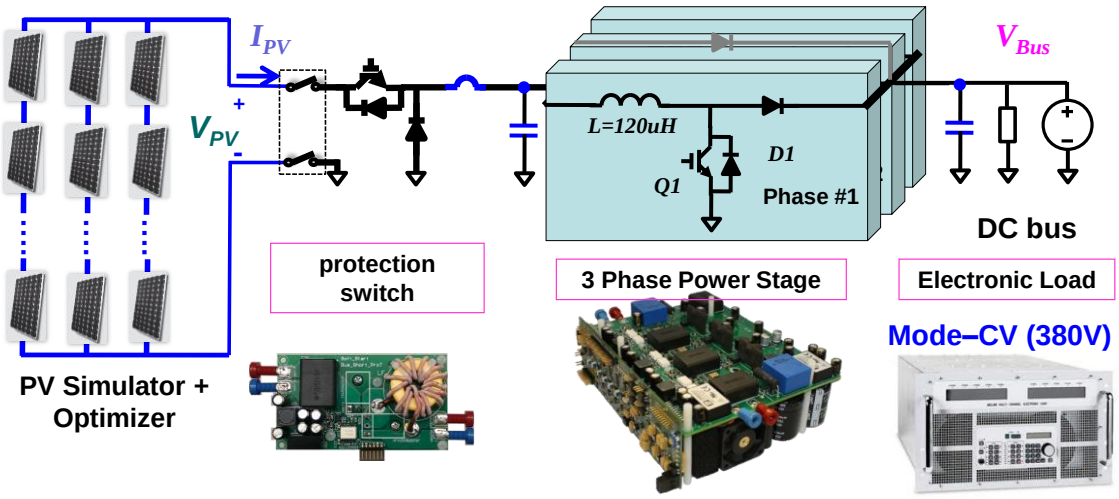

Figure 3.16 Experiment setup for central MPPT converter

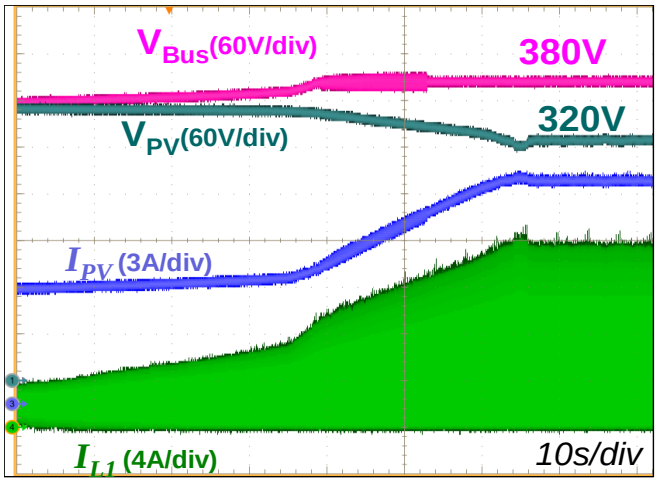

Figure 3.17 Validation for the central MPPT converter

3.3 Three-channel Interleaved Bidirectional Battery Charger

3.3.1 Si-IGBT Power Semiconductor Selection

As discussed in 2.1.1, battery pack voltage range is 252~336V, and the maximum charging/discharging current is ±25A; therefore, the maximum power of the battery converter is 8.4kW. To interface with the DC Bus, 360~400V, a three channel interleaved bidirectional buck/boost converter, shown in Figure 3.18, is selected as the target topology. And it features smaller input/output current ripple and the corresponding filter design, phase shedding to increase light load efficiency, better thermal dissipation, smaller channel inductance and so on.

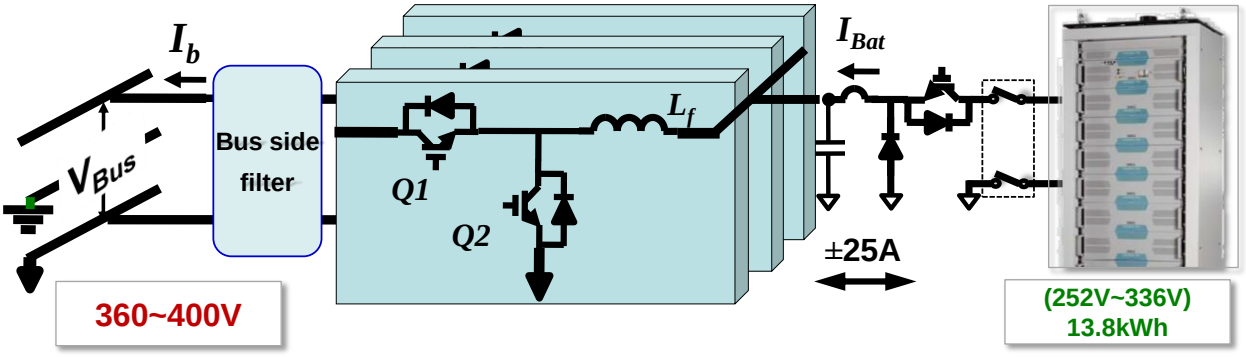

Figure 3.18 Three-channel interleaved 8.4kW bidirectional battery charger

Battery picture is from http://www.saftbatteries.cn/sites/default/files/ess_market-brochure_en.pdf, Used under fair use, 2015

The power semiconductor devices used for phase leg design of each channel is IGBT. Si-MOSFET is not used here and the major consideration is the bad performance of the body-diode of Si-MOSFET. With two active MOSFETs in each leg and the embedded body-diodes, there will be huge reverse recovery loss and severe *di/dt* during hard turn-on transition, and the fast *di/dt* will also cause heavy gate driver loop oscillations through the parasitic common source inductances. Si-IGBT with co-packaged optimal high voltage diode, i.e., soft-recovery or fast-recovery diode will dramatically decrease the reverse recovery introduced loss comparing the body-diode of Si-MOSFET. Another important difference between Si-MOSFET and Si-IGBT is

the C_{OSS}. Large current rating MOSFETs have large p-n channel overlapped area, thus, the C_{OSS} is very large. For example, the C_{OSS} and Q_{RR} of 650V/15A MOSFET, *IPx60R125C6*, is 125pF@100V and 10uC@0.1kA/us respectively, however, the C_{OSS} and Q_{RR} of 650V/15A IGBT, *IKP15N65H5*, is 13pF@100V and 0.2uC@1kA/us. There are over 10 times improvements over C_{OSS} and Q_{RR} which dominates the turn-on loss.

To select the best IGBT with smaller switching loss and conduction loss, three manufactures are compared on 650V/15A device, which are *FGP15N60UNDF* from Fairchild Semiconductor, *IKP15N65H5* from Infineon and *STGx15H60DF* from ST. Considering switching loss, the E_{Off} and E_{On} are summed up for each device and the V_{CE} is used to designate the performance of conduction loss. Figure 3.19 shows the three candidates comparison, and it shows that the *IKP15N65H5* from Infineon offers the best overall performance. Therefore, it was chosen for the power semiconductor device used in phase leg design.

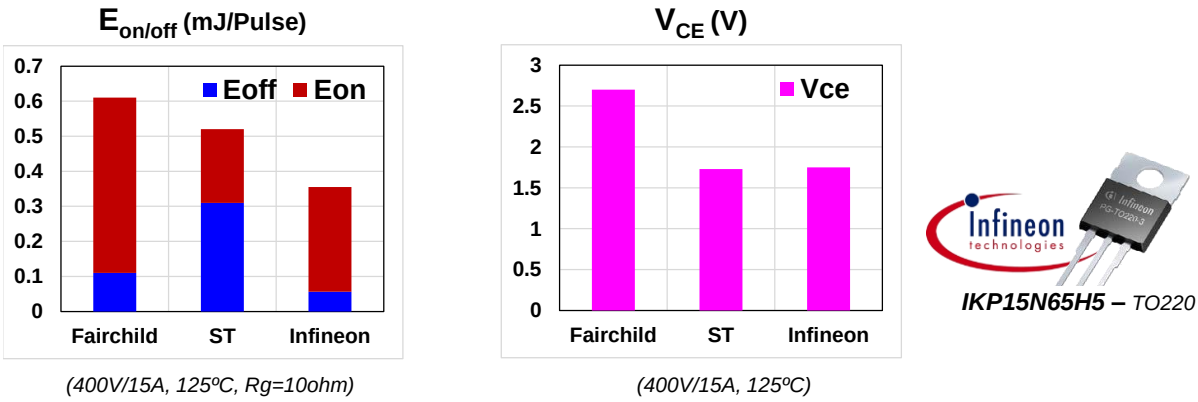

Figure 3.19 Power semiconductor device selection considerations

3.3.2 Device Loss Characterization and CCM/DCM Loss Analysis

To optimize the converter design, detailed loss characterization is implemented to understand the switching performances of the target IGBT device, *IKP15N65H5*. Two devices under test (DUT) are applied to a double pulse tester, with current shunt in series with the bottom

DUT. Bandwidth of the current shunt is 2GHz, from T&M Research. The hardware is shown in Figure 3.20 (a). Figure 3.20 (b) shows the electrical circuit diagram to test the switching current and voltage of the DUT. Different with the typical double pulse tester with SiC diode in parallel with the inductor, two same active DUT devices are used during the test to emulate the real circuit configuration for the bidirectional buck/boost converter.

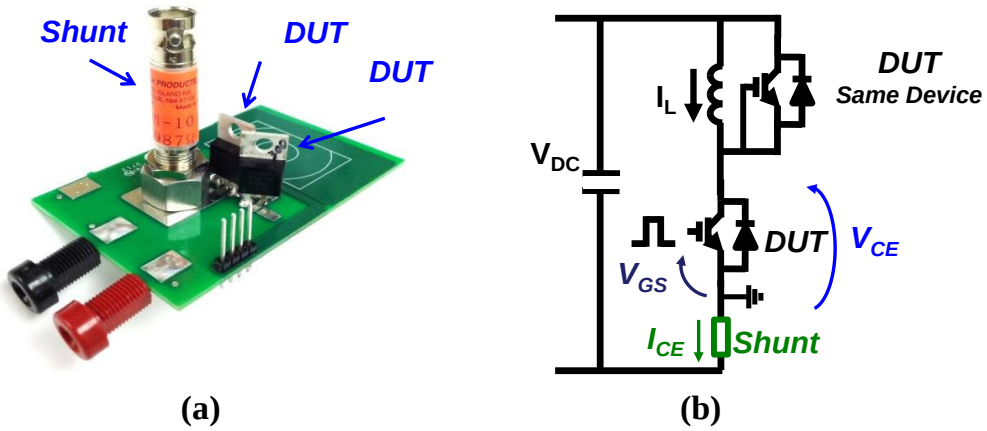

Figure 3.20 Double-pulse tester for DUT current measurement

Figure 3.21 shows the target device switching waveform during turn-on transition, shown in Figure 3.21 (a), and turn-off transition, shown in Figure 3.21 (b), with 400V/10A condition, and the external gate resistance is 10Ω for this test. As shown in Figure 3.21 (a), there is reverse recovery induced high turn-on current at turn-on moment which will generate turn-on loss on the power device which generates high turn-on loss, E_{ON}. Considering the turn-off transition, interestingly, the target device with Infineon's latest TrenchSTOP 5^{TM} technology has negligible turn-off tail current at turn-off transition, shown in Figure 3.21 (b). Integrating the current and voltage for this turn-on and turn-off transition leads E_{On}=192uJ and E_{Off}=30uJ. There are 6 times difference comparing the turn-on loss and turn-off loss. And the major reason is the reverse recovery introduced turn-on loss even with optimized fast/soft co-package anti-parallel diode.

And this loss difference has strong influences over the converter design for efficiency optimization.

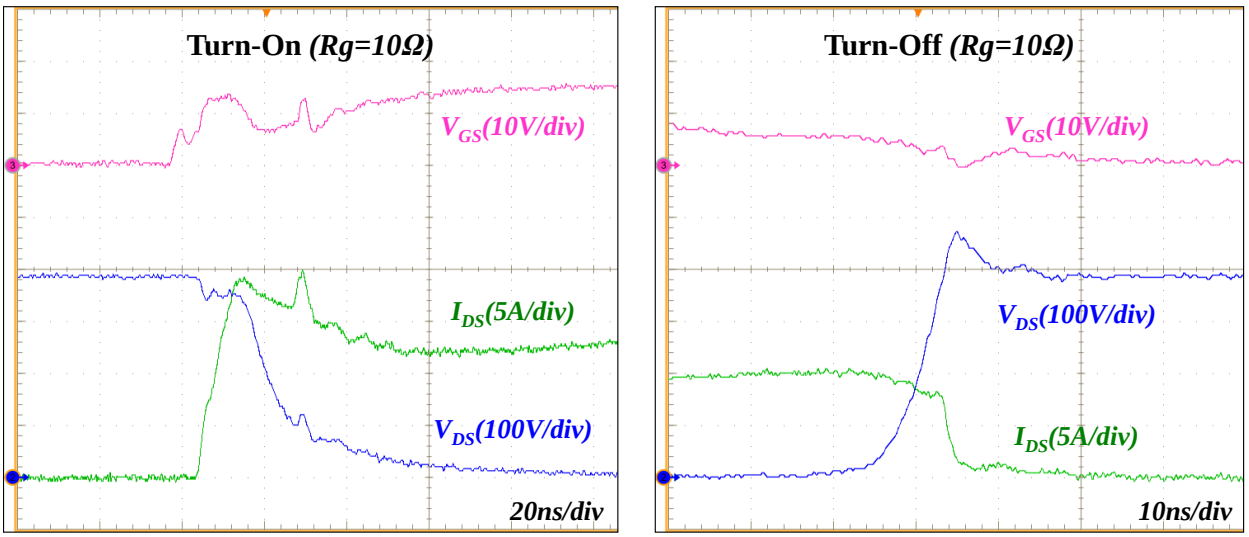

Figure 3.21 Turn-on and Turn-off switching waveform from double pulse tester

Sweeping the measurement over the target current range from 0A~20A, the E_{On} and E_{Off} switching energy is summarized in Figure 3.22. Importantly, all the turn-on and turn-off energy have already considered the energy stored in the C_{OSS} (1.65uJ). Final E_{On} value is the sum of measurement results of E_{On} and the E_{COSS}, and final E_{Off} value is the subtraction of E_{COSS} from the measurement results of E_{Off}.

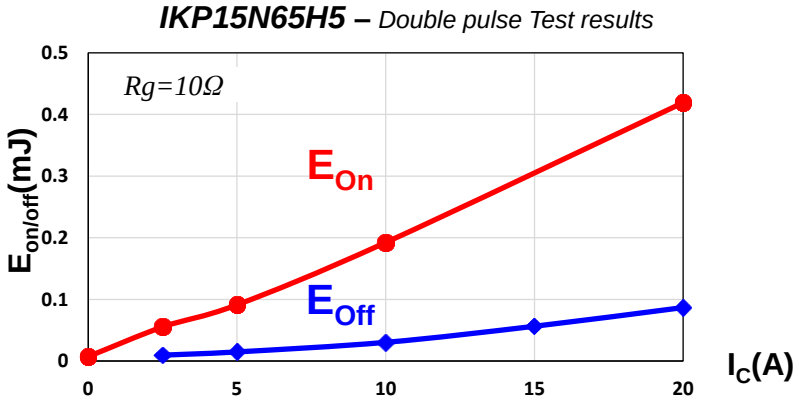

Figure 3.22 E_{On} and E_{Off} test results for IKP15N65H5

Considering the large difference between turn-on and turn-off loss, battery converter could be designed to have smaller turn-on current and large turn-off current, i.e. large current ripple in each channel. However, the total input and output current ripple will not be a severe concern, since the interleaving current ripple cancellation will help the input/output filter design. Sweeping the inductance and current ripple, it could be found that the boundary conduction mode with zero turn on current has the minimum switching loss. Figure 3.23 shows the total semiconductor loss comparison between CCM, L_f=554uH and DCM, L_f=83uH. CCM design is based on 30% of full load current ripple, and 83uH is selected corresponding to boundary mode conduction at full load and maximum battery voltage. It could be seen from Figure 3.23 that the significant turn-on loss could be saved with DCM operation, with a little bit sacrifice on the turn-off loss and conduction loss. Importantly, the conduction loss on IGBT is majorly dominated by the average load current. Large current ripple with higher RMS current value will not impact the total conduction loss very much, which is proved and shown in Figure 3.23.

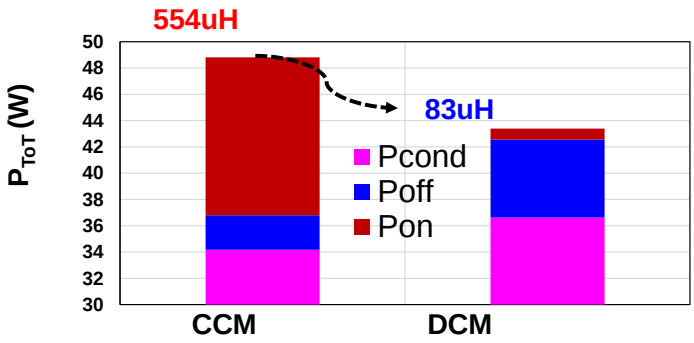

Figure 3.23 Total semiconductor loss comparison between CCM and DCM operation

3.3.3 8.4kW Bidirectional Battery Charger Prototype and Efficiency

Figure 3.24 shows the final completed 8.4kW battery charger prototype with indication of the major components, such as power device, bypassing cap, heat-sink, output choke and

sensors. Calculating the dimension, the power density for this 8.4kW converter is 75W/in^3. The switching frequency is designed to be 30 kHz.

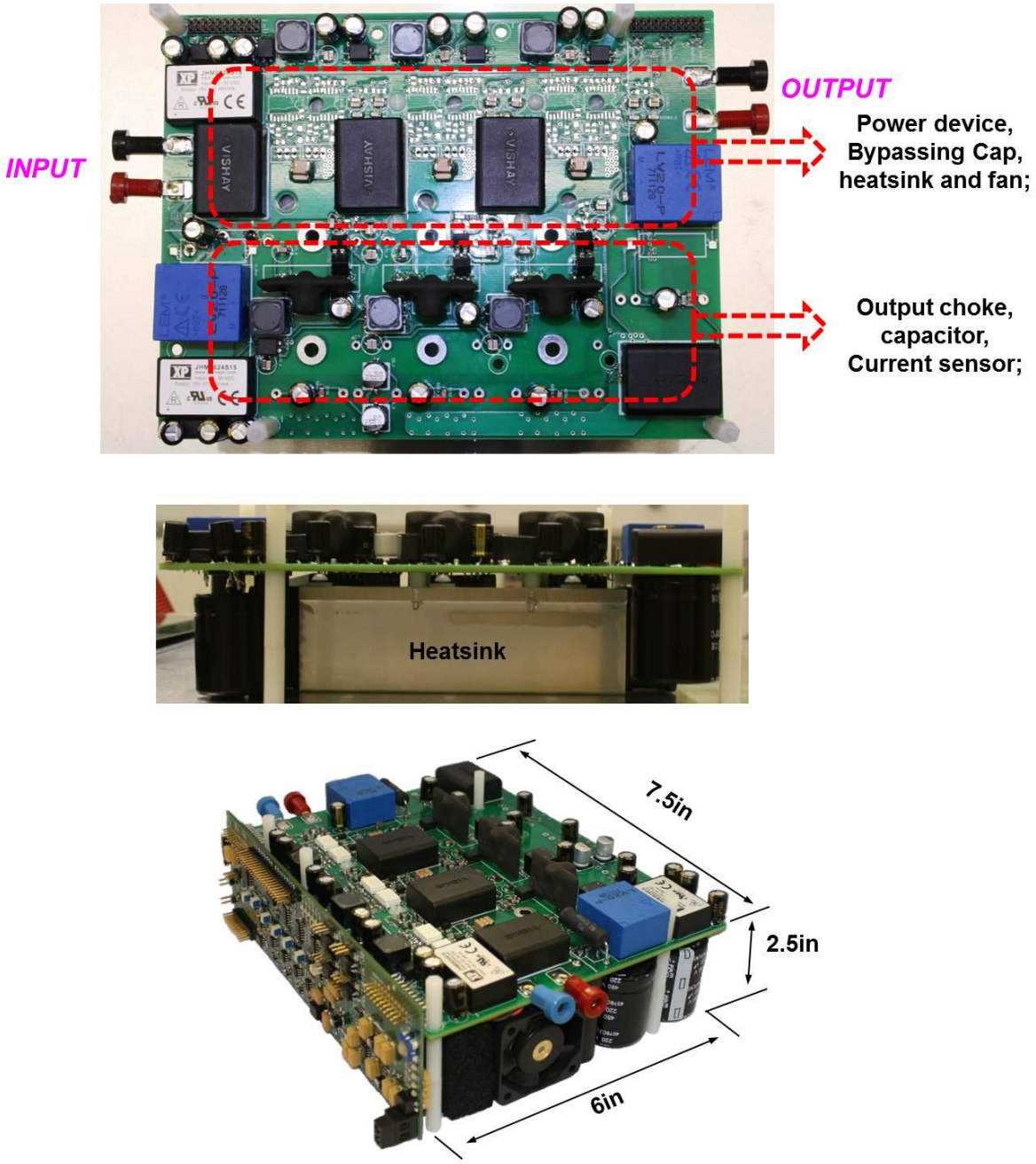

Figure 3.24 Hardware prototype for the 8.4kW bidirectional battery charger

Figure 3.25 shows the efficiency measurement of single channel bidirectional battery charger under different battery voltage conditions, maximum battery voltage, $V_{Bat.Max}$ (336V),

nominal battery voltage $V_{Bat.N}$ (310V), and minimum battery voltage $V_{Bat.Min}$ (252V). As can be seen in Figure 3.25, the efficiency over wide load range and voltage range is around 99%. Importantly, efficiency of DCM operation at light load also is also good since there is not circulation current induced conduction loss comparing CCM operation. Therefore, DCM operation does improve efficiency over wide load and voltage range for battery charger applications. Figure 3.26 shows the operating waveforms at full load with different battery voltage. At maximum battery voltage, the converter is operating in boundary conduction mode, and turns to DCM operation at minimum battery voltage, with certain dead time on inductor current at fixed 30 kHz switching frequency.

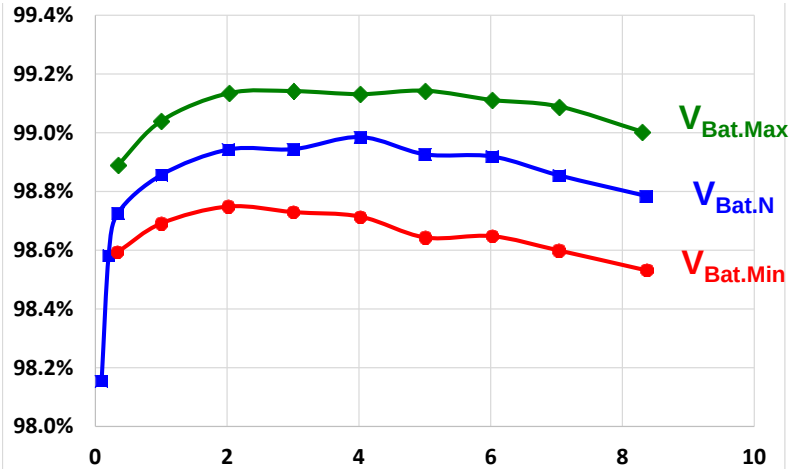

Figure 3.25 Single Channel efficiency measurement for the bidirectional battery charger (Charging mode)

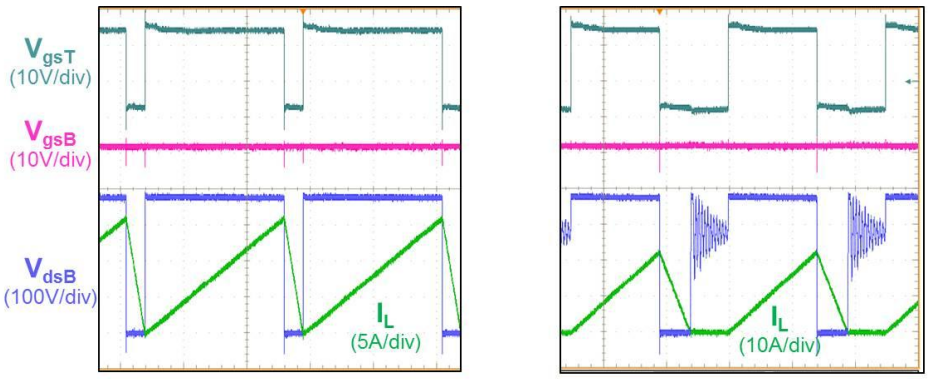

(a) V_{Bat}=336V, I_{Bat}=8.33A (b) V_{Bat}=252V, I_{Bat}=8.33A

Figure 3.26 Operation waveforms at full load under different battery voltages

3.3.4 Simulation Model for battery bidirectional converter

DCM operation for battery converter has two different models: one is for charging operation controlling the top switch in Figure 3.18 which can be referred to be Buck converter in DCM operation; the other one is for discharging operation controlling the bottom switch which can be referred to be Boost converter in DCM operation.

Figure 3.27 shows the three-terminal average model for battery converter including V_{Cell_Max} control loop under charging mode, and μ in is found in (3.1)

$$\boldsymbol{u = \frac{d^2}{2 \cdot L_f \cdot f_S} \cdot \frac{v_{cp}}{i_a}} \tag{3.1}$$

where *d* refers to the duty cycle for top switch of Buck converter in DCM operation. Figure 3.28 shows the transient simulation results (1A→24A→1A, 1ms) for both average model (blue dash line) and switch model (solid red line), and the two simulation results match each other well.

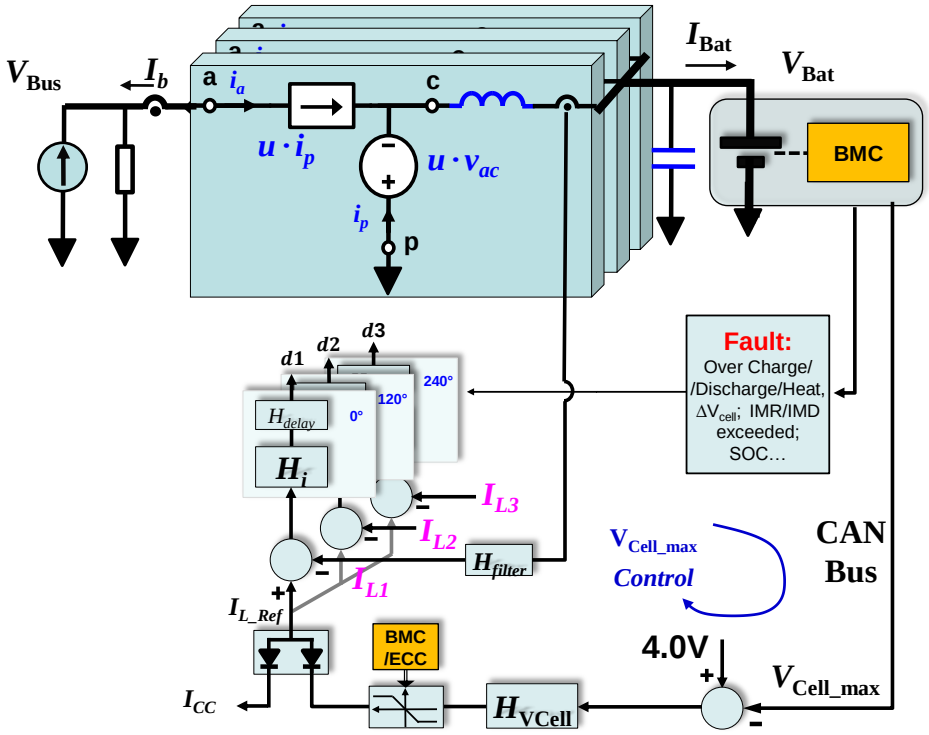

Figure 3.27 Average model for battery converter in charge DCM operation

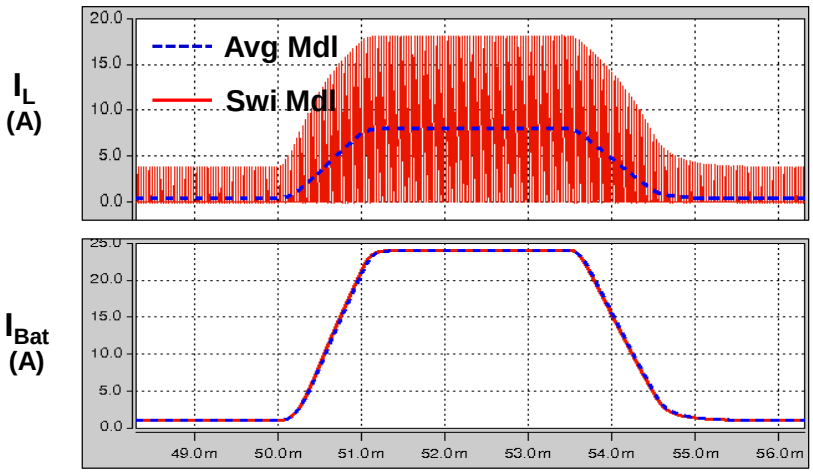

Figure 3.28 Simulation results of average and switch model for charge operation

Figure 3.29 shows the three-terminal average model for battery converter in discharge bus voltage regulation, and μ in is found in (3.1), where d refers to the duty cycle for bottom switch as Boost converter in DCM operation. Figure 3.29 also includes the discharge bus voltage regulation with droop operation, see R_D in Figure 3.29. Detailed discussion on droop resistance setting is addressed in Chapter 4.

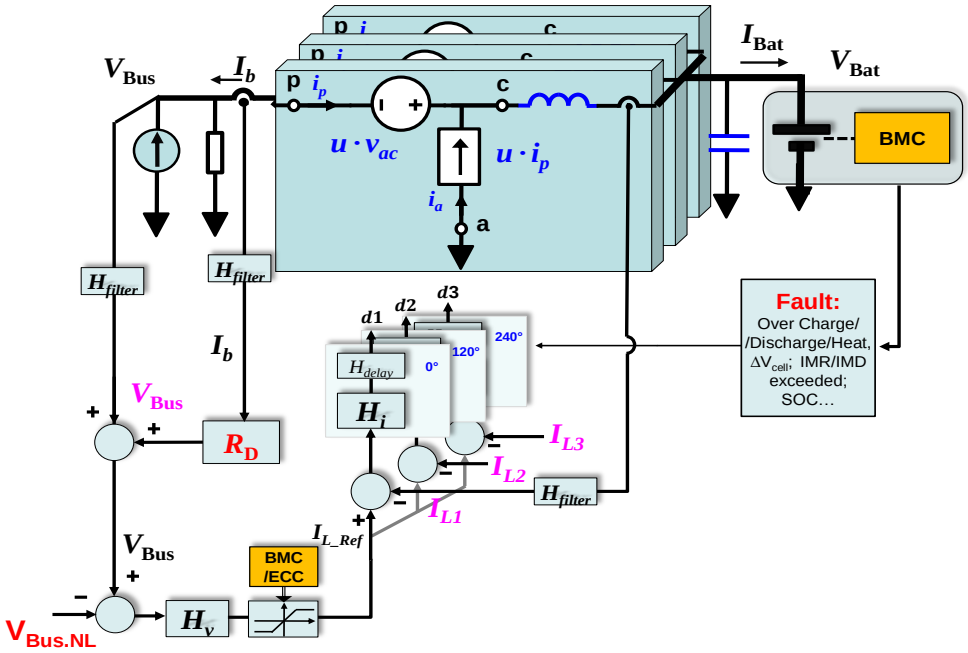

Figure 3.29 Average model for battery converter in discharge DCM operation

Figure 3.30 shows the load transient simulation results (18Ω→180Ω→18Ω, 1ms) for both average model (blue dash line) and switch model (solid red line), and the two simulation results match each other very well.

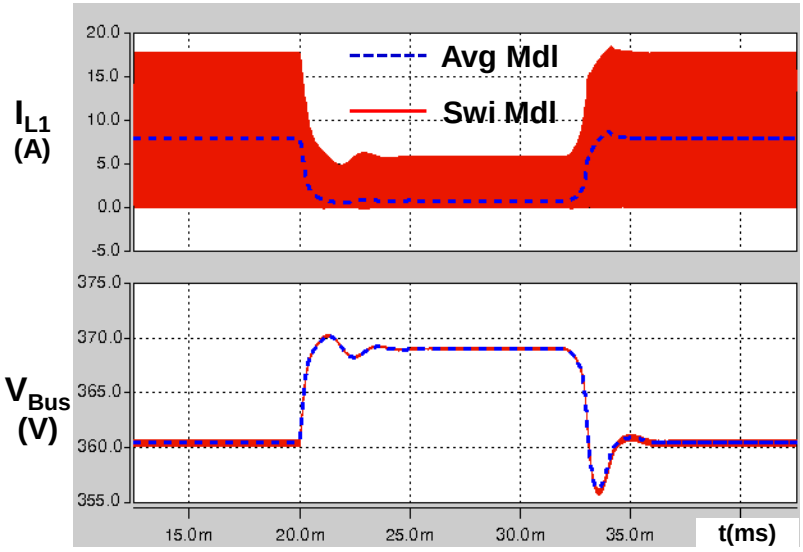

Figure 3.30 Simulation results of average and switch model for discharge bus operation

3.4 Summary

The ECC converter is reviewed with identification of the system function. PV configurations with consideration of mismatches are reviewed with the utilization of smart DC-DC converter to increase the maximum power. Different configurations are compared to further expanding the common MPPT region. An 8.4kW multi-phase bidirectional battery charger with Si IGBT in DCM operation is designed and implemented to achieve high efficiency and to be the interface converter between lithium-ion battery and DC bus.

Chapter 4 Energy Management System (EMS) Control and Experiment for DC Future Home

To enable Net-zero electric energy cost and optimal power management for future homes or buildings, the DC electric distribution systems (DC Nano-grid) finds feasibility and simplicity for integrating multi-type renewable energy sources. However, integrating all the sources and loads in a simple, reliable and smart way is still challenging. What is more, in order to optimize energy management for future home, residential load demand profiles and local renewable power variation, like fluctuation of wind speed or solar irradiance, play an important role in managing the power flow in a period of a day/season/year. Finally, managing all the energy flow among the grid, energy storage and renewables in a smart and robust way is also quite important for the adoption of renewable in a future Smart Grid.

4.1 Distributed Droop Control for DC Renewable Energy Nano-grid

Considering the centralized control and decentralized control and their characteristics discussed in section 1.3, a distributed droop control is proposed in this paper which combines the benefit of decentralized control and centralized control. Therefore, the proposed system embeds the robustness, as well as the smart prioritization of energy scheduling. As shown in Figure 4.1 (a), two sources sharing the same no-load set point voltage, apply droop control with the droop resistance, R_d, (4.1)

$$\boldsymbol{R_d = \frac{V_d^2}{P_{Max}}} \tag{4.1}$$

R_d is in reverse proportional to the maximum power of the corresponding source while keeping V_d the same. Under this condition, the two sources will share the load proportional to the source power limit. However, this control cannot support prioritizing different kinds of sources in case the desired system prefers to use source #2 first, for example, solar, to save electric energy cost. In Figure 4.1 (b), by shifting the set point of source #1 down by low speed communication: see the grey line in Figure 4.1 (b), and summing up the two sources, solid line in Figure 4.1 (b), the utilization of source #2 will have a higher priority than #1. For example, the system could apply source #2 as solar or wind energy to be used firstly within the availability of the renewable energy. In this case, the bus voltage will be regulated in a distributed way. In Figure 4.1 (b), source #2 regulates the bus in a higher voltage range with source #1 in idle mode, and source #1 regulates the bus lower voltage range with source #2 in current/Power limiting mode.

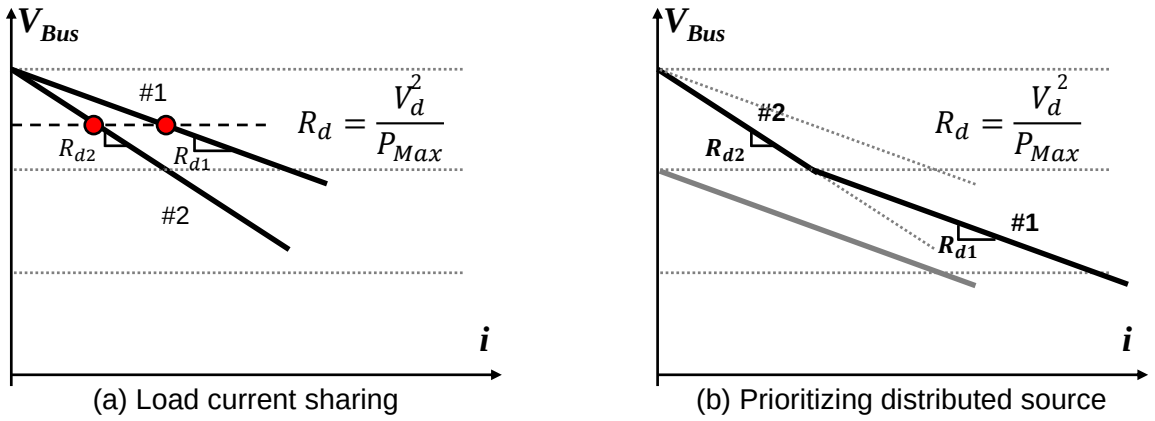

Figure 4.1 Droop design consideration with a) load current sharing; b) distributed droop control

In case there is more than one source in one voltage range, the two sources could both run in droop mode, shown in Figure 4.2 (a) with source #1 and #3 for example, sharing the load in proportion to the source power limit. Another possible candidate is to have one source, for example source #1, responsible for regulating the bus in the corresponding voltage range while all the other sources, for example source #3, are operating in low-speed current/power

scheduling mode. The purpose of this control is to avoid fast and continue transient on source #3, shown in Figure 4.2 (b), considering the non-coincidental load characteristics of the residential load application. Moreover, the example for source #3 could be energy storage, such as lithium-ion batteries, which prefer a slow speed or fewer transients to extend the lithium-ion battery cycle life.

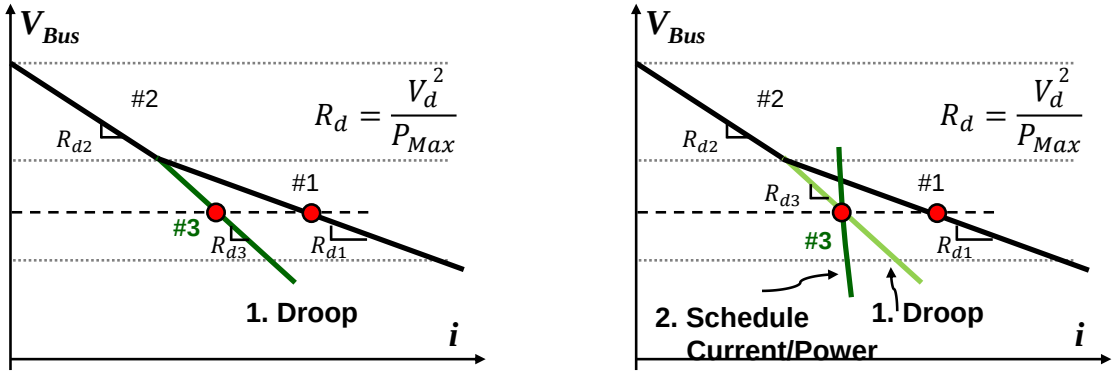

(a) Droop control for #3 (b) Schedule power for #3

Figure 4.2 Power scheduling with distributed droop control

Another benefit of distributed droop control also includes load shedding, shown in Figure 4.3. The emergency region with bus voltage signaling can be designed for shedding the unimportant load to prevent the system from failing in some critical over load conditions, such as shedding dryer and water heater in residential applications.

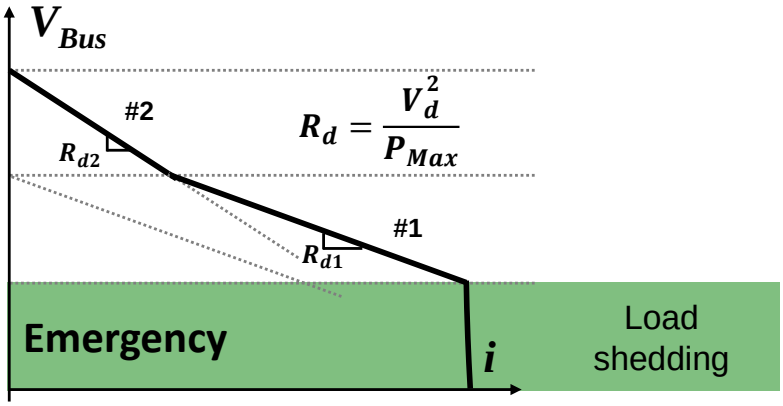

Figure 4.3 Load shedding at heavy load

Based on the discussion of energy prioritization and considering the cost of different energy types, such as renewable, utility energy, energy storage energy, the highest priority of energy utilization is designed to be renewables considering the low cost, and then to be the utility energy which embeds the bidirectional energy flow. The third one is battery emergency backup power, enhancing the system robustness and smart energy management. This priority organization, shown in Figure 4.4, is the fundamental and basic organization of the system control, which applies droop control for system robustness. Based on the DC future home Nano-grid addressed in 1.1.3, shown in Figure 4.5, an example of a system level distributed droop control for all the discussed source components is shown in Figure 4.6. PV and Wind energy is prioritized to regulate the bus over 390V; ECC regulates 370~390V with bidirectional energy flow, and the battery is responsible for DC bus below 370V by discharge regulation.

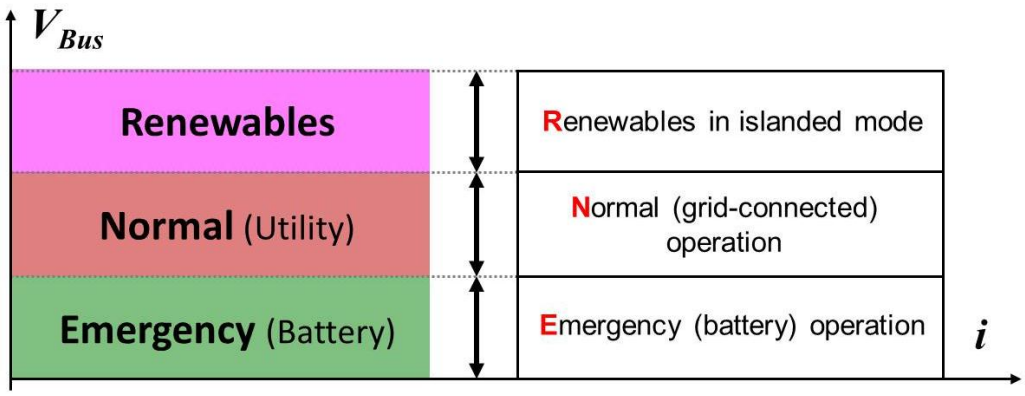

Figure 4.4 Distributed droop control with source prioritization

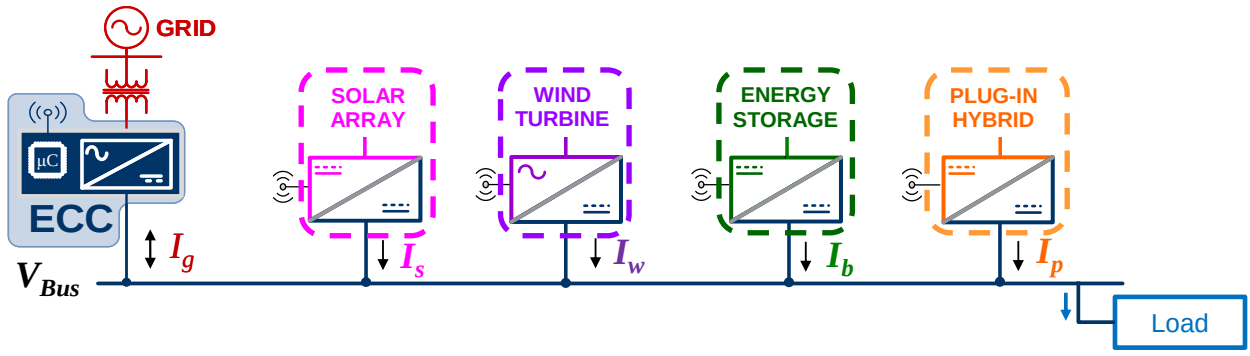

Figure 4.5 Electrical source components in renewable energy DC Nano-grid

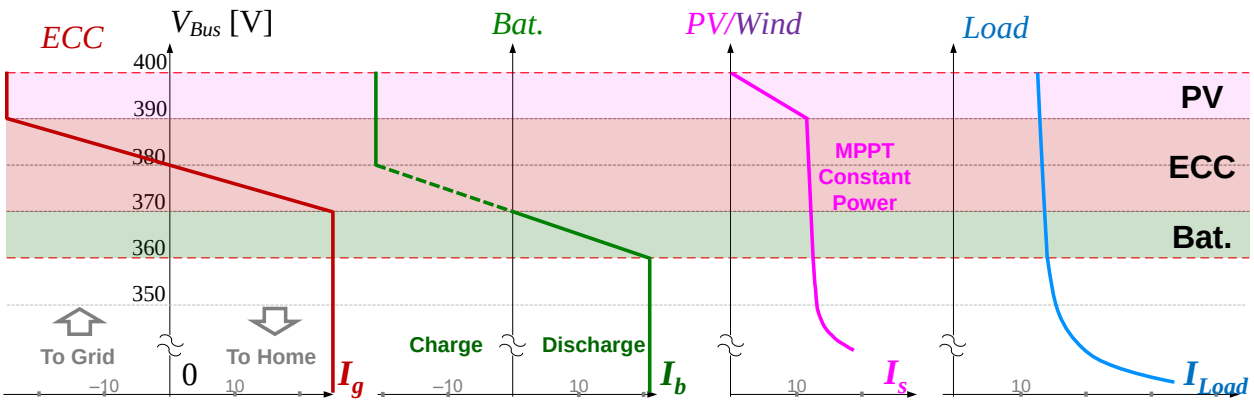

Figure 4.6 Fundamental control strategies for ECC, battery, PV/Wind and load

4.2 Energy Control Strategies for ECC, PV/Wind and Battery

4.2.1 Energy Control Strategy for ECC Converter

The solid dark red curve, shown in Figure 4.7, is the control strategy for the energy control center (ECC) converter. The ECC is responsible for DC bus voltage regulation from 370V~390V with bidirectional energy flow. The regulation droop resistance is designed to be 10V over the ECC current limit, 25A, which is 0.4Ω.

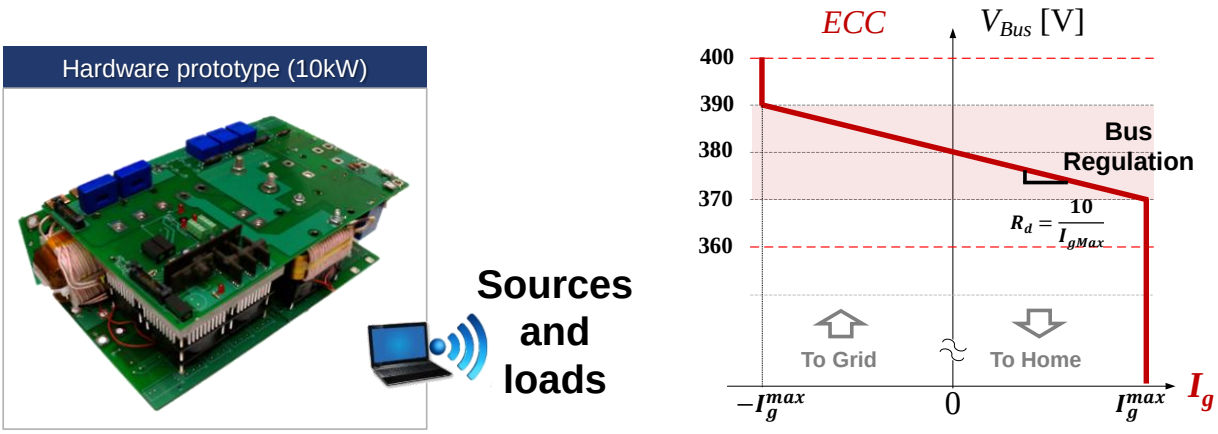

Figure 4.7 Energy control center (ECC) and its control strategy

Within 380~390V, the ECC converter current I_g is negative and it is operating in regenerative mode with energy flowing from home to utility grid. Within 370~380V, the ECC is

operating in rectifier mode with energy flowing from utility grid to home. Beyond this voltage range, the ECC converter enters a current limit mode and finally shuts down when bus voltage is greater than over voltage protection (V_{Bus}>400V) and less than under voltage protection (V_{Bus}<330V). Importantly, regulation within the target range requires the ECC converter to respond fast enough for all possible load transient. Besides the basic circuit level requirement, ECC will communicate with all other sources, PV/Wind, energy storage and load appliance, for smart energy management to achieve Net-zero electricity energy cost.

4.2.2 Energy Control Strategy for PV/Wind Converter

The objective of the PV converter's control strategy includes two parts. The first one involves sourcing maximum available power from the installed solar panel with clean and free energy, which serves the a major purpose. The other one is regulating the bus between 390V~400V during islanded mode operation when PV/Wind's power is higher than all the other sources. The voltage regulation mode of the PV/Wind converter will limit the PV/Wind side power and achieve power equivalence between load and PV/Wind. In this case, the PV converter will not be working with maximum power tracking. Importantly, droop-resistance within 390~400V is constant considering the intermittent and variable PV power.

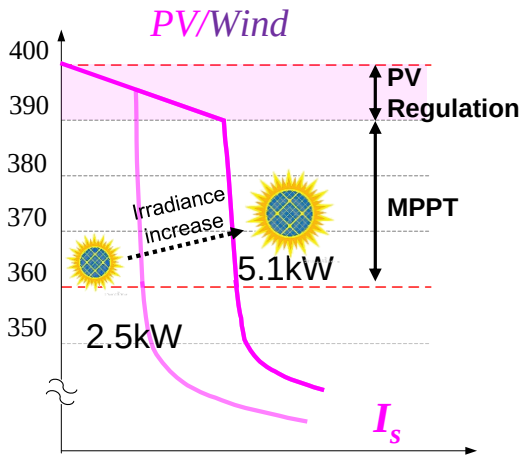

Figure 4.8 PV converter control strategy

4.2.3 Energy Control Strategy for Battery Energy Storage

A lithium-ion battery is used as an energy storage component in the proposed DC Nano-grid. Detailed information of the battery bank configuration, battery converter hardware including efficiency optimization prototype design consideration can also be found in 2.1.1 and 3.3. To manage energy storage smartly, it is critical to understand the objectives of energy storage management. The first control objective of the Li-ion battery is the charging profile. This paper adopts the maximum cell voltage, V_{Cell_Max}, controlled charging profile addressed in Figure 2.4. The second objective is emergency back power to increase system robustness. More importantly, the 3rd objective of energy management is to have flexible and smart control strategies for achieving Net-zero electric energy cost with utilization of the dispatchable battery storage energy.

Figure 4.9 shows the fundamental strategy applied to the battery energy storage system. Between 360V and 370V, the battery converter regulates the DC bus when the ECC converter enters current limiting, as in case of over load. This serves as a backup power for the DC future home. The droop resistance is designed with a 10V voltage drop over the current limit of the battery converter, 20A. When the DC Nano-grid is operating in islanded mode, which means the ECC converter has no capability to regulate the DC bus by bidirectional energy flow, the battery converter would provide a similar function to the ECC by charging/discharging the battery within the limit battery usable capacity. More importantly, the battery will lose the capability to do charge regulation when the battery is fully charged, as well as losing discharge regulation when battery is fully discharged.

In a normal operating mode when the bus voltage is over 370V, the battery control strategy follows the dashed green line, which designates that the battery will not regulate the DC

bus together with the ECC converter by charging the battery. A charge current command over 370V is decided by battery management or ECC command for smart energy dispatching. More importantly, the battery converter will not regulate DC bus over 370V, and the major concern is with the Li-ion battery cycle life. Since the bus regulation of the battery converter has the battery bank answering fast load dynamics and sharing load with the ECC converter, thus decreasing the battery calendar/cycle life. The benefits of having one source regulating the bus and other sources operating in power scheduling mode is addressed in 4.1.

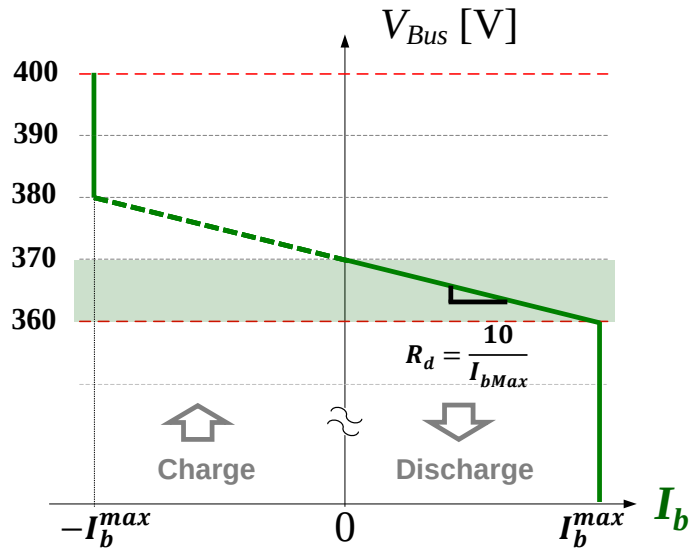

Figure 4.9 Battery bus voltage regulation, 360~370V

Figure 4.10 shows one of the interactions between the energy storage and the ECC by programming battery charging and discharging current within the allowed battery current range to schedule certain amount of power for system energy management optimization. When the battery is close to full charge and operating in a constant voltage charging mode, the battery charge current is decided by the lithium-ion charging profile of battery management system (refer to 2.4), which is a series of constant power lines from maximum charging power to minimum charging power (decided by maximum battery pack termination current and voltage).

While scheduling power for an energy storage system, the ECC converter is responsible for the bus regulation and the battery converter is following the command of the energy control center (ECC) for optimization of system energy management.

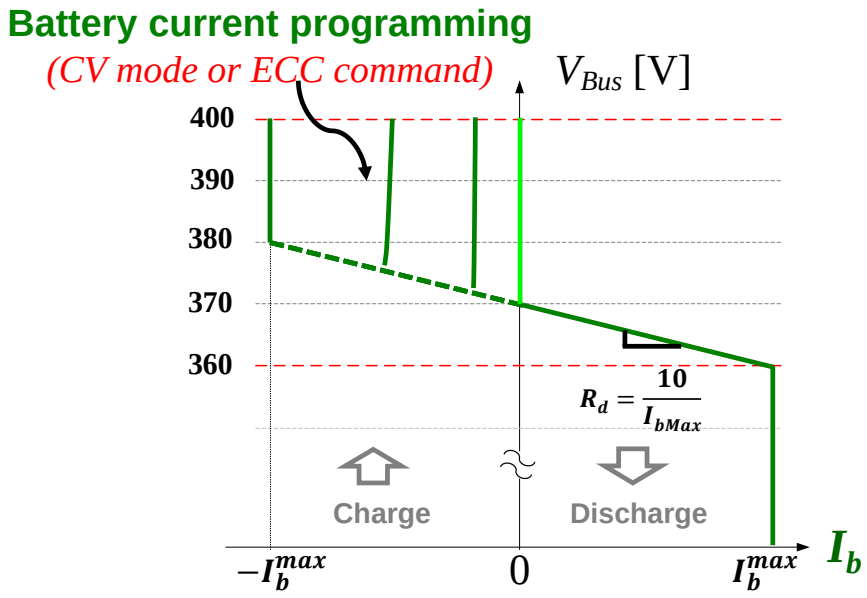

Figure 4.10 Battery energy scheduling by programming battery charge/discharge current

Figure 4.11 shows another kind of interaction with ECC by shifting the battery control role upward and downward. More discharge will be engaged when shifting the battery control law upward since the discharge region, right half of Figure 4.11, covers more of the bus voltage region (360V ~ 400V). For example, the discharge region of the upper control role in Figure 4.11 ranges from 360V to 380V, increased by 10V when compared with the lower battery control law, which is only from 360V to 370V. In contrast, shifting the battery role downward will engage more charge for energy storage. More important, the red shaded area in Figure 4.11 is the unfavorable region for discharge, since discharged battery energy in this region will be sent back to grid. This is not preferred for system control optimization, and the considerations include (1) limited battery capacity for high cost of Li-ion battery pack; (2) energy utilization efficiency.

Energy stored in the battery pack is preferred from renewable energy sources, therefore, storing renewable energy in battery and then discharging it to grid is inefficient when compared with sending renewable energy directly back to grid.

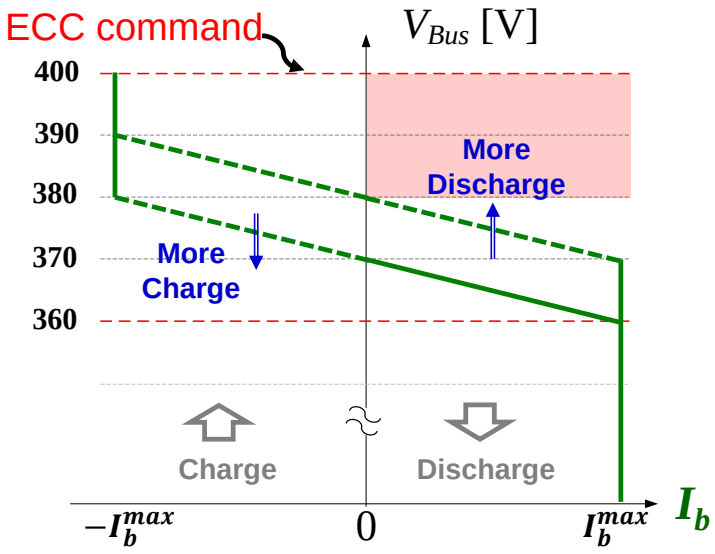

Figure 4.11 Battery energy scheduling by shifting battery role upward/downward

To summarize all control strategies for the battery energy, the energy control center (ECC) can flexibly manage and dispatch battery system energy follow for system level energy management optimization, eventually achieving Net-zero electric energy cost.

4.3 Energy Management System (EMS) Control and Experiment

4.3.1 Residential Load/PV Power Profile and Hourly Electricity Rate

To optimize energy management for the future home, a residential load demand profile and local solar irradiance play an important role to manage power flow in the period of a day/season/year and achieve Net-zero electric energy cost for residential customers. Figure 4.12 shows a few days' average hourly load demanding profile in winter and summer for an example of future house located in San Francisco, CA, USA [89]. In Figure 4.12 (a), the load demand

profile in winter normally has two peaks in breakfast and dinner time, which is different from summer condition with only one peak in dinner time within in 24 hours, shown in Figure 4.12 (b), because the air conditioner operates more heavily in summer. The wind power profile is not introduced here and will be part of the future work.

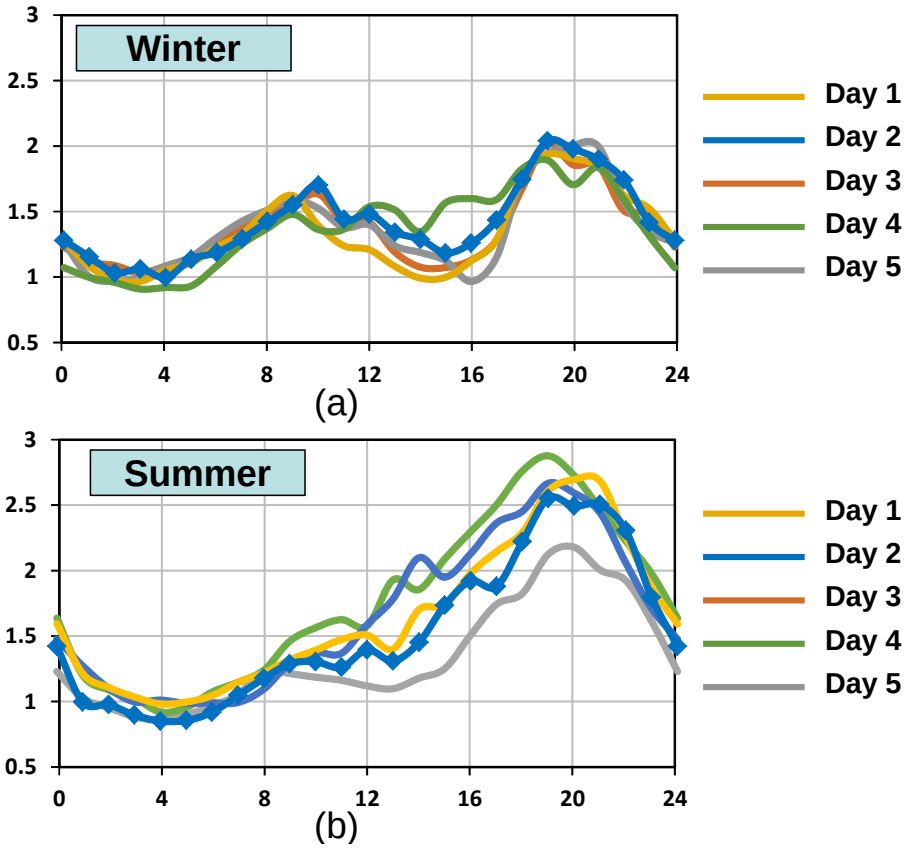

Figure 4.12 Load demand profile in 24hours, winter and summer

Along with the load demand profile, solar irradiance is also a variable which directly affects the PV output power. Figure 4.13 shows a few days' local solar irradiance profile for a future house located in San Francisco, CA [90]. It is clear to see that the solar irradiance profile in summer is higher than winter. What is more, depending on the different weather conditions, for example in a cloudy day, there will be very heavy fluctuations on solar irradiance; therefore, the PV converter output power will also be fluctuating. Generally speaking, the average solar

irradiance over 24 hours closely follows the sun positions, and is available from around 6:00am to 18:00pm, such as the clear day solar irradiance shown in solid pink line in Figure 4.13.

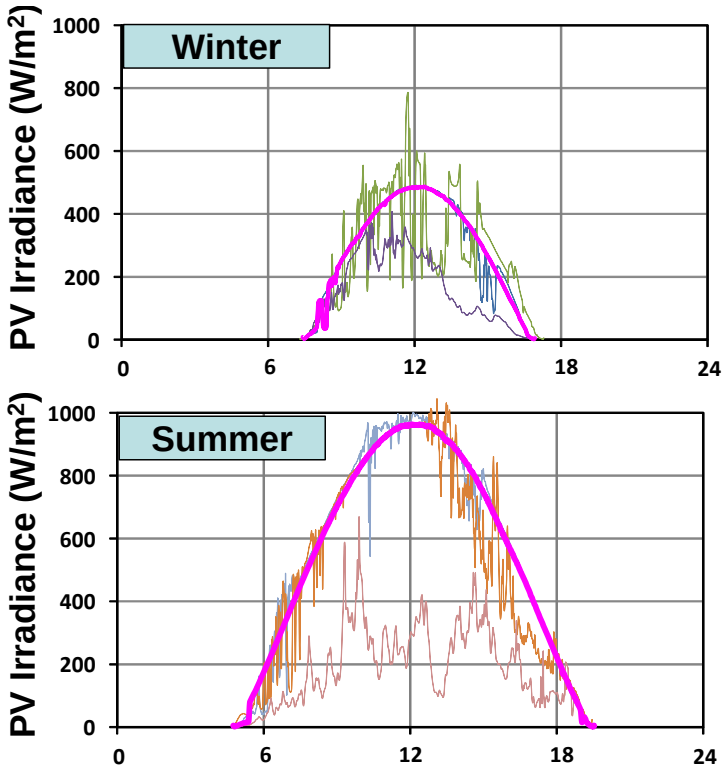

Figure 4.13 Solar irradiance profile in 24hours, winter and summer

What is more, the schedule of electricity rate from utility company [89] for the house during a day/24h, also called the time of use (TOU) , has three different electricity rate tiers , on-peak, part-peak and off-peak hours. On-peak hour is from 2:00pm to 09:00pm with around 40₵/kWh, shown with light-red shaded area in Figure 4.14. Part-peak hour's rate is around 20₵/kWh and comprised of two sections, 7:00am to 2:00pm and 09:00pm to 11:00pm, shown with light-pink shaded area Figure 4.14. All the other hours are off-peak hours and the off-peak hour electricity rate is around 10₵/kWh. Comparison between on-peak and off-peak hour rate, there is 4 times of difference. Therefore, managing the energy flow smartly during a day/24h

should consider both the load/source profile and electricity schedule to maximize the benefit for residential end users.

Summing all the considerations together, PV power, load demand and TOU electricity rate, Figure 4.14 shows all the information with an example future house located in San Francisco, CA [89][90]. One clear day data of PV in summer is selected, and the solar power capacity applied in the testbed is 4.6kW. Therefore, the available peak PV power in Figure 4.14 is around 4.2kW considering 950W/m^2 solar irradiation and wiring impedance. The average hourly load demand profile reaches peak around dinner time at 2.5kW. Considering non-coincidental residential load consumption, the instantaneous peak power can be over 10kW depending on how many appliances are running simultaneously.

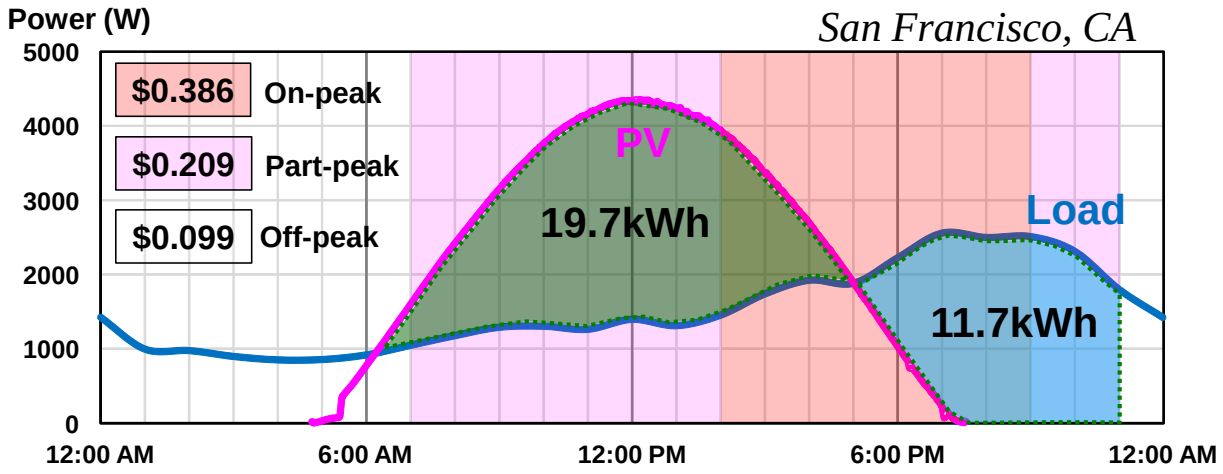

Figure 4.14 An example study considering PV/load demand profile and electricity rate

Figure 4.14 also calculates the total load energy consumption during the example 24h is 36.7kWh and total PV energy in this clear day is 37.7kWh. The load power and the PV power reach a rough balance. However, there is huge mismatch between solar power generation and load demand consumption. As shown in Figure 4.14, there will be 19.7kWh surplus power around noon and there will be 11.7kWh power deficiency during late afternoon and dinner time

where the electricity rate is the highest. Therefore, the energy management strategy will play an important role on the total electric bill annually. For example, 19.7kWh surplus energy from the PV can be used to charge battery during daylight and be discharged at night, especially during the on-peak load hours. To achieve a lower electric energy bill, another important factor is energy storage capacity and its sizing.

As illustrated in 2.1, the lithium-ion battery capacity is 13.8kWh in total and the available capacity is 9.7kWh, which corresponds to 70% of the depth of discharge (DoD) considering battery cycle life and battery system service life cycle up to 20~25 years. Therefore, the total 19.7kWh surplus energy cannot be totally used to charge battery energy, since the battery charge stops when it reaches 100% SoC. Solutions for the surplus energy can allow the ECC converter to operate in a regenerative mode, therefore, any surplus energy can also be sourced to grid by a net energy metering (NEM) service [89]. The utility company will then credit the customers with a NEM service. Sizing the energy storage is beyond the discussion of this paper and will be part of the future work.

To summarize the previous discussion in this section, the basic strategy for energy management control is concluded by firstly monitoring the energy for sources and loads in a year period and considering on/part/off hour electricity rate for energy usage. Then investigating an energy management strategy, especially on how to schedule energy storage power/energy, with the control strategy discussed in section 4.2. The ultimate goal is to achieve a net-zero electric energy cost in a yearly range.

4.3.2 10kW Emulator Testbed Configuration for DC Future Home

A 10kW future home emulator testbed for experimental demonstration includes four components: 1) Energy control center (ECC); 2) PV; 3) lithium-ion battery storage, and 4) load.

The ECC represents the utility interface. Solar energy represents the renewable energy components. A lithium-ion battery represents the energy storage components. Constant power load is considered to represent the house appliance load since all the load is interfaced with DC bus with power electronics converters. Therefore, the four above mentioned components, ECC, PV, Battery and load, form a minimized DC Nano-grid system, shown in Figure 4.15.

Total installed PV capacity is 5.1kW, including 30×150W PV panels from Suntech (ST170-24). For experimental convenience, 15 of E4361A Agilent solar simulators are used to emulate the 30 real panels, shown in Figure 4.15, which can be easily configured for all possible configurations mentioned in 3.2. Considering mismatches of solar irradiance among the panels, a dedicated DC-DC converter with an extra distributed MPPT (Max Power Point Tracking) algorithm, what is called a module integrated MPPT converter (PV panel optimizer) or smart converter (SC) addressed in 3.2, is connected to each panel to reduce the mismatch impact.

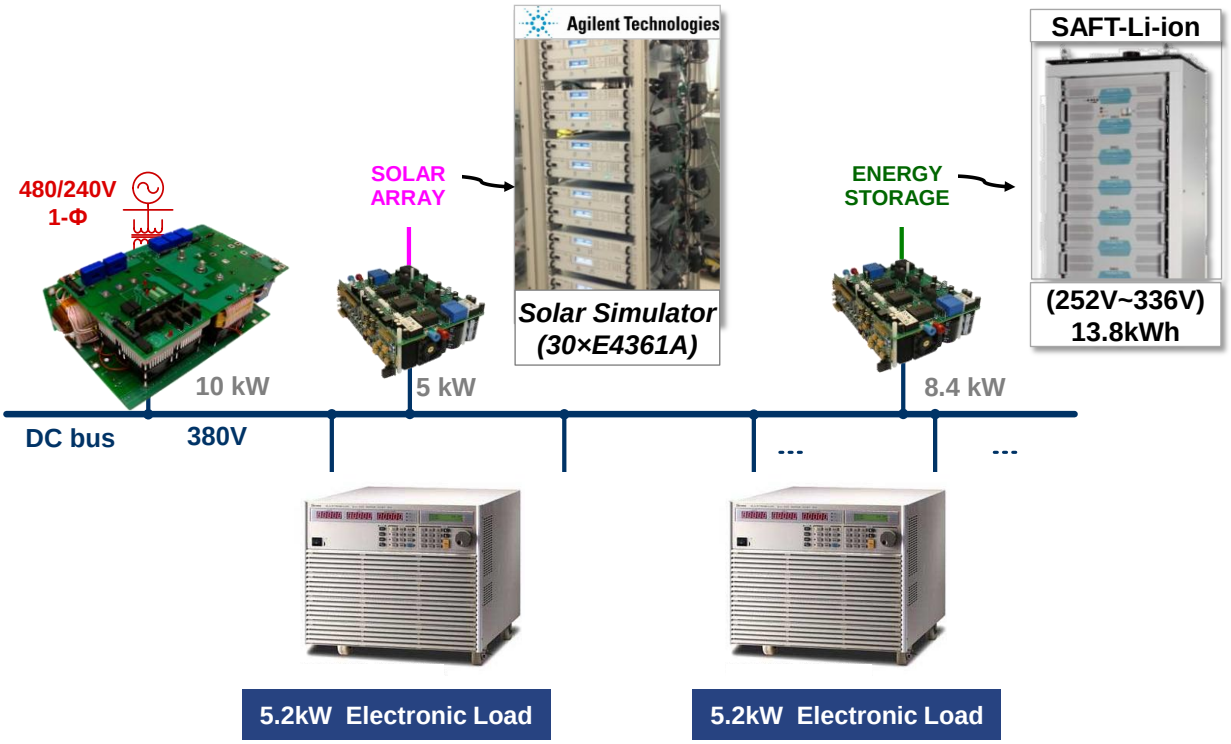

Figure 4.15 Hardware equipments used for DC Nano-grid

Electronic load pictures are from www.chromausa.com/instruments/electronic-loads/, Used under fair use, 2015
Battery picture is from http://www.saftbatteries.cn/sites/default/files/ess_market-brochure_en.pdf, Used under fair use, 2015

A 13kWh 45Ah lithium-ion battery from SAFT, discussed in detail in 2.1, is used for energy storage sources. Two 5.2kW DC electronic loads from Chroma are applied to emulate the house appliance. Importantly, all the active sources, including the PV panel level power and profile programming and communication, battery management system communication, load demand profile programming, can be remotely controlled by a remote computer to study the different kinds of cases, like severe mismatch of the PV, 24h load/PV power profile, house appliance load transient as well as islanded operation.

Figure 4.16 shows the 10kW emulator testbed for a DC future home, and all the above mentioned sources are interfacing with the DC bus with the dedicated power electronics converter. Since both of the input and output of the power electronics converter are sources with dedicated voltage when enabled, proper pre-charge circuits and circuit breakers are installed for the purposes of system startup and protection.

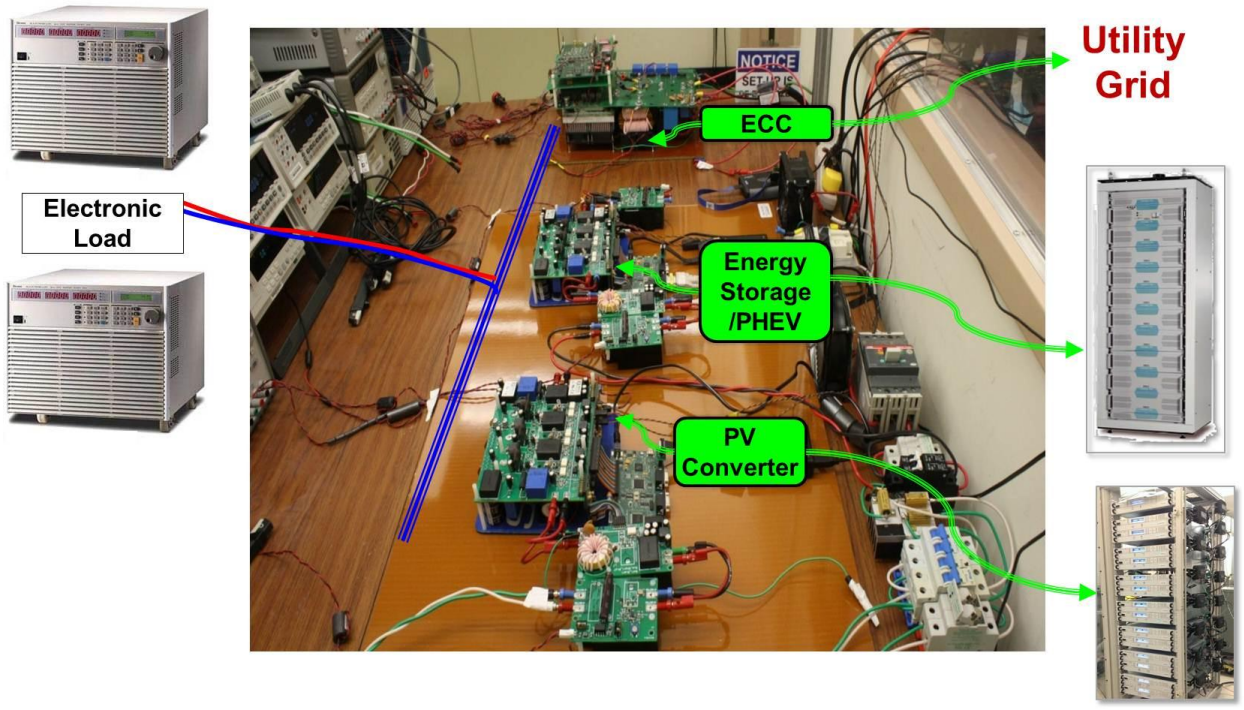

Figure 4.16 10kW emulator testbed for DC future home

Electronic load pictures are from www.chromausa.com/instruments/electronic-loads/, Used under fair use, 2015
Battery picture is from http://www.saftbatteries.cn/sites/default/files/ess_market-brochure_en.pdf, Used under fair use, 2015

In Figure 4.16, the ECC converter hardware prototype, shown in Figure 3.7, is used as single interface converter between the utility and the DC bus. The PV and energy storage converter hardware is using a Si-IGBT version three-channel interleaved buck/boost converter, shown in Figure 3.24, and the difference is that energy storage converter is bidirectional and the PV converter is unidirectional with one IGBT and one diode for each phase leg design.

For reliable system level test, there are four layers of protection.

1) Gate driver over current desaturation protection

   The first layer is over current protection which was integrated on the gate driver with V_{CE} desaturation based cycle by cycle detection and protection. This layer has the fastest responding speed; however, the desaturation protection current level is normally beyond 5-10 times of the device current rating, since it is decided by the gate driver steady state voltage, normally 15V for lower on-state voltage drop.

2) Hall current/voltage sensor detection and protection

   The second layer is based on a hall current/voltage sensor, which senses input/output current/voltage, compares with current/voltage references and generates a fault pulse to latch off all the active switches.

3) Redundant active semiconductor based circuit breaker

   The third layer of protection is an active semiconductor based circuit breaker which is used to disconnect the converter from active sources and the DC bus when a short happens in phase leg, unexpected cases or converter fault fails. The principle is still based on desaturation protection, however, the difference between the redundant protection circuit and the gate drive over current protection is that the current protection level in the redundant protection circuit is programmable, for example 25A

as the limit. This breaker will disconnect the converter with other sources or DC bus within 500ns after over current happens. The protection speed also depends on the input/output capacitance on the power stage filter. Generally speaking, the smaller the input/output capacitance on the converter, the faster the redundant converter will react.

4) Thermomechanical circuit breaker

The fourth layer is based on a thermomechanical circuit breaker, which reacts very slow and can only protect the wire from being melted with over current.

4.3.3 Energy Management System (EMS) Control Strategy Illustration and Experiment

To examine and demonstrate the proposed energy management control strategy, one day in summer, shown in Figure 4.14, is picked up for control illustration and experimental verification. The load demand profile and the PV source profile are remotely programmed according to the profile set in Figure 4.14. All the components included in this experiment setup are shown in Figure 4.17 where the current direction is the same as the experiment setup. All sources' current flows into bus, while the load current is measured flowing out of bus. Three examples within the selected 24 hour cases are investigated and illustrated as follows in a chronological way.

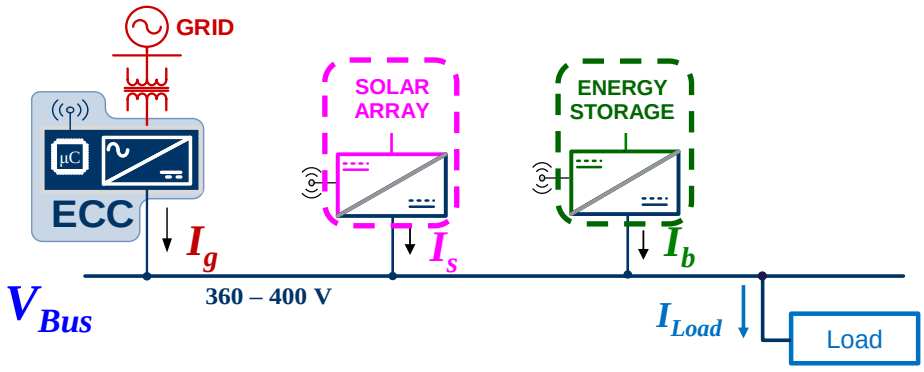

Figure 4.17 DC Nano-grid components for control illustration

4.3.3.1 Example 1 – 24h Energy Flow with Smart Energy Management

Stage 1: ECC in Rectifier Mode (Midnight to 6:00am)

This scenario example illustrates the control strategies that happen from midnight to 6:00am in the morning, shown in Figure 4.18. The ECC converter firstly supports the load and regulated the bus from midnight to early in the morning. As shown as point 1 in Figure 4.19, there is no PV power and the battery is in idle mode (I_S=I_b=0). The total load current is supplied by ECC (I_g=I_L). Due to the droop characteristics of the ECC converter in rectifier mode, the bus voltage is slightly lower than 380V. As shown in Figure 4.22, four currents, ECC output current (I_g) in dark red line, PV current (I_S) in pink line, load current (I_L) in dark blue line and battery current (I_b) in dark green line, are experimentally measured to emulate the setup for Stage 1. In Figure 4.22 before PV power appears, ECC current is equal to load current as 1kW.

After 5:00am in the morning, solar power, operating in MPPT mode, starts to step-in and shares power with the ECC converter. Solar power meets the load demand at t_2. As show in Figure 4.19, a new pink line, drawn with constant power designating 1kW power, supplies load current, therefore, a new power equilibrium point is found in point 2, where the bus voltage is 380V and there is zero net power flow in the ECC converter. At this moment, I_g=I_b=0 and I_S=I_L. In Figure 4.22 between point 1 and 2, it can be seen that I_S keeps increasing, corresponding with the decreasing I_g, which means less power is being supplied by utility grid.

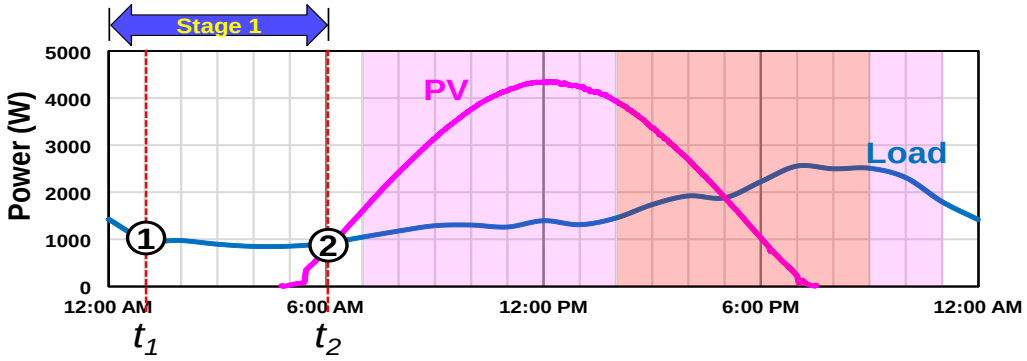

Figure 4.18 Stage 1 (ECC rectifier mode) – Midnight to 6:00am

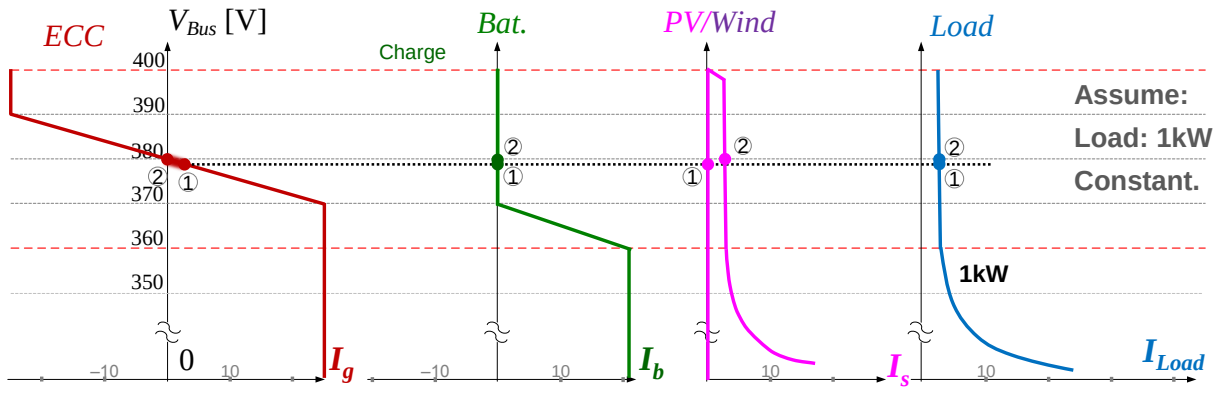

Figure 4.19 Control illustration for Stage 1

Stage 2: Charge Battery with PV Energy (6:00am to 11:00am)

This scenario example illustrates the control strategies that happen from 6:00am to 11:00am in the morning, shown in Figure 4.20. After solar power meets the load demand at t_2, solar power keeps increasing and exceeds load demand. The battery system operation is programmed by the energy control center (ECC) to adjust its battery charge power, taking the surplus PV energy. In this scenario, the initial SoC is assumed to be 30%, the minimum SoC in the morning. The control illustration during this scenario, including two steady states (solid dot point 2 and 3), is shown in Figure 4.21. Taking steady state (dot 3) for example, the battery charging current is programmed by the ECC converter to match the surplus solar energy, thus, the ECC converter regulates the bus voltage and there is no net energy flow during this scenario.

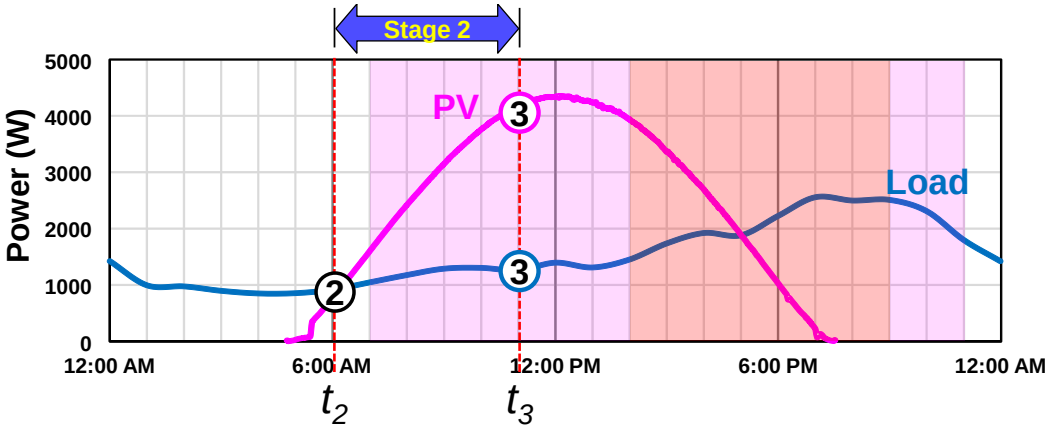

Figure 4.20 Stage 2 (Charging battery with PV energy) – 6:00am to 11:00am

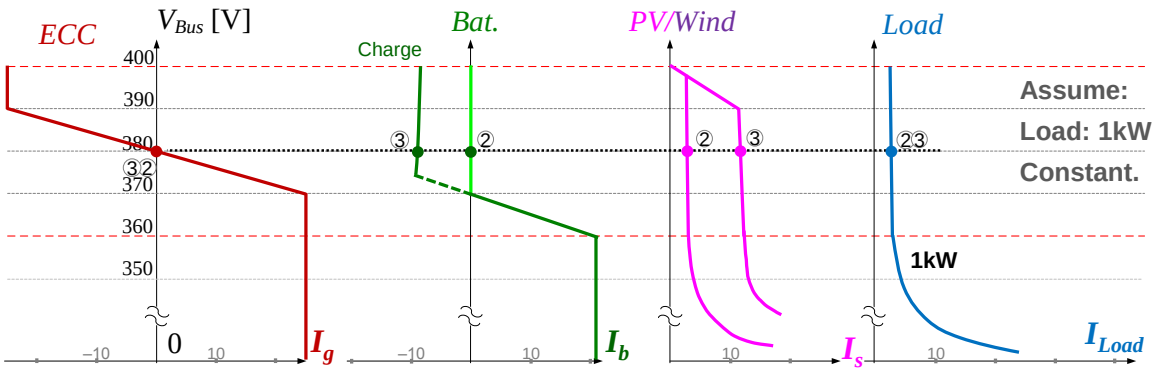

Figure 4.21 Control illustration for Stage 2

The right side of Figure 4.22 shows the experimental demonstration of example 2. Since the average load demand in Figure 4.20 is around 1kW, the load power in the experiment is assumed to be constant 1kW. After point 2 where PV and load power meet, in Figure 4.22, the battery charging current, negative means charging battery (refer to Figure 4.17), starts from zero and keeps increasing to match the surplus PV energy. What is more, it can be seen in Figure 4.22 that ECC current I_g stays at zero, which means that there is a net-zero energy flow on the ECC converter and all the free surplus energy is being charged to battery. Importantly, at every steady state point, a power balance/equilibrium must be satisfied, which can be expressed in (4.2),

$$I_g + I_b + I_S = I_{Load} \tag{4.2}$$

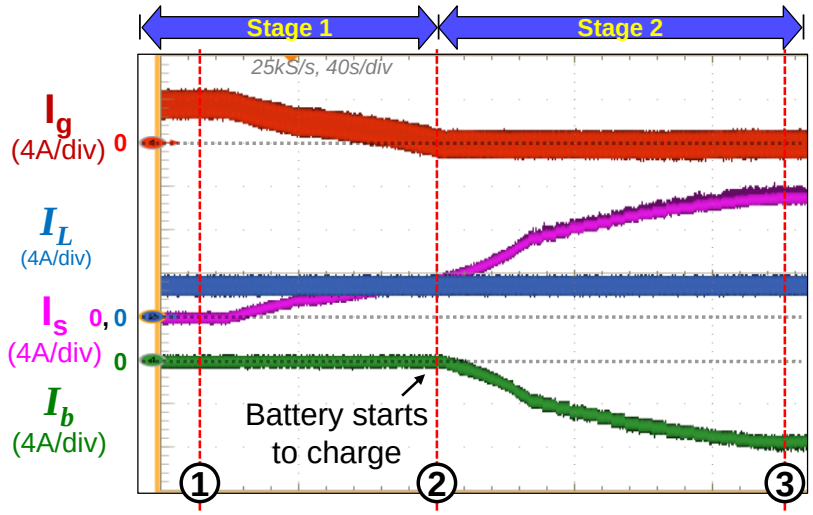

Figure 4.22 Experiment results for Stage 1 and 2

Stage 3: Battery Constant Voltage Charging (11:00am to 12:00pm)

Scenario stage 3 illustrates the control strategies that happen from 11:00am to 12:00pm in the morning, shown in Figure 4.23. During this timeframe, due to the fact that surplus solar power keeps charging the battery, SoC reaches 100% around the noon time which means the charging power will be regulated by the battery management, V_{Cell_Max} controlled charging profile. And the surplus energy will begin to be sourced to grid. The control illustration corresponding to this scenario is shown in Figure 4.24 with constant PV power and load demand, where two steady states are highlighted, t_3 and t_4. The battery management system in CV mode regulates the battery charging current and decreases logarithmically during t_3~t_4. At steady state t_4, the battery has been fully charged and the charging current drops to zero, shown in Figure 4.24, and all the surplus energy is source from PV to grid through the ECC converter. Therefore, the bus voltage increases over 380V and the ECC converter enters regenerative mode.

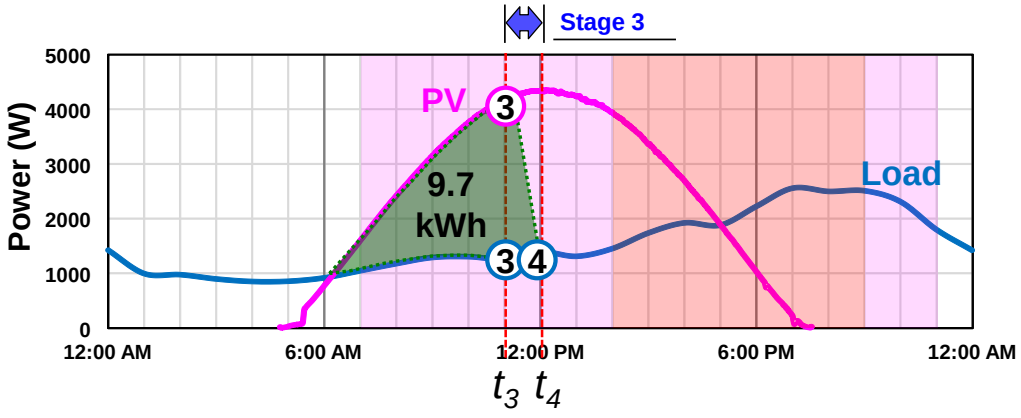

Figure 4.23 Stage 3 (Battery CV mode charging) – 11:00am to 12:00pm

Figure 4.25 shows the experiment and corresponds to the control illustration in Figure 4.24. As seen in Figure 4.25, battery charge current, I_b, reversely decreases, and corresponds to ECC power, I_g, reversely increases, which shows that the increasing surplus PV power is sourced to the grid while PV system is always operating in maximum power tracking mode.

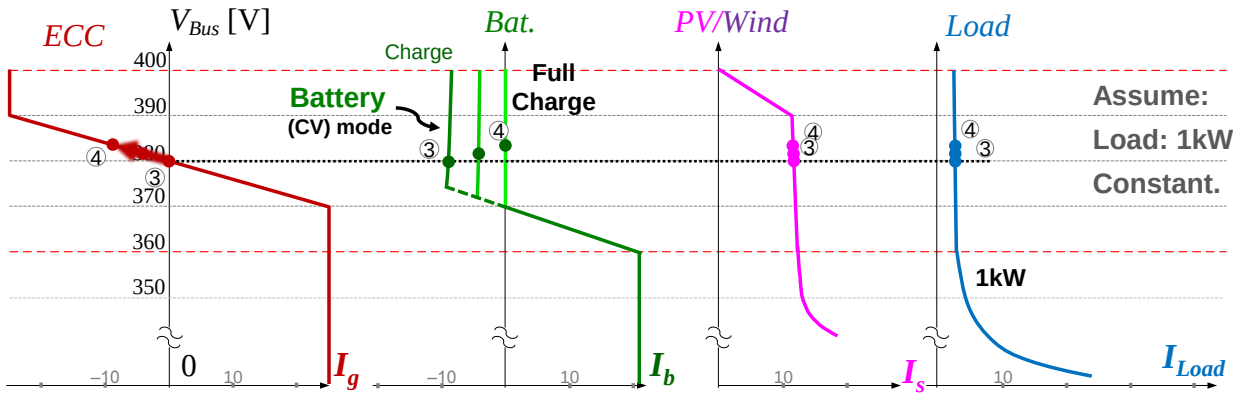

Figure 4.24 Control illustration for Stage 3

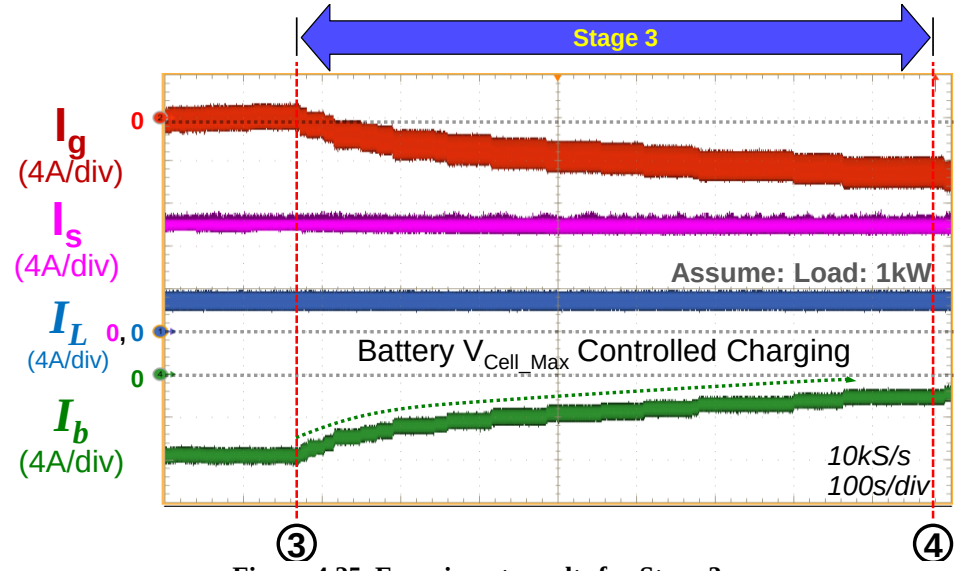

Figure 4.25 Experiment results for Stage 3

Stage 4: PV Energy Sourced to Utility Grid (12:00pm to 05:00pm)

Scenario stage 4 illustrates the control strategies that happen from 12:00pm to 05:00pm in the afternoon, shown in Figure 4.26. At steady state t_4, the battery is fully charged and cannot accept any additional power. Therefore, the battery charging current is limited to zero, shown in Figure 4.27. PV power decreases accompanied by load demand increases leads to decreased ECC sourcing energy to grid. Two critical moments, t_4 and t_5, are shown in Figure 4.27. At steady state t_5, the PV output power decreases and is the same with load power, thus, the surplus power sourced to the grid decreases to zero with the bus voltage regulated by ECC at 380V.

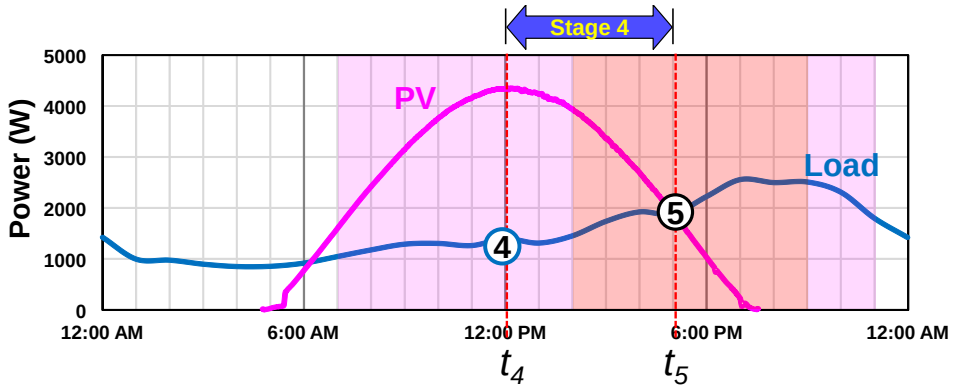

Figure 4.26 Stage 4 (PV energy to utility) – 12:00pm to 5:00pm

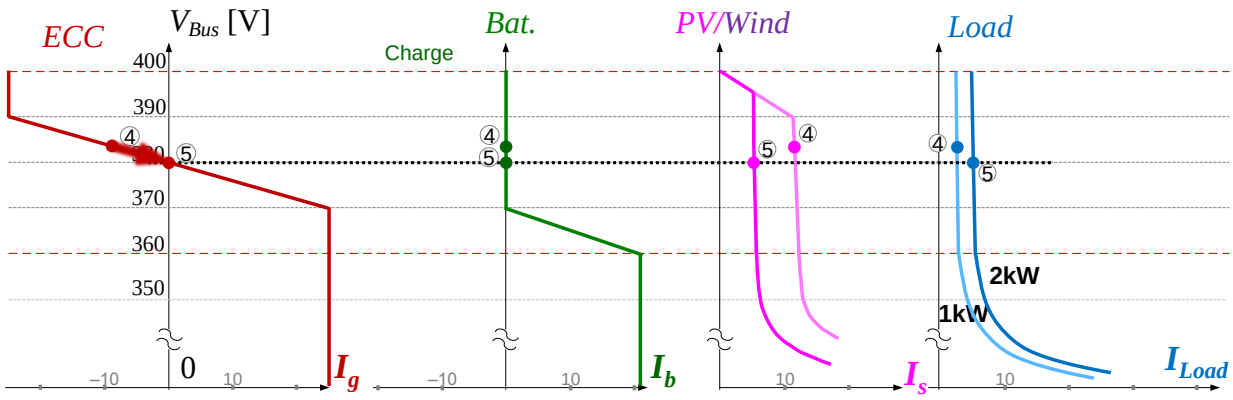

Figure 4.27 Control illustration for Stage 4

Figure 4.28 shows the experiment results for Example 4. I_b stays at zero since the battery is fully charged, and I_g, ECC current, reversely decreases to zero when PV power (I_S in pink line) is equal to load power (I_L in dark blue line) at t_5.

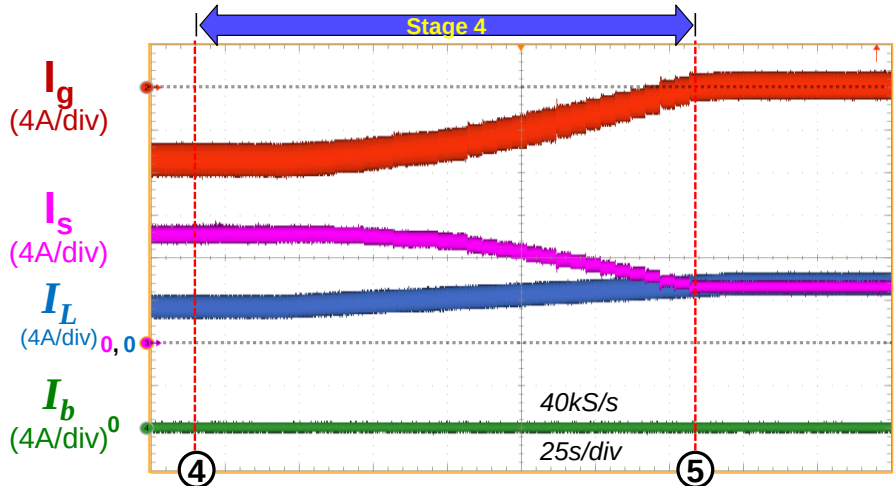

Figure 4.28 Experiment results for Stage 4

Stage 5: Shift battery role upward/downward (5:00pm to 11:00pm)

Scenario example 5 illustrates the control strategies that happen from 5:00pm to 11:00pm, as shown in Figure 4.29. This example is used to demonstrate that the ECC commands the battery control law to shift upward and share load with the ECC converter, alleviating on-peak hour load demand for the grid and saving on the electricity bill. A solid light green line in Figure 4.30 shows the default control law with a charge current limit to be zero for the battery converter. During this time stage, the TOU is at on-peak hours with the most expensive electricity rate, and generates most of the electricity bill.

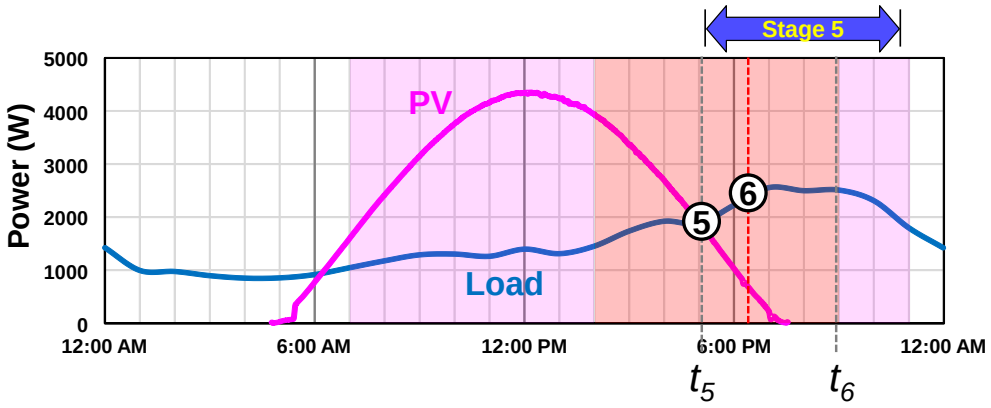

Figure 4.29 Stage 5 (Shift battery role upward/downward) – 5:00pm to 11:00pm

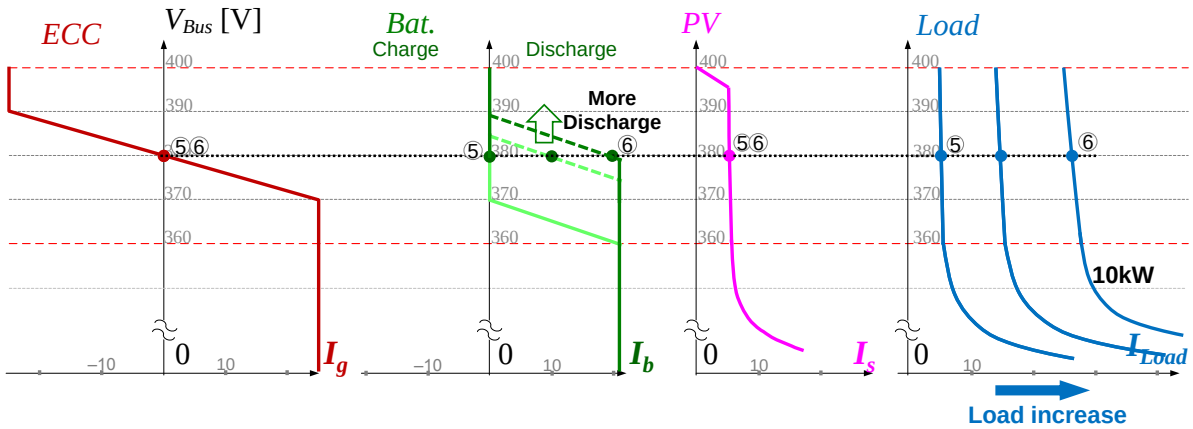

Figure 4.30 Control illustration for Stage 5

With a flexible battery control law commanded by ECC to shift it upward (shifting battery role upward tends to discharge battery more, refer to 4.2.3, a certain amount of discharging current will be drawn from the battery to share the load with the ECC. Figure 4.30 shows the battery discharged current increasing from steady state '5' to steady state '6' corresponding to a load increase, and the ECC current stays at zero with net zero energy flow. The higher the battery role is shifted up, the more energy is discharged by the battery. As show in Figure 4.30 from '5' to '6', the solid steady state dots are shifting to right with more discharged current. Importantly, it is not preferred to shift the battery role up further, since battery energy will be sent back to grid. The potential concerns include: 1) Limited battery stored energy; 2) lithium-ion battery cycle life; 3) low energy conversion efficiency (PV energy → battery → ECC → utility grid) with multiple stages of energy conversion. Similarly, all the regions over 380V with a positive battery current, shown in Figure 4.11, will always lead to battery energy being sourced to the grid, which should be avoided by smart energy management, refer to 4.2.1.

Figure 4.31 shows the experiment for shifting the battery role upward, the increased battery discharge current leads to net-zero current from utility.

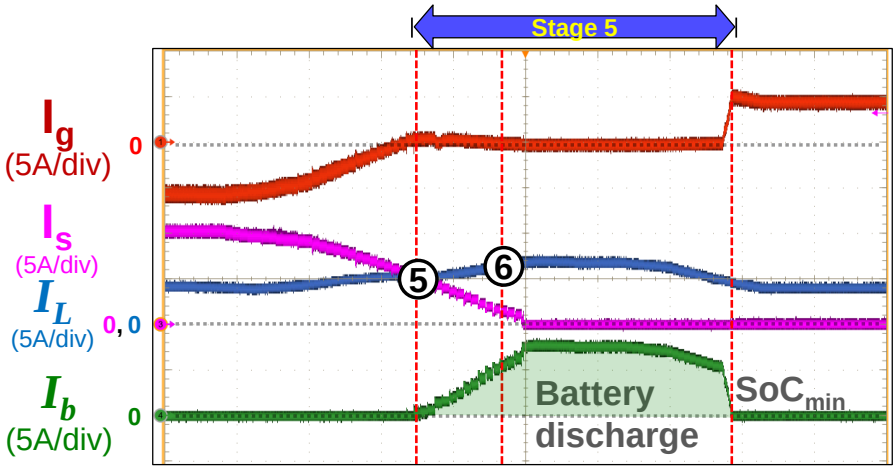

Figure 4.31 Experiment results for Stage 5

4.3.3.2 Example 2 – Battery discharge bus regulation below 370V

Example 2 is used to demonstrate the robustness of the system at over load conditions, and illustrates the control strategies that happen when the instantaneous load exceeds the ECC converter current limit during heavy load on-peak hours. The battery converter starts to discharge energy for the bus regulation when ECC enters a current limiting mode, extending the load operating range. For example, air conditioner turns on when the washer and dryer are operating at heavy load.

With stage 5 of example 1 to be the initial point, Figure 4.32 illustrates the battery's discharge regulation below 370V when ECC enters the current limiting mode, and the steady state point 5′ serves as an example with ECC in current limit mode and the battery converter is in discharge droop voltage regulation. The experiment for this scenario is shown in Figure 4.33: (a) without battery; (b) with battery. Without battery energy back up, the DC bus voltage droops immediately as the ECC converter enters current limit mode, show as blue line in Figure 4.33 (a). With battery energy backup and discharge regulation under 370V, it is clear that the battery converter current immediately catches up as ECC enters the current limiting mode and saves the bus voltage after a load transient, which is highlighted on the black dash-line.

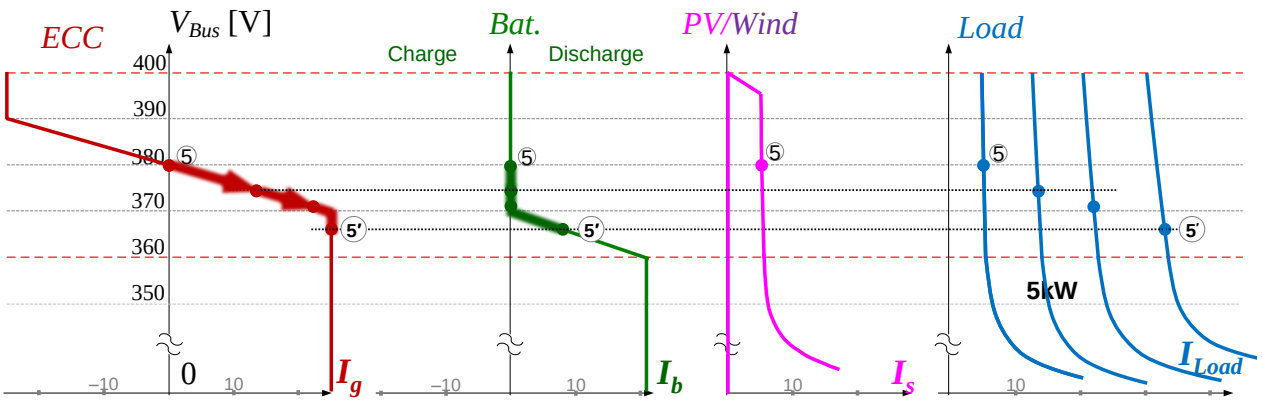

Figure 4.32 Control illustration for Example 2

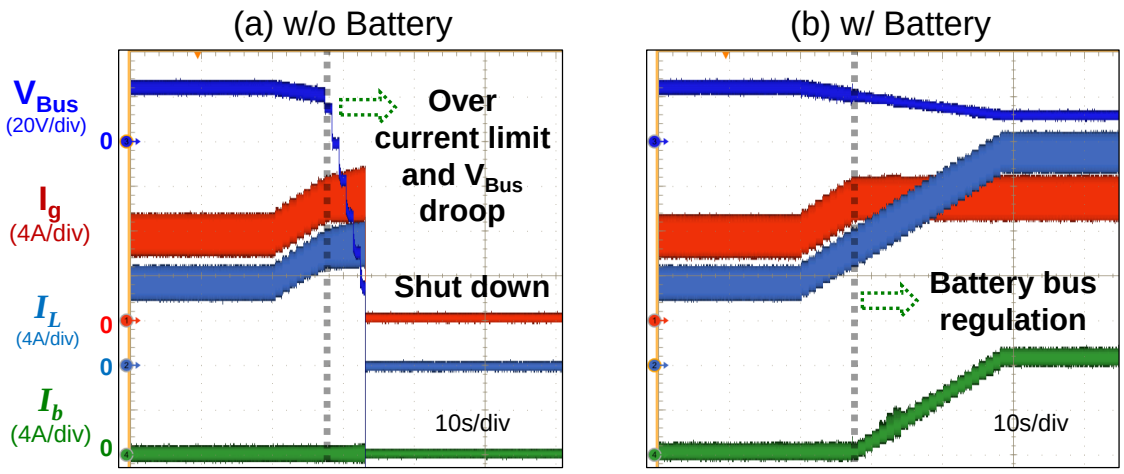

Figure 4.33 Experiment results for Example 2

4.3.3.3 Example 3 – PV bus regulation over 390V

Example 3 is used to demonstrate the robustness of the system when the ECC converter has limited capability to send surplus PV energy to the grid, or ECC is operating in an islanded mode with no bidirectional energy control capability. Without proper control strategy, surplus PV energy from maximum power point tracking (MPPT) will charge the DC bus capacitor and eventually cause system shut-down by over voltage protection. Based on the proposed control strategy over 390V, shown in Figure 4.6, the PV converter will regulate the bus voltage over 390V and give up MPPT operation within this voltage range. Therefore, it could allow the system still operating with the bus voltage regulated by the PV converter. Figure 4.34 shows the control strategy illustration with the initial condition of a steady state '4' in stage 4 of example 1. At steady state '4', the surplus PV energy is sourced to the grid through the ECC converter, and the bus is regulated by the ECC converter. Suddenly, a load decrease (assume the PV power is constant) will lead to more surplus energy sourced to the grid. However, with current limit of ECC converter to be maximally 5A, the bus capacitor will be charged and bus voltage increases

due the additional PV energy. Over 390V, the PV converter gives up the MPPT operation and start to regulate the DC bus, thus a new power equilibrium point is found at steady state point '4''. To the worst case, the ECC converter is islanded and disconnected with the grid, no more energy could be sourced to the grid, and the PV converter will continue decrease the PV output power and regulate the DC bus voltage based on droop characteristics from 390~400V, shown as steady state point '4'''.

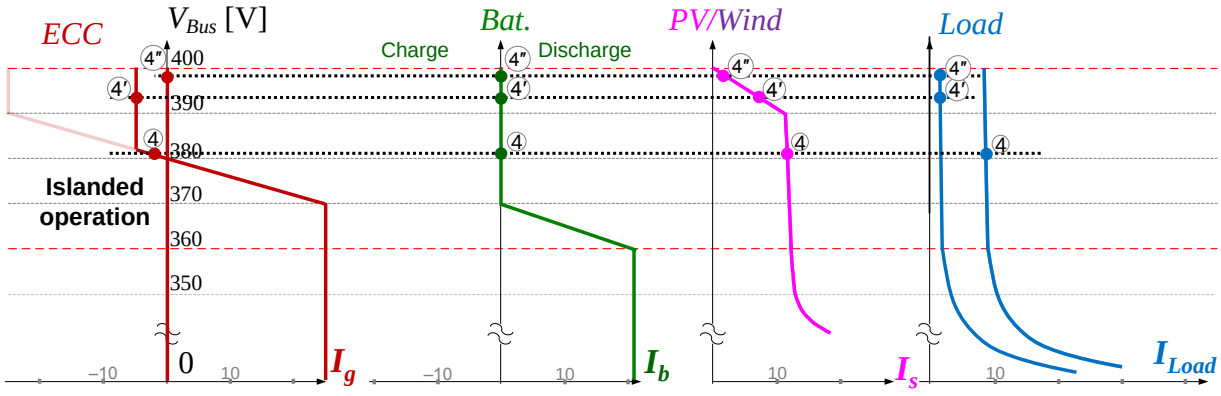

Figure 4.34 Control illustration for Example 3

Figure 4.35 shows the experiment waveforms of example 3. At steady state point '4', the surplus PV energy is sourced to the grid through the ECC converter, negative current means energy flows back to grid, and the ECC converter regulates the bus voltage. After steady state point '4', load starts to decrease and leads to more sourced energy to grid, see reversely increased red waveform, I_g, in Figure 4.35. After the first grey vertical dash line, the ECC source current reaches 5A limit, the additional PV energy charges the bus capacitor and the bus voltage increases, shown in blue waveform 'V_{BUS}' at the top of Figure 4.35, and the PV converter stops the MPPT operation and starts to regulate the bus side voltage by reducing PV energy corresponding to a load decrease, shown in pink waveform 'I_S' in Figure 4.35. Steady state point '4'' is a new power equilibrium point with the PV converter regulating the bus voltage and the

ECC converter is under current limiting mode – -5A grid sourcing current. At the moment of the second grey vertical dash line, the ECC converter is disconnected from the utility and I_g drops to zero. The PV converter reacts with decreased PV energy, with bus voltage increases a little bit due the droop characteristics, and reaches another power equilibrium point, '4''.

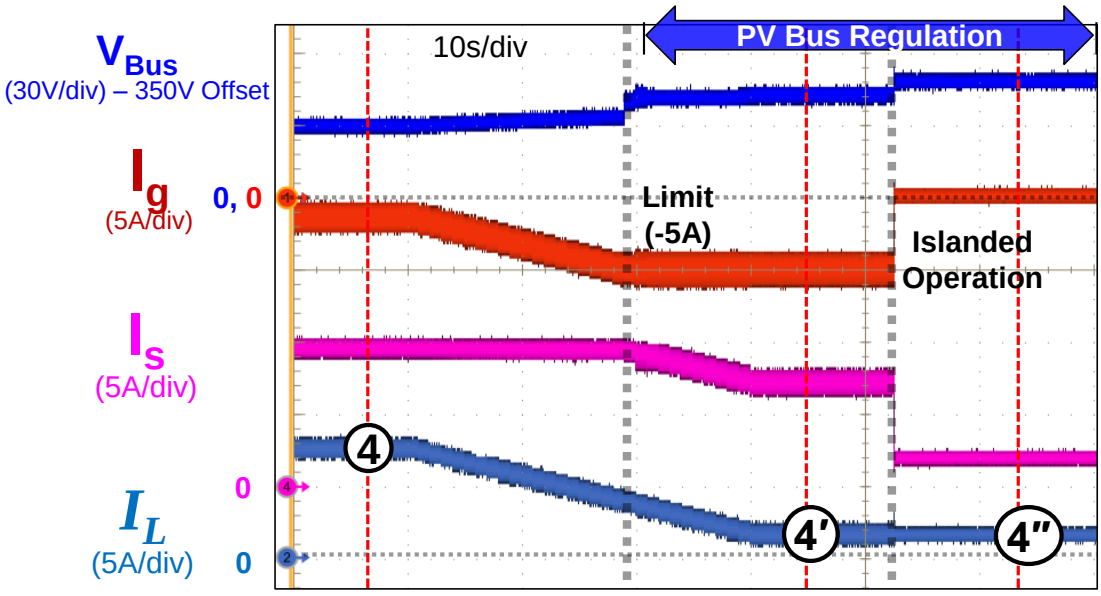

Figure 4.35 Experiment results for Example 3

4.4 Energy Flow Summary and Net-zero Electric Energy Cost Discussion

To summarize the control strategies for all components discussed in section 4.2 and 4.3, Figure 4.36 (a) summarizes and highlights the 24h energy flow region with different colors. Figure 4.36 relates the energy flow with the electricity prices which presents us clues for smart energy management to achieve Net-zero electric energy cost:

1) At off-peak hours, it is preferred to use utility energy to supply load.

2) Surplus renewable energy is preferred to charge the battery first (Surplus PV energy → Battery), and the considerations include: 1) Free PV energy; 2) fewer stages energy conversion comparing (PV→Utility→Battery); 3) mitigate the

burden with high renewable energy sourced to grid – grid voltage increase and frequency increase, referred to 1.2.1.

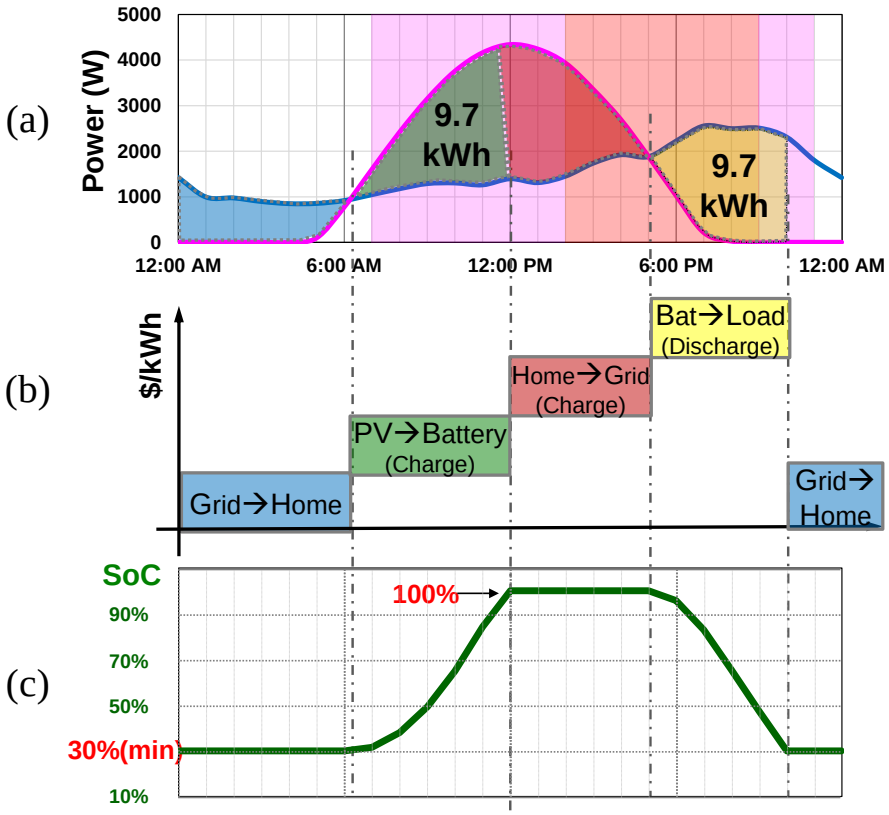

Figure 4.36 24h Energy flow summary and energy management strategy

3) A battery management system sets the voltage and current limit to protect the lithium-ion battery from over charge/discharge under any conditions.

4) A flexible energy management strategy on the battery helps the battery energy to be dispatched at required, such as discharge during on-peak hours. This can save the electricity bill and mitigate the utility company heavy load issues which decide the total system capacity installation and corresponding transmission investment, referred to 1.2.

Figure 4.36 (c) shows the SoC variation under the studied energy flow profile in Figure 4.36 (a) and (b), with a minimum SoC (30%) at midnight and a maximum SoC (100%) during noon solar-rich hours, finally discharged to 30% during on-peak hours.

To give a systematically 24h view of all the involved energy flow, Figure 4.37 (b) shows the experiment results with the PV and load profile programmed to be similar to Figure 4.37 (a). The 24h experiment is scaled down to an approximate 1h experimental test due to the scope's limited capture range and resolution. All the components included in this experiment setup are shown in Figure 4.15, with ECC, PV, battery and load. Current direction shown in Figure 4.15 is referred to as experimental measured direction. All sources current flows into bus, while load current is measured flowing out of bus. All the waveform color is adjusted in the scope and matches the control law current shown in Figure 4.6. The time sequences of Figure 4.37 (b) roughly correspond to Figure 4.37 (a) with the vertical dotted lines highlighting the critical transitions. The control strategies and sequences applied for this experiment are addressed in detail in section 4.3.3 from Example 1 to Example 3, and they are not repeated here.

Considering the 24h case study with electric utility electricity price, the electricity bill will be $9.35 without battery and PV energy, and the electricity bill will be decreased to -$0.32 when 5kW PV energy is installed in the REN system. More importantly, more saving on the electrical cost can be achieved by adopting energy storage and managing it with the flexible and smart control strategies, further decreasing the bill to -$1.63, which not only saves on the electricity bill, but also alleviates intensive the intensive PV power introduced voltage and frequency increase on the utility grid.

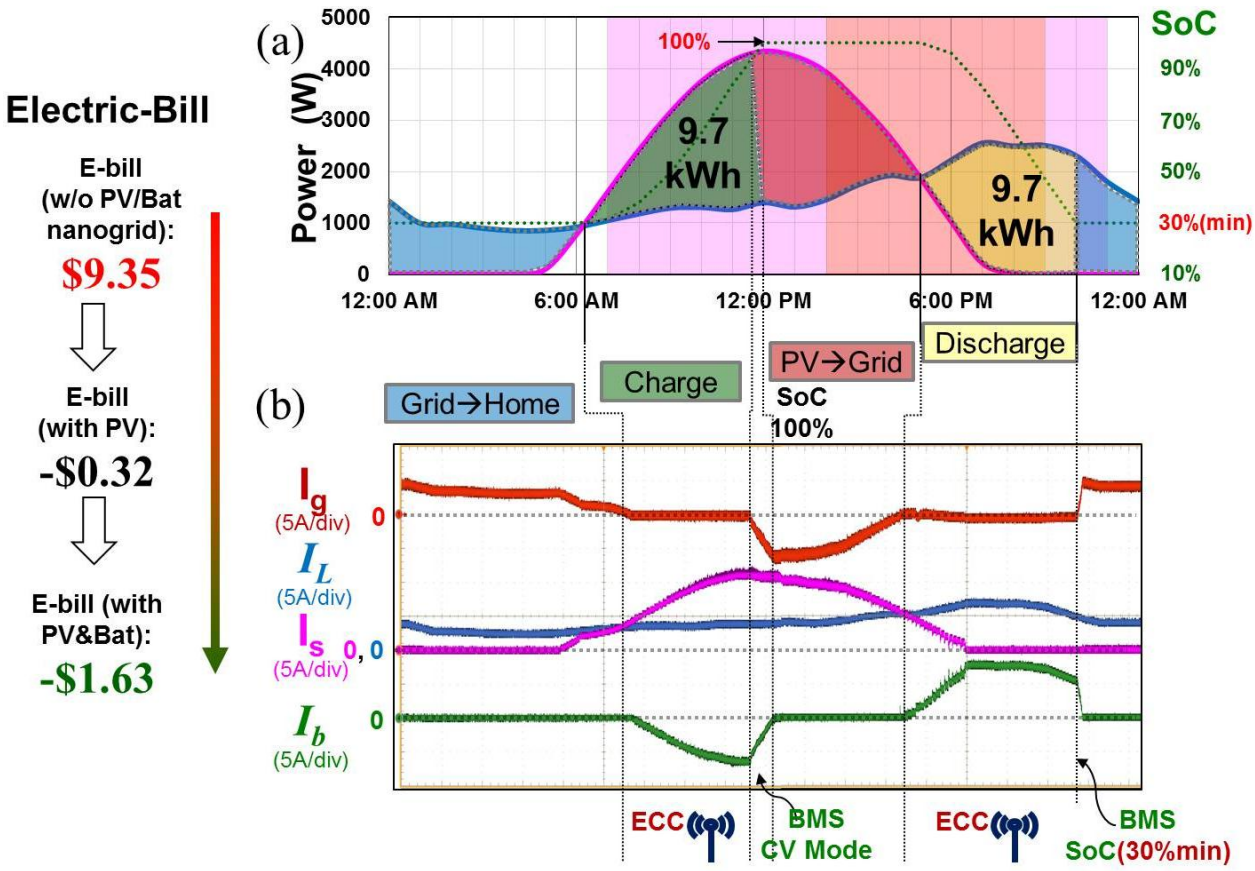

Figure 4.37 24h energy flow experiment and electric bill calculation

4.5 Summary

This chapter explains the control objectives of every key source component, and then proposes a distributed droop control method to integrate all the sources and their converters. Control strategies in the component level and system level are defined and discussed, and energy storage management with its control law in the DC Nano-grid is proposed. System level energy management control strategies in a 24 hour day are examined and discussed with considerations of residential load demand profile, local renewable energy source profile and schedules of electrical rate. A 10kW DC future home emulator testbed is prepared and introduced; all the discussed control strategies are experimentally validated.

Chapter 5 Conclusions and Future Work

5.1 Conclusions

To enable a Net-zero electric energy cost and optimize power management for future homes or buildings, the DC electric distribution systems (DC Nano-grid) find feasibility and simplicity in integrating multi-type renewable energy sources. However, integrating all the sources and loads in a simple, reliable and smart way is still challenging.

Dissipative cell equalization is studied for high voltage lithium-ion battery energy storage. Non-dissipative equalization methods are reviewed using an energy flow chart. Typical charging schemes considering total battery bank voltage to control the constant voltage charging and the related over-charge risk are illustrated. A lithium-ion battery charging profile based on $V_{Cell\_Max/Min}$ monitoring is proposed and the design consideration with CAN bus communication are addressed and validated with experimental results in an 8.4kW bidirectional battery charger for the DC future home.

For the DC future home emulator testbed design, an ECC converter is reviewed with identification of its system function. A residential PV system with different configurations are compared with severe mismatch cases studied to further expanding the common MPPT region, thus increasing the maximum power. An 8.4kW multi-phase bidirectional battery charger with Si IGBT in DCM operation is designed to achieve high efficiency and to be the interface converter between lithium-ion battery and the DC bus. Power device candidates considering smaller switching loss and conduction loss are compared and discrete Infineon Si-IGBT with TO-220

package is selected for the phase-leg design. Switching performance, including turn-on and turn-off loss of the target device, is characterized with double pulse tester for accurate loss model and loss breakdown. CCM and DCM operation is compared considering the switching loss and inductor volume. Finally, an 8.4kW bidirectional converter prototype is implemented and tested for the purpose of system integration and energy management study.

For the DC future home energy management system, this thesis proposes a distributed droop control method and a smart energy management with comparison of centralized and decentralized control, and then investigates the proposed control laws for energy storage to enhance the Net-zero electric energy cost. Finally, all of the control functions, in system and component level, are applied to the DC future home with interactions among the energy control center (ECC), renewable energy sources and load variation during a 24 hour day. What is more, system level energy management control strategies for a Net-zero electric energy cost are examined and illustrated. 10kW future home emulator testbed is build and introduced. Finally, all the concepts are experimentally verified with considerations for the 24 hours residential load demand and the renewable power profile.

5.2 Future Work

All of the discussions, including battery management system optimization, testbed design consideration and energy management strategy, provide clues and evidences in system and components level that the DC future home can help to achieve a Net-zero electric energy cost in a simple, reliable and robust way. To further improve the DC Nano-grid concept for adoption in future Smart Grid, the following research topics can be continued:

1) Non-dissipative cell equalization and its practical design considerations in high voltage lithium-ion battery system. A smart battery module with an integrated battery charger/discharger and non-dissipative cell equalizer.
2) To achieve a Net-zero electric energy cost with minimum investment in the equipment, solar/wind and battery capacity require detailed modeling of the PV/wind/load profile in terms of yearly range, and optimally sizing the components considering the proposed energy management strategy.
3) More dynamics and detailed small signal modeling among multiple sources can be studied for system stability analysis.
4) Reliable system communication protocol.

References

[1] Loh, P.C.; Ding Li; Yi Kang Chai; Blaabjerg, F., "Autonomous Operation of Hybrid Microgrid With AC and DC Subgrids," Power Electronics, IEEE Transactions on , vol.28, no.5, pp.2214,2223, May 2013.

[2] Boroyevich, D.; Cvetkovic, I.; Burgos, R.; Dong Dong, "Intergrid: A Future Electronic Energy Network?," Emerging and Selected Topics in Power Electronics, IEEE Journal of , vol.1, no.3, pp.127,138, Sept. 2013.

[3] "Annual Energy Outlook 2015," Report No. DOE/EIA-0383(2015), U.S. Department of Energy (DoE) / Energy Information Administration (EIA), Apr 2015.

[4] "Annual Energy Review 2011," Report No. DOE/EIA-0383(2011), U.S. Department of Energy (DoE) / Energy Information Administration (EIA), Sep 2012.

[5] National Renewable Energy Laboratory, “Energy innovations science & Technology at NREL,” winter 2010.

[6] K.C.Divya, Jacob Stergaard, “Battery energy storage technology for power systems - an overview,” Electrical Power System Research, Volume 79, Issue 4, April 2009, Pages 511-520

[7] P. Torcellini, S. Pless, M. Deru, D. Crawley, "Zero energy buildings: A critical look at the definition", NREC/CP-550-39833, National Renwable Energy Laboratory and U.S. Department of Energy, Jun 2006

[8] Po-Wa Lee; Lee, Y. -S; Bo-Tao Lin, "Power distribution systems for future homes," Power Electronics and Drive Systems, 1999. PEDS '99. Proceedings of the IEEE 1999 International Conference on , vol.2, no., pp.1140,1146 vol.2, 1999

[9] Pratt, A.; Kumar, P.; Aldridge, T.V., "Evaluation of 400V DC distribution in telco and data centers to improve energy efficiency," Telecommunications Energy Conference, 2007. INTELEC 2007. 29th International, Sept. 30 2007-Oct. 4 2007

[10] Bryan, J.; Duke, R.; Round, S., "Decentralized generator scheduling in a nanogrid using DC bus signaling," Power Engineering Society General Meeting, 2004. IEEE , vol., no., pp.977,982 Vol.1, 6-10 June 2004

[11] K. Sun; L. Zhang; Y. Xing; Guerrero, J.M., "A Distributed Control Strategy Based on DC Bus Signaling for Modular Photovoltaic Generation Systems With Battery Energy Storage," Power Electronics, IEEE Transactions on , vol.26, no.10, Oct. 2011

[12] Kakigano, H.; Nishino, A.; Ise, T., "Distribution voltage control for DC microgrid with fuzzy control and gain-scheduling control," Power Electronics and ECCE Asia (ICPE & ECCE), 2011 IEEE 8th International Conference on , May 30 2011-June 3 2011

[13] Riffonneau, Y.; Bacha, S.; Barruel, F.; Ploix, S., "Optimal Power Flow Management for Grid Connected PV Systems With Batteries," Sustainable Energy, IEEE Transactions on , vol.2, no.3, pp.309,320, July 2011

[14] N. G. Hingorani and L. Gyugyi: Understanding FACTS: Concepts and Technology of Flexible AC Transmission Systems. New York: IEEE Press, 2000.

[15] X. P. Zhang, L. Yao, B. Chong, C. Sasse, and K. R. Godfrey, “FACTS and HVDC Technologies for the Development of Future Power Systems,” in International Conference on Future Power Systems, 2005, pp. 1-6.

[16] Cvetkovic, I.; D. Dong; W. Zhang; L. Jiang; Boroyevich, D.; Lee, F.C.; Mattavelli, P., "A testbed for experimental validation of a low-voltage DC nanogrid for buildings," Power Electronics and Motion Control Conference (PEMC), 15th International , Sept. 2012

[17] Wei Zhang; Dong Dong; Cvetkovic, I.; Lee, F.C.; Boroyevich, D., "Lithium-based energy storage management for DC distributed renewable energy system," Energy Conversion Congress and Exposition (ECCE), 2011 IEEE , vol., no., pp.3270,3277, 17-22 Sept. 2011

[18] Wei Zhang, Fang Chen, Fred C. Lee. Pinyu Huang, “Energy Management Control and Experiment for DC Future Home Part 1 – 380V DC System Testbed,” CPES Annual conference, 2014, CPES Conference 2014, Blacksburg, VA (April 6-8, 2014)

[19] Eyer, J. and G. Corey. "Energy Storage for the Electricity Grid: Benefits and Market Potential Assessment Guide". SAND2010-0815, Sandia National Laboratories, February 2010.

[20] http://energystorage.org/, Energy storage association.

[21] “Rechargeable Li-ion OEM Battery Products”, Panasonic.com. Retrieved, 2010-04-23;

[22] “SANYO Launches it’s Long Awaited Rechargeable Battery with High Capacity and Low Self-discharge. ” www.sanyo-component.com;

[23] Andrew Burke, “Ultracapacitors: why, how, and where is the technology”, Journal of Power Sources, 2000;

[24] “Lithium Technologies”, www.saftbatteries.com;

[25] Jim McDowall, "Sophistication versus simplicity: System design considerations for lithium-ion batteries in standby power applications", The Battcon 2010 Proceedings, Hollywood, FL.

[26] Jim McDowall, "Understanding lithium-ion technology", The Battcon 2008 Proceedings, Marco Island, FL.

[27] Jim McDowall, "A guide to lithium-ion battery safety", The Battcon 2014 Proceedings, Boca Raton, FL.

[28] Jim McDowall, "Comparing apples and oranges: Guidance on the adoption of new technologies", The Battcon 2011 Proceedings, Orlando, FL.

[29] Jim McDowall, "A stationary battery in every home? Predicting the future for residential energy storage", The Battcon 2007 Proceedings, Tampa, FL.

[30] Jim Mcdowall, “Lithium-Ion Battery Chemistries: Strengths and Weaknesses”, Presentation, Blacksburg, VA, 2009;

[31] William H. DeLuca, “System and Method for Charging electrochemical cells in series”; US4238721;

[32] Douglas C. Hopkins, “Dynamic Equalization During Charging of Serial Energy Storage Elements”, IEEE Transactions on Industry Applications, 1993;

[33] Kutkut, N.H.; Divan, D.M., "Dynamic equalization techniques for series battery stacks," Telecommunications Energy Conference, 1996. INTELEC '96., 18th International , vol., no., pp.514,521, 6-10 Oct 1996

[34] Ikeda, N.; Kaya, S.; Jiang Li; Sato, Y.; Kato, S.; Yoshida, S., "High power AlGaN/GaN HFET with a high breakdown voltage of over 1.8 kV on 4 inch Si substrates and the suppression of current collapse," Power Semiconductor Devices and IC's, 2008. ISPSD '08. 20th International Symposium on , vol., no., pp.287,290, 18-22 May 2008

[35] Lidow, A., "GaN as a displacement technology for silicon in power management," Energy Conversion Congress and Exposition (ECCE), 2011 IEEE , vol., no., pp.1,6, 17-22 Sept. 2011

[36] Mishra, Umesh K.; Parikh, Primit; Yi-Feng Wu, "AlGaN/GaN HEMTs-an overview of device operation and applications," Proceedings of the IEEE , vol.90, no.6, pp.1022,1031, Jun 2002

[37] TPH2006 datasheet from Transphorm Inc., www.transphormusa.com/

[38] IPP60R160C6 datasheet from Infineon, www.infineon.com/

[39] Kakigano, H.; Miura, Y.; Ise, T., "Low-Voltage Bipolar-Type DC Microgrid for Super High Quality Distribution," Power Electronics, IEEE Transactions on , vol.25, no.12, pp.3066,3075, Dec. 2010

[40] Johnson, B.K.; Lasseter, R.H., "An industrial power distribution system featuring UPS properties," Power Electronics Specialists Conference, 1993. PESC '93 Record., 24th Annual IEEE , vol., no., pp.759,765, 20-24 Jun 1993

[41] Johnson, B.K.; Lasseter, R.H.; Alvarado, F.L.; Adapa, R., "Expandable multiterminal DC systems based on voltage droop," Power Delivery, IEEE Transactions on , vol.8, no.4, pp.1926,1932, Oct 1993

[42] Lasseter, R.H., "MicroGrids," Power Engineering Society Winter Meeting, 2002. IEEE , vol.1, no., pp.305,308 vol.1, 2002

[43] Ito, Youichi, Yang Zhongqing, and Hirofumi Akagi. "DC microgrid based distribution power generation system." Power Electronics and Motion Control Conference, 2004. IPEMC 2004. The 4th International. Vol. 3. IEEE, 2004.

[44] Schonberger, J.; Duke, R.; Round, S.D., "DC-Bus Signaling: A Distributed Control Strategy for a Hybrid Renewable Nanogrid," Industrial Electronics, IEEE Transactions on , vol.53, no.5, pp.1453,1460, Oct. 2006

[45] Chen, D.; Xu, L.; Yao, L., "DC Voltage Variation Based Autonomous Control of DC Microgrids," Power Delivery, IEEE Transactions on , vol.28, no.2, pp.637,648, April 2013

[46] Cvetkovic, I.; D. Dong; W. Zhang; L. Jiang; Boroyevich, D.; Lee, F.C.; Mattavelli, P., "A testbed for experimental validation of a low-voltage DC nanogrid for buildings," Power Electronics and Motion Control Conference (PEMC), 15th International , Sept. 2012

[47] VL45E Datasheet from http://www.saftbatteries.com/

[48] M. Brousselya, Ph. Biensanb, F. Bonhommeb, etc., “Main aging mechanisms in Li ion batteries”; Journal of Power Sources Volume 146, Issues 1-2, 26 August 2005, Pages 90-96;

[49] Soo S. Choi, Hong S. Lim, “Factors that affect cycle-life and possible degradation mechanisms of a Li-ion Cell Based on LiCoO2”, Journal of Power Source, Volume 111, Issue 1, 18 September 2002, Pages 130-136

[50] Min Chen; Rincon-Mora, G.A., "Accurate electrical battery model capable of predicting runtime and I-V performance," Energy Conversion, IEEE Transactions on , vol.21, no.2, pp.504,511, June 2006

[51] AD7280 Datasheet, www.analog.com

[52] BQ77PL900 Datasheet, www.ti.com

[53] William H. DeLuca, “System and Method for Charging electrochemical cells in series”; US4238721;

[54] Hopkins, Douglas C.; Mosling, C.R.; Hung, S.T., "Dynamic equalization during charging of serial energy storage elements," Industry Applications, IEEE Transactions on , vol.29, no.2, pp.363,368, Mar/Apr 1993

[55] Kutkut, N.H.; Divan, D.M., "Dynamic equalization techniques for series battery stacks," Telecommunications Energy Conference, 1996. INTELEC '96., 18th International , vol., no., pp.514,521, 6-10 Oct 1996

[56] Stuart, T.A.; Wei Zhu, "A targeted equalizer for lithium ion battery packs," Vehicle Power and Propulsion Conference, 2009. VPPC '09. IEEE , vol., no., pp.175,180, 7-10 Sept. 2009

[57] Moo, C.S.; Yao Ching Hsieh; Tsai, I.S., "Charge equalization for series-connected batteries," Aerospace and Electronic Systems, IEEE Transactions on , vol.39, no.2, pp.704,710, April 2003

[58] Moo, C.S.; Hsieh, Y.-C.; Tsai, I.S.; Cheng, J.C., "Dynamic charge equalisation for series-connected batteries," Electric Power Applications, IEE Proceedings - , vol.150, no.5, pp.501,505, 9 Sept. 2003

[59] Yin-Hai Zhang; Ji-Gang Li; Jun Lin; Jin-Fa Ge, "A Charging Equalization Circuit with Odd and Even Module for Li-ion Series-Connected Batteries," Artificial Intelligence and

Computational Intelligence, 2009. AICI '09. International Conference on , vol.1, no., pp.553,557, 7-8 Nov. 2009

[60] Cassani, P.A.; Williamson, S.S., "Design, Testing, and Validation of a Simplified Control Scheme for a Novel Plug-In Hybrid Electric Vehicle Battery Cell Equalizer," Industrial Electronics, IEEE Transactions on , vol.57, no.12, pp.3956,3962, Dec. 2010

[61] Sang-Hyun Park; Tae-Sung Kim; Jin-Sik Park; Gun-Woo Moon; Myung-Joong Yoon, "A new battery equalizer based on buck-boost topology," Power Electronics, 2007. ICPE '07. 7th Internatonal Conference on , vol., no., pp.962,965, 22-26 Oct. 2007

[62] Ziling Nie; Mi, C., "Fast battery equalization with isolated bidirectional DC-DC converter for PHEV applications," Vehicle Power and Propulsion Conference, 2009. VPPC '09. IEEE , vol., no., pp.78,81, 7-10 Sept. 2009

[63] Kutkut, N.H., "A modular nondissipative current diverter for EV battery charge equalization," Applied Power Electronics Conference and Exposition, 1998. APEC '98. Conference Proceedings 1998., Thirteenth Annual , vol.2, no., pp.686,690 vol.2, 15-19 Feb 1998

[64] Lee, Yuang-Shung; Ming-Wang Cheng, "Intelligent control battery equalization for series connected lithium-ion battery strings," Industrial Electronics, IEEE Transactions on , vol.52, no.5, pp.1297,1307, Oct. 2005

[65] Lee, Yuang-Shung; Guo-Tian Cheng, "Quasi-Resonant Zero-Current-Switching Bidirectional Converter for Battery Equalization Applications," Power Electronics, IEEE Transactions on , vol.21, no.5, pp.1213,1224, Sept. 2006

[66] Kimball, J.W.; Kuhn, B.T.; Krein, P.T., "Increased Performance of Battery Packs by Active Equalization," Vehicle Power and Propulsion Conference, 2007. VPPC 2007. IEEE , vol., no., pp.323,327, 9-12 Sept. 2007

[67] Baughman, A.C.; Ferdowsi, M., "Double-Tiered Switched-Capacitor Battery Charge Equalization Technique," Industrial Electronics, IEEE Transactions on , vol.55, no.6, pp.2277,2285, June 2008

[68] Sano, K.; Fujita, H., "Voltage-Balancing Circuit Based on a Resonant Switched-Capacitor Converter for Multilevel Inverters," Industry Applications, IEEE Transactions on , vol.44, no.6, pp.1768,1776, Nov.-dec. 2008

[69] Yu Du; Mengqi Wang; Meitl, R.T.; Lukic, S.; Huang, A.Q., "High-frequency high-efficiency DC-DC converter for distributed energy storage modularization," IECON 2010 - 36th Annual Conference on IEEE Industrial Electronics Society , vol., no., pp.1832,1837, 7-10 Nov. 2010

[70] Hong-sun Park; Chol-Ho Kim; Ki-Bum Park; Gun-Woo Moon; Joong-Hui Lee, "Design of a Charge Equalizer Based on Battery Modularization," Vehicular Technology, IEEE Transactions on , vol.58, no.7, pp.3216,3223, Sept. 2009

[71] Datasheet BQ77PL157A4225, BQ76PL536, BQ29440, Texas Instruments

[72] http://liionbms.com/php/index.php

[73] V.H. Johnson, NREL, Temperature-Dependent Battery Models for High-Power Lithium-Ion Batteries, 2000;

[74] Wei Zhang, Fred. C. Lee, "Active cell equalizer techniques classifications for lithium-ion batteries", April.5th , PMC quarterly review, 2011, Blacksburg, VA;

[75] 2011 Nissan Leaf – VIN 0356, Advanced Vehicle Testing, Vehicle Technologies Program, Energy Efficiency & Renewable Energy, U.S. Department of Energy.

[76] http://insideevs.com/dissecting-leaf-battery-wvideo/

[77] 2013 Chevrolet Volt – VIN 3929, Advanced Vehicle Testing, Vehicle Technologies Program, Energy Efficiency & Renewable Energy, U.S. Department of Energy.

[78] http://leandesign.com/chevy-volt-tear-down-videos/

[79] http://www.eaton.com/Electrical/USA/ProductsandServices/ElectricalDistribution/ElectricVehicleChargingSolutions/index.htm;

[80] http://www.abb.com/product/seitp332/a0b7275bea656b16c1257903004 abf65.aspx

[81] Aggeler, D.; Canales, F.; Zelaya-De La Parra, H.; Coccia, A.; Butcher, N.; Apeldoorn, O.; "Ultra-fast DC-charge infrastructures for EV-mobility and future smart grids"; Innovative Smart Grid Technologies Conference Europe (ISGT Europe), 2010 IEEE PES, Page(s):1-8

[82] D. Dong, D. Boroyevich, W. Ruxi, and I. Cvetkovic, "A two-stage high power density single-phase ac-dc bi-directional PWM con-verter for renewable energy systems," in Energy Conversion Con-gress and Exposition (ECCE), 2010 IEEE, 2010, pp. 3862-3869.

[83] D. Dong, Z. Xuning, L. Fang, D. Boroyevich, and P. Mattavelli, "Common-mode EMI noise reduction for grid-interface converter in low-voltage DC distribution system," in

Applied Power Elec-tronics Conference and Exposition (APEC), 2012 Twenty-Seventh Annual IEEE, 2012, pp. 451-457.

[84] D. Dong, L. Fang, Z. Wei, D. Boroyevich, P. Mattavelli, I. Cvetkovic, J. Li, and K. Pengju, "Passive filter topology study of single-phase ac-dc converters for DC nanogrid applications," in Applied Power Electronics Conference and Exposition (APEC), 2011 Twenty-Sixth Annual IEEE, 2011, pp. 287-294.

[85] Li Jiang; Wei Zhang; Dong Dong; Cvetkovic, I.; Lee, F.C.; Mattavelli, P.; Boroyevich, D.; Pengju Kong, "R-based MPPT method for smart converter PV system," Applied Power Electronics Conference and Exposition (APEC), 2012 Twenty-Seventh Annual IEEE , vol., no., pp.2072,2079, 5-9 Feb. 2012

[86] Feng Wang; Pengju Kong; Lee, F.C.; Fang Zhuo, "Analysis and optimization of module integrated MPPT converter based residential PV system," Power Electronics and Applications (EPE), 2013 15th European Conference on , vol., no., pp.1,7, 2-6 Sept. 2013

[87] Zongsheng Cao, "Multi-Phase Smart Converter for PV System", Thesis, Virginia Tech, 2014

[88] Li Jiang; Wei Zhang; Dong Dong; Cvetkovic, I.; Lee, F.C.; Mattavelli, P.; Boroyevich, D.; Pengju Kong, "R-based MPPT method for smart converter PV system," Applied Power Electronics Conference and Exposition (APEC), 2012 Twenty-Seventh Annual IEEE , vol., no., pp.2072,2079, 5-9 Feb. 2012

[89] www.pge.com

[90] www.nrel.gov